

**RADIO FREQUENCY ANTENNA DESIGNS AND METHODOLOGIES
FOR HUMAN BRAIN COMPUTER INTERFACE
AND ULTRAHIGH FIELD MAGNETIC RESONANCE IMAGING**

by

Yujuan Zhao

B.Eng., Hefei University of Technology, 2006

M.S., Shanghai Jiao Tong University, 2009

Submitted to the Graduate Faculty of
Swanson School of Engineering in partial fulfillment
of the requirements for the degree of
Doctor of Philosophy

University of Pittsburgh

2015

UNIVERSITY OF PITTSBURGH
SWANSON SCHOOL OF ENGINEERING

This dissertation was presented

by

Yujuan Zhao

It was defended on

February 10, 2015

and approved by

George D. Stetten, M.D., Ph.D., Professor, Department of Bioengineering

Howard J. Aizenstein, M.D., Ph.D., Associate Professor, Psychiatry

Zhi-Hong Mao, Ph. D. Associate Professor, Departments of Electrical and Computer
Engineering

Dissertation Director: Tamer S. Ibrahim, Ph.D., Associate Professor, Department of
Bioengineering and Radiology

Copyright © by Yajuan Zhao

2015

**RADIO FREQUENCY ANTENNA DESIGNS AND METHODOLOGIES
FOR HUMAN BRAIN COMPUTER INTERFACE
AND ULTRAHIGH FIELD MAGNETIC RESONANCE IMAGING**

Yujuan Zhao, Ph.D.

University of Pittsburgh, 2015

Brain Computer Interface (BCI) and Magnetic Resonance Imaging (MRI) are two powerful medical diagnostic techniques used for human brain studies. However, wired power connection is a huge impediment for the clinical application of BCI, and most current BCIs have only been designed for immobile users in a carefully controlled environment. For the ultrahigh field ($\geq 7T$) MRI, limitations such as inhomogeneous distribution of the transmit field (B_1^+) and potential high power deposition inside the human tissues have not yet been fully combated by existing methods and are central in making ultrahigh field MRI practical for clinical use. In this dissertation, radio frequency (RF) methods are applied and RF antennas/coils are designed and optimized in order to overcome these barriers. These methods include: 1) designing implanted miniature antennas to transmit power wirelessly for implanted BCIs; 2) optimizing a new 20-channel transmit array design for 7 Tesla MRI neuroimaging applications; and 3) developing and implementing a dual-optimization method to design the RF shielding for fast MRI imaging methods.

First, three miniaturized implanted antennas are designed and results obtained using finite difference time domain (FDTD) simulations demonstrate that a maximum RF power of up to 1.8 milliwatts can be received at 2 GHz when the antennas are implanted at the dura, without violating the government safety regulations. Second, Eigenmode arrangement of the 20-channel transmit coil allows control of RF excitation not only at the XY plane but also along the Z

direction. The presented results show the optimized eigenmode could generate 3D uniform transmit B_1^+ excitations. The optimization results have been verified by *in-vivo* experiments, and they are applied with different protocol sequences on a Siemens 7 Tesla MRI human whole body scanner equipped with 8 parallel transmit channels. Third, echo planar imaging (EPI), B_1^+ maps and S matrix measurements are used to verify that the proposed RF shielding can suppress the eddy currents while maintaining the RF characteristics of the transmit coil.

The contributions presented here will provide a long-term and safer power transmission path compared to the wire-connected implanted BCIs and will bring ultrahigh field MRI technology closer to clinical applications.

TABLE OF CONTENTS

PREFACE.....	XVI
1.0 INTRODUCTION.....	1
1.1 MOTIVATION	2
1.1.1 Challenges of Brain Computer interfaces: direct wire connections	2
1.1.2 Challenges of Ultrahigh-Field MRI: Transmit Fields Inhomogeneity and Specific Absorption Rate.....	3
1.1.3 Challenges of Ultrahigh Field MRI: Eddy Currents.....	3
1.2 OBJECTIVES OF THIS DISSERTATION.....	4
1.3 THE STRUCTURE OF THIS DISSERTATION	6
2.0 BACKGROUND.....	11
2.1 BRAIN COMPUTER INTERFACE.....	11
2.1.1 Brain Computer Interfaces Review	11
2.1.2 Brain Computer Interface Architecture.....	12
2.2 IMPLANTED ANTENNA WITHIN THE HUMAN ENVIRONMENT.....	13
2.2.1 Antenna Geometry and Miniaturization Techniques	13
2.2.2 Wireless Data Transmission and Power Transmission.....	14
2.2.3 RF Safety	15
2.3 MAGNETIC RESONANCE IMAGING	15
2.3.1 Static Magnetic Field.....	16

2.3.2	RF Excitation	17
2.3.3	RF Coils	18
2.3.4	Spatial Encoding.....	19
2.3.5	Pulse and Sequence Design	20
2.4	FINITE DIFFERENCE TIME DOMAIN METHOD.....	21
2.4.1	The Finite-Difference Time-Domain formulation	21
2.4.2	One Dimensional Transmission Line Excitation	26
2.5	FINITE ELEMENT METHOD.....	28
2.5.1	Finite Elements in Electromagnetics.....	29
3.0	IMPLANTED MINIATURIZED ANTENNA FOR BRAIN COMPUTER INTERFACE APPLICATIONS	31
3.1	INTRODUCTION.....	31
3.2	MATERIALS AND METHODS	33
3.2.1	FDTD Simulation and the Transmission Line Feed Model.....	33
3.2.2	Antenna Geometry and Antenna Performance Parameters	35
3.2.3	Human Head Model	36
3.2.4	Antenna Measurement Set-up.....	37
3.3	RESULTS	38
3.3.1	Measurement Validation of the FDTD Simulations.....	38
3.3.2	Effects of Ultra-thin Insulating Layers.....	39
3.3.3	Effects of the Insulating Layer Dielectric Properties	42
3.3.4	Effects of the Head Tissues Properties	43
3.3.5	Effects of the Human Head Phantom Shape and Dielectric Properties ...	46
3.3.6	Designs of the Implanted Antennas	48

3.3.7	Maximum Power Reception without SAR Violations	51
3.4	CONCLUSION	53
4.0	IN-DEPTH ANALYSIS OF THE ELECTROMAGNETIC PSEUDO MODES PREDEDUCED BY A 20 CHANNEL TIC-TAC-TOE TRANSMIT ARRAY.....	55
4.1	INTRODUCTION.....	55
4.2	MATERIAL AND METHODS	57
4.2.1	The RF Coil	57
4.2.2	Determination of Eigenmodes	59
4.2.3	Helmholtz Equation and Current Requirements	60
4.2.4	Simulations and Experiments.....	62
4.3	RESULTS	63
4.3.1	Eigenmodes inside the Phantom and the Head Model.....	63
4.3.1.1	B_1^+ Field and SAR Comparison for Mode 1 at Different Levels	63
4.3.1.2	B_1^+ Field and SAR Comparison for Other Modes at Different Levels.....	66
4.3.1.3	Peak Local SAR.....	69
4.3.2	Experimental Demonstration	70
4.4	DISCUSSION AND CONCLUSION	72
5.0	TRANSMIT ARRAY EIGENMODES OPTIMIZATION.....	75
5.1	INTRODUCTION.....	75
5.2	MATERIALS AND METHODS	77
5.2.1	RF Coil and Eigenmodes.....	77
5.2.2	FDTD Simulations and Field Optimization	78
5.2.3	Experiments	80
5.3	RESULTS	81

5.3.1	Slice Excitation Verification and Limits of Homogenous Slice via RF Shimming.....	81
5.3.2	3D Field Simulation Verification.....	84
5.3.3	Transmit Field and Absorbed Power Efficiency	85
5.3.4	Optimization Criteria Comparison.....	87
5.3.5	Comparison between Different Coils and Applications.....	89
5.3.6	Experimental Verifications.....	91
5.3.7	20 Modes and B_1^+ shimming Optimizations Comparison.....	92
5.3.8	Virtual Observation Points Applications and Verification.....	93
5.4	DISCUSSION AND CONCLUSION	96
6.0	DUAL OPTIMIZATION METHOD OF RF AND QUASI-STATIC FIELD SIMULATIONS FOR REDUCTION OF EDDY CURRENTS GENERATED ON 7T RF COIL SHIELDING.....	98
6.1	INTRODUCTION.....	98
6.2	METHODS	100
6.2.1	The RF Coil	100
6.2.2	Gradient Field Induced Eddy Current Simulations (FEM)	102
6.2.3	Full Wave RF Field Simulations (FDTD).....	105
6.2.4	RF Testing and 7T Experiments	106
6.3	RESULTS	107
6.3.1	Eddy Current Simulation Verification and Z Gradient Field Behavior along the Magnet Axis	107
6.3.2	Comparison of Rectangular and Circular Shielding.....	109
6.3.3	Effects of Thickness of Copper Layers and the Top Panel.....	111
6.3.4	Effects of Simple-Structured Slots	114

6.3.5	Dual Optimization Approach	115
6.3.6	<i>In-Vivo</i> Demonstration	117
6.4	DISCUSSION	118
7.0	CONCLUSIONS AND FUTURE WORK	123
7.1	SUMMARY AND FINDINGS	123
7.2	CONTRIBUTION OF THIS DISSERTATION	124
7.2.1	Non 50 Ohm Antenna and SAR Regulation Considerations	124
7.2.2	A New RF coil Mode Excitation Paradigm	126
7.2.3	New Eddy Currents Calculation and Shielding Slot Methods	127
7.3	FUTURE WORKS	128
7.3.1	Implanted Antenna Designed for Wireless Power Transmission	128
7.3.2	RF Coil Designed for 7 Tesla MRI	129
APPENDIX A	130
APPENDIX B	135
BIBLIOGRAPHY	157

LIST OF TABLES

Table 3.1. Dielectric property of three adjacent major tissues at three different locations inside the human head (Figure 3.8) at 2.4GHz.....	44
Table 3.2. Maximum power reception under IEEE and ICNIRP SAR limit (2 Watts perKg per 10gm) at 2 GHz when the implanted antenna is placed right under the dura.....	53
Table 4.1: Relative Phases of the 5 Levels of the Coil for the Phantom	63
Table 6.1: Z-gradient coil arrangement	103

LIST OF FIGURES

Figure 2.1: Electric and magnetic field vector components with a Yee cell at (i,j,k) position.....	26
Figure 2.2: The 1D transmission line model to the 3D grid	28
Figure 3.1: Three different human model phantoms used for antenna performance analysis. a) Sagittal cross sections of the multi-tissue head model at the middle slice; b) Sagittal cross section of the homogenous head-shaped phantom model at the middle slice; c) Homogeneous rectangular shape phantom model.....	36
Figure 3.2: Monopole antenna measurement set up	37
Figure 3.3: A comparison of the FDTD simulation results with the measurements for the input impedance of the monopole antenna	38
Figure 3.4: Geometry of the antenna and head model a) Implanted rectangular antenna; b) Antenna position inside the head model (sagittal view of the head model is shown), the color bar scale represents the relative permittivity values.....	40
Figure 3.5: Effects of thin insulating layers on the input impedance of the implanted antenna inside the head model	41
Figure 3.6: Simulation results of antennas surrounded with insulating layers with the same thickness but the different dielectric properties	42
Figure 3.7: Implanted antenna at three different locations inside the human head model	44
Figure 3.8: Input Impedance of the implanted rectangular antenna at three different locations inside the human head (Figure 3.7).....	45
Figure 3.9: Input Impedance of the antenna when implanted 19 mm inside the multi-tissue head model, the head shaped homogenous phantom model and the rectangular homogenous phantom model.....	47
Figure 3.10: Geometry (a) and input impedance of the implanted rectangular antenna (b).....	49
Figure 3.11: Geometry (a) and input impedance of the implanted serpentine antenna (b)	50

Figure 3.12: Geometry of a dipole antenna	51
Figure 4.1: Coil schematic diagrams and load positons.	58
Figure 4.2: Central sagittal, and 3 axial slices of 1) B1+ field distributions (phase and intensity maps) per average SAR over the entire 3D volume that is equal to 3.2 W/kg/10g and 2) SAR distributions per average B1+ field intensity inside the ROIs (B1+ field intensity is normalized to 1.97uT).....	65
Figure 4.3: B1+ distributions for different modes. Center sagittal slices of B1+ field distributions per average SAR over the entire 3D volume (normalized to 3.2 W/kg/10g) are presented. Field patterns inside the phantom and human head model are comparable.	68
Figure 4.4: Average B1+ intensities calculated inside 8 different ROIs (shown in Figure 4.1.) The values of the average B1+ intensities are normalized to an average SAR over the entire 3D head volume. The unit is Tesla per 3.2 W/kg/10g.....	69
Figure 4.5: The ratio between the local peak SAR and average SAR over the entire 3D head volume for different levels and modes.	70
Figure 4.6: Experimental and simulated B1+ field distributions for the phantom and the human head. The two central axial slices of Mode1 are compared for the phantom and three central sagittal slices are compared for the human head	71
Figure 4.7: 3D in-vivo B1+ map of one optimized preliminary case. The map was normalized to maximum 90° flip angle to show the uniformity.	72
Figure 5.1: Coil arrangements. (a) Parallel transmit system connected to the coil by using N-way power splitters, phase cables are needed for specific applications. (b) TTT coil (without RF shielding) and the relative human head position. (c) TEM coil (without RF shielding) and the relative human head position.	78
Figure 5.2: Experimental and simulated B1+ magnitude and phase maps	83
Figure 5.3: Experimental and simulated B1+ magnitude maps of axial and sagittal slices targeted for homogeneous excitation.	83
Figure 5.4: Phantom localization	83
Figure 5.5: The 20 ch pseudo quadrature mode (not optimized for homogeneity nor SAR.) Simulated magnetic fields compared with measured magnetic field distribution (sagittal and axial slice). In-vivo B1+ maps were measured using Saturated Turbo Flash method (1ms square pulse); cable loss was taken into consideration for the intensity calculation.....	85

Figure 5.6: TTT 20-ch pseudo quadrature excitation and quadrature excitation generated by the top 4-ch quadrature excitation compared with TEM quadrature excitation.....	86
Figure 5.7: Field uniformity (COV, max/min), efficiency, SAR distribution for all of the optimization results.	88
Figure 5.8: B1+distribution from two different optimizations. B1+ efficiency is 52% and 61% for Optimization 1 and Optimization 2 respectively; absorbed efficiency is 20% and 19% respectively.	90
Figure 5.9: In-vivo 3D MPRAGE images (0.9 x 0.9 x1.0 mm ³ , TR/TE/TI = 3000/2.32/1200 ms, ~10 minutes). The images are obtained by Dr. Ibrahim’s Lab.....	91
Figure 5.10: In-vivo Turbo Spin Echo with GRAPPA 2 (0.4x0.4x2 mm ³ , TR/TE=14000/54ms). The images are obtained by Dr. Ibrahim’s Lab.	91
Figure 5.11: MPRAGE and SWI images to show the excitation coverage. The images are obtained by Dr. Ibrahim’s Lab.....	92
Figure 5.12: 20 modes optimization inside the head and brain	93
Figure 5.13: Global and local SAR monitoring pathway	94
Figure 5.14: Global power and local SAR verifications with VOP supervision	95
Figure 6.1: Schematics of the coil, RF shielding and gradient coils.....	101
Figure 6.2: CAD models of circular and rectangular shielding	104
Figure 6.3 Built TEM coil and TTT coil.....	105
Figure 6.4: Time domain and frequency domain eddy current results.	108
Figure 6.5: Gradient field distribution (simulations)	109
Figure 6.6: 7T Tx-SENSE excitation pattern for circular & rectangular coil shielding.	110
Figure 6.7 : Measurements of gradient field intensities at 7T.	110
Figure 6.8: 7T In-vivo BOLD images.....	111
Figure 6.9: Four different copper shielding comparisons.....	113
Figure 6.10: In-vivo EPI images (22 slices to cover the whole brain) with (a) the proposed slots in double 4 μ m (2x4 μ m) copper shielding and with (b) 18 μ m intact/no-slots copper shielding.....	117

Figure 6.11: Ghosting ratio comparisons (measured with EPI scans) between 5 tested/discussed copper shielding methods. 119

Figure 6.12: In-vivo EPI images with the modified slots in the double 4 μ m (2x4 μ m) copper shielding using the 20-ch Tx coil with 32-ch Rx insert. 121

PREFACE

I would first like to thank my advisor, Dr. Tamer S. Ibrahim, for providing support and advice throughout my PhD study, both in academics and career planning. I always enjoy our discussions and learn new ways of thinking from him. My PhD study wouldn't be possible without his guidance, his encouragement and his care. I would also like to thank all my committee members, Dr. Zhi-Hong Mao, Dr. Howard J. Aizenstein and Dr. George D. Stetten. Dr. Zhi-Hong Mao trusted my work and encouraged me during my dissertation research. He has taught me the most fundamental part of positive psychology through discussions that motivated me to do better. Dr. Howard J. Aizenstein has always been very supportive in our collaborations. I'd like to thank him for all the wonderful discussions around the late life diseases, especially Alzheimer's disease. I hope I can continue to study brain functions in my future career. I'd like to thank Dr. George Stetten for his advice on my dissertation. He has inspired me to want to design a medical device that is "going to be like cell phones, every doctor and nurse want to use carry one around," as he said in one of his media interviews

I would also like to thank all the team members from Dr. Ibrahim's lab and the UPMC MR Research Center. I could not get a lot of the results in this dissertation without their hard work. In particular, I would like to thank Dr. Tiejun Zhao, Anthony Defranco, Dr. Hoby Hetherington, Dr. Jullie Pan, Dr. Hai Zheng, Dr. Tae Kim, Dr. Ty Bae, Dr. Zhen Yao, Dr. Chuan Lu, Dr. Eric Lin, Dr. Yongxian Qian, Narayan Krishnamurthy, Daniel Stough, Sossena Wood,

Jung-Hwan Kim, Shailesh Raval and Tales Santini for their support both professionally and personally.

Last but not least, I would like to dedicate my dissertation to my parents, my sister and my dear friends, for their continual support and love. I thank you for always being with me and sharing this wonderful journey.

1.0 INTRODUCTION

Electromagnetic waves travel at the speed of light, and they transfer energy and information through empty space and media. Within the electromagnetic spectrum, radio frequency is normally defined from 3 kHz to 300 GHz. Radio frequency (RF) wave propagation is non-ionizing radiation. Therefore, it has been preferred for body-centric wireless communication and non-invasive human imaging methods. In this dissertation, RF methodologies are used to facilitate human brain studies.

The human brain is the center of the nervous system. It controls movement, autonomic function (e.g. heartbeat and respiration), sensation, learning, memory, emotion and thought. Up to now, the human brain has been seen as one of the most phenomenal yet complex and little-understood structures; it is susceptible to many types of irreparable damage and incurable (as of to date) diseases, such as Alzheimer's disease, Parkinson's disease, etc. Consequently, advanced technologies are needed to 1) understand normal brain physiology, 2) predict, detect, and monitor the changes within the brain in the presence of neurological diseases, and 3) facilitate the treatment of brain damage or directly treat the diseases. Brain Computer Interface (BCI) and Magnetic Resonance Imaging (MRI) are two powerful medical diagnostic techniques used for human brain studies. However, they both face significant challenges (detailed in the following sections). In this dissertation, RF methods are applied, and RF antennas/coils are designed and optimized in order to overcome such challenges.

1.1 MOTIVATION

1.1.1 Challenges of Brain Computer interfaces: direct wire connections

Brain Computer Interfaces (BCIs) are devices designed to establish a communication link between the human brain and neuro-prosthetic devices in order to study brain function and/or restore sensory information lost as a result of injury or disease (1). The invasive BCIs are implanted either on the surface of the brain or inserted into the cerebral cortex to capture local field/action potentials (2-4). They provide the high spatial/temporal signal precision required for implementing real-time control of a robotic arm (5) and a prosthetic limb (6) to restore independence for people with paralysis (7).

However, nearly all implanted BCIs require a direct power connection with external prosthetics devices. These implanted BCIs can only be used in a research environment for a very short time due to the increase of device failure and clinical risks (8). This in turn limits functionality of BCI in application and clinical practice. Researchers have tried various wireless power supply methods such as micro batteries and inductive coupling coils, but none of these power modules can be implanted in human brains safely and are able to provide stable power chronically. RF power transmission is a promising approach to solve the safety problem and to realize long-term implantation of BCIs in users. The RF power transmission could provide more robust and long-term communication compared with wire-connected BCIs since it will reduce the tissue damage caused by the wire connections and the stress caused by plugging and unplugging the recording system.

1.1.2 Challenges of Ultrahigh-Field MRI: Transmit Fields Inhomogeneity and Specific Absorption Rate

MRI is based on the nuclear magnetic resonance (NMR) phenomenon. The extraordinary soft tissue contrast of MRI makes it the preferred imaging modality for diagnosing many soft tissue disorders especially in the brain, spinal cord, and knees. Ultrahigh-field (≥ 7 Tesla) MRI is of high interest since it can generate higher resolution anatomical imaging, better localization imaging and improved spectroscopic imaging. However, there are technical and physical limitations associated with ultrahigh-field imaging that have not yet been fully combated: (a) the inhomogeneous distribution of the transmit fields B_1^+ (9-12), arising from the short wavelength interference effects and the large wave amplitude attenuation by high tissue conductivity and (b) the potential high-power deposition inside the human tissues (13,14) and the difficulty in supervising the local specific absorption rate (SAR) (15). Successful ultrahigh-field human MRI with safe and homogeneous B_1^+ field distribution will provide more accurate locations of brain diseases than other MRI imaging methods. This new technology will provide neuroimaging researchers the opportunity to observe disease-related structural changes in detail, which until now could only be observed with postmortem tissue analysis (16).

1.1.3 Challenges of Ultrahigh Field MRI: Eddy Currents

For ultrahigh-field MRI, RF shielding is oftentimes an essential component of the transmit coils (17-21). Many of the parallel transmit (PTX) trajectories use either spiral or EPI type gradient waveforms. These gradient waveforms can change rapidly (22,23). The fast-changing gradient waveforms induce intensive eddy currents that considerably distort the image quality.

Furthermore, for each transmit RF coil (i.e. head/knee/breast) used at the 7 Tesla MRI system, the RF coil shielding design varies, rendering the system eddy current correction potentially insufficient. In addition, this spatially non-linear eddy current behavior in regions close to the RF coil shielding may also render post-processing methods less reliable. As a result, eddy currents induced on RF coil shielding could be very problematic, so a systematic method to study and reduce eddy currents is necessary.

1.2 OBJECTIVES OF THIS DISSERTATION

The main goal of this dissertation is to provide solutions (based on physics and engineering concepts and using RF methods) to the challenges identified in section 1.1 in order to realize the clinical practice of wireless implanted BCIs and 7 Tesla MRI. Specifically, this work will design a compact, safe and feasible wireless communicating method for BCIs; optimize B_1^+ field distributions to generate a more uniform magnetic field for 7 Tesla MRI; minimize eddy currents generated in the RF shielding, and maintain RF performance at the same time.

Objective 1: Design and analyze miniaturized implantable antennas for BCI applications. The implantable miniaturized antennas operating at radio frequency is a promising approach in realizing long-term wireless data/power transmission and safe implantation of BCIs in patients. However, due to the limited antenna size and the electromagnetic loss from brain tissues, implantable miniaturized antennas suffer low radiation efficiency. The electromagnetic computational method Finite-Difference Time-Domain (FDTD) method and miniaturization techniques are applied in this work. The accuracy and stability of the implantable antenna FDTD simulation are verified. The effects of the biocompatible insulating layers and implantation

environment within the human brain on the implantable antenna's input impedance, frequency bandwidth and power transmission/absorption by tissues (i.e. specific absorption rate) are investigated.

Objective 2: Optimize B_1^+ field to mitigate the transmit field inhomogeneity. A new 20-channel Tic-Tac-Toe (TTT) RF coil is discussed. 3D eigenmode excitation paradigms are studied. Eigenmode arrangement of the 20-ch coil allows controlling RF excitation not only at XY plane but also along Z direction. Based on FDTD simulation results of the head model and water phantom, exhaustive optimizations are used to manipulate the coil's modes combinations (changing amplitudes of the excitations and phases in between) in order to generate a more uniform MR image where SAR regulations are considered. A 7T MRI scanner is used to image the phantoms and *in-vivo* human subjects. Since the load sensitivity of the TTT RF coil is robust, the optimization results could be extended for all patient scans without patient-specific simulations.

Objective 3: Minimize the gradient fields generated eddy currents in the RF coil shielding. The RF coil shielding is designed to suppress gradient field induced eddy currents without sacrificing the RF signal. A new and elaborate dual-optimization method is performed to design the RF shielding of the TTT coil. The designed RF shielding can reduce low frequency magnetic field distortions due to eddy currents and simultaneously maintain the RF characteristics of the RF-coil. The designs are tested on a 7T human scanner using phantoms and *in-vivo* subjects.

1.3 THE STRUCTURE OF THIS DISSERTATION

The chapter-by-chapter structure of the dissertation is given below. Publications from the work of each chapter are also listed.

Chapter 1 presents the specific objectives of this dissertation along with the current difficulties for Brain Computer Interfaces and ultrahigh field MRI.

Chapter 2 contains a review of Brain Computer Interfaces and describes the basic MR physics such as the generation and reception of MR signal. Implanted antennas inside the human environment are described. In addition, a brief mathematical description of two major numerical simulation methods used in this dissertation, the finite-difference time-domain (FDTD) method and finite element method (FEM), are presented.

Chapter 3 presents simulations, analyses and designs of implanted antennas for a wireless implantable RF-powered BCI application. Due to their limited size and the electromagnetic loss from human brain tissues, implanted miniaturized antennas suffer low radiation efficiency. The impact of thin (on the order of 100 micrometers thickness) biocompatible insulating layers, dielectric properties of the biocompatible insulating layers, and the implantation position inside human brain tissues on the implanted antenna performance have been investigated. This work resulted in two journal articles and one conference paper:

- Yujuan Zhao, Robert L. Rennaker, Chris Hutchens, and Tamer S. Ibrahim, “Implanted Miniaturized Antenna for Brain Computer Interface Applications: Analysis and Design”, PloS one 2014; 9(7): e103945.
- Yujuan Zhao, Lin Tang , Robert Rennaker, Chris Hutchens and Tamer S. Ibrahim, “Studies in RF Power Communication, SAR, and Temperature Elevation in Wireless Implantable Neural Interfaces”, PloS one 2013;8(11):e77759.

- Yujuan Zhao, Robert Rennaker, Chris Hutchens and Tamer S. Ibrahim, “Simulation of Implantable Miniaturized Antennas for Brain Machine Interface Applications”, the 28th Applied Computational Electromagnetics Society Annual Meeting, Columbus, OH, April 2012.

Chapter 4 studies the 3D eigenmode excitation paradigms of a 20-channel TTT based RF transmit array design. The freedom to manipulate current distribution in the X, Y, and Z directions contributes to the generation of targeted field distributions at 7 Tesla MRI. The transmit fields are calculated using the FDTD method. The eigenmodes of the transmit coil are determined using the magnetic field matrix. The 20-ch TTT transmit array can be viewed as a coil composed of 5 4-channel transmit arrays. Each transmit array is composed of 4 elements mounted at shifted locations in the XY plane and at different levels along the static magnet field (Z) direction. For each Z level of the coil elements, 4 distinctive eigenmodes can be generated; the eigenmodes can excite different regions along the Z direction. Coil eigenmodes are tested on a 7T MRI scanner with phantoms and *in-vivo* human subjects. An optimized case is also presented to show the eigenmode could be optimized and can generate 3D uniform B_1^+ excitations. This work resulted in one journal article, and two ISMRM conference abstracts:

- Yujuan Zhao, Tiejun Zhao, Tamer S. Ibrahim, “In-depth Analysis of the Electromagnetic Pseudo Modes Produced by a 20 channel Tic-Tac-Toe Transmit Array”, under review.
- Yujuan Zhao, Sossena Wood, Tiejun Zhao, Narayanan Krishnamurthy, Tamer S Ibrahim, “Simultaneous Excitation of Distinct Electromagnetic Modes Using a Tx Array”, ISMRM Annual Meeting, April 2013, p4399.

- Yujuan Zhao, Tiejun Zhao, Narayanan Krishnamurthy, and Tamer Ibrahim, “In-depth Analysis of the Electromagnetic Modes Produced by a 20 channel Transmit Array”, under review the 23th ISMRM Annual Meeting, May 2015

Chapter 5 studies the 3D transmit eigenmode optimizations. An exhaustive search is used to go through all possible eigenmode combinations. While there could be many different optimization solutions for the RF excitation that achieve a very similar fidelity to the targeted excitation pattern (homogenous B_1^+ field), minimizing the specific absorption rate (SAR) and maximizing the B_1^+ efficiency are two of the most important constraints of the optimization procedure. The optimized fields are also compared with an 8-ch TEM coil. This work resulted in one journal article, and three ISMRM conference abstracts:

- Yujuan Zhao, Tiejun Zhao, Narayanan Krishnamurthy, and Tamer S. Ibrahim, “20-Ch Transmit Array Modes Optimization”, under review
- Yujuan Zhao, Tiejun Zhao, Narayanan Krishnamurthy, and Tamer S. Ibrahim, “On the E-field construction/deconstruction and B_1^+ Efficiency/Homogeneity with Transmit Array Eigen Modes”, the 22th ISMRM Annual Meeting, May 2014, p4931
- Yujuan Zhao, Tiejun Zhao, and Tamer Ibrahim, “Experiments and Analysis of Virtual Observation Points at 7T”, under review the 23th ISMRM Annual Meeting, May 2015
- Yujuan Zhao, Narayanan Krishnamurthy, Sossena Wood, Tiejun Zhao, Shailesh B. Raval, and Tamer S. Ibrahim, “3D Eigenmodes Optimizations for 3D Imaging at 7T”, under review the 23th ISMRM Annual Meeting, May 2015

Chapter 6 optimizes the design of RF shielding of transmit coils at 7T and reduces eddy currents generated on the RF shielding when imaging with rapid gradient waveforms. One set of a four-element, 2x2 Tic-Tac-Toe (TTT) head coil structure is selected and constructed to study

eddy currents on the RF coil shielding. The generated eddy currents are quantitatively studied in the time and frequency domains. The RF characteristics are studied using the FDTD method. Five different kinds of RF shielding are tested on a 7T MRI scanner with phantoms and *in-vivo* human subjects. The eddy current simulation method is verified by the measurement results. Eddy currents induced by solid/intact and simple-structured slotted RF shielding can significantly distort the gradient fields. Echo Planar Imaging (EPI) images, B_1^+ maps and S matrix measurements verify that the proposed slot pattern can suppress the eddy currents while maintaining the RF characteristics of the transmit coil. The presented dual-optimization method can be used to design the RF shielding and reduce the gradient field-induced eddy currents while maintaining the RF characteristics of the transmit coil. This work resulted in one journal article, and two ISMRM conference abstracts:

- Yujuan Zhao , Tiejun Zhao , Shailesh B. Raval , Narayanan Krishnamurthy, Hai Zheng , Chad T. Harris , William B. Handler , Blaine A. Chronik , and Tamer S. Ibrahim, “Dual Optimization Method of RF and Quasi-Static Field Simulations for Reduction of Eddy Currents Generated on 7T RF Coil Shielding”, *Magnetic Resonance in Medicine*, DOI 10.1002/mrm.25424.
- Yujuan Zhao, Daniel K. Stough, Hai Zheng, Tiejun Zhao, Chad T. Harris, William Handler, Blaine A. Chronik, Fernando Boada, and Tamer S. Ibrahim, “Maximizing RF Efficiency and Minimizing Eddy Current Artifacts Using RF and Eddy Current Simulations”, ISMRM Annual Meeting, Melbourne, Australia, May 2012, p 0536.
- Yujuan Zhao, Tiejun Zhao, Daniel Stough, Chad Harris, William Handler, Hai Zheng, Shaohua Lin, Fernando Boada, Blaine Chronik, and Tamer Ibrahim, “Simulation and

experimental verification of eddy current due to RF coil shielding” , The 20th ISMRM Annual Meeting, Melbourne, Australia, May 2012, p 2759.

Chapter 7 summarizes the results and proposes future work. In addition, the significant contributions of this dissertation are explained in detail.

2.0 BACKGROUND

2.1 BRAIN COMPUTER INTERFACE

2.1.1 Brain Computer Interfaces Review

BCIs provide direct communication pathways between a subject's brain and external devices (a computer, prosthesis, wheelchair or other device) via electrodes. The pathways include 1) translating a signal from a neuron and 2) converting and inputting diagnosing signals into the human brain. Through the first pathway, BCI recording devices help neurophysiologists extract information from the neural activities and correlate them to the brain's thoughts, emotions, or other mental states. Through the second pathway, implanted BCI devices assist in realizing deep brain stimulation.

The first pathway will be the major BCI format discussed in this dissertation. For this kind of BCIs, brain activity rhythms, evoked potentials, steady state visually evoked potentials and P300 evoked potential (24) are the useful signals to measure and characterize neuron activities. Neuron activities are normally analyzed by signal processing, feature extraction, feature selection and feature classification.

Specific applications include medical diagnostics (25), brain function studies (26), function recoveries (27), external device controls and treatment of diseases such as profound

deafness (28) and Parkinson's disease (29). BCIs designed for non-medical purposes (healthy users) have also attracted considerable interest, and BCIs in gaming applications are some of the most popular (30).

The various classes of BCIs can be distinguished by their level of invasiveness (non-invasive or invasive) (31). Non-invasive systems primarily record electroencephalograms (EEGs) (25) from the scalp surface. The signals provided by EEGs are typically weak, since the signals are transmitted across different tissue layers and each tissue layer has high conductivity (32). Three other non-invasive technologies are magnetoencephalography (MEG), functional magnetic resonance imaging (fMRI) and near infrared spectroscopy (NIRS). MEG and fMRI technologies require a magnetic field environment; NIRS and fMRI have poor temporal resolution (25). In contrast, invasive BCIs can detect the activity of small areas of the brain or even individual neurons. For example, for Electrocorticography (ECoG), the electrodes are placed directly on the surface of the brain to record electrical activity from the cerebral cortex. They can provide very good signal quality (high level of amplitude, low-noise) and very good spatial resolution.

2.1.2 Brain Computer Interface Architecture

A BCI system has four major components: 1) a signal acquisition system including electrodes and other circuitries which acquire signals from the brain; 2) a signal processing system which extracts signal features from the brain, selects features and translates them into device commands; 3) an output device that sends device commands to the external devices; and 4) an operating protocol that guides users' operation and controls the sequence and speed of interactions between user and system.

The development of electronics and telecommunication research during the last decade has allowed the clinical application of BCIs to steadily advance. The achievements of stable signal probes and enormous integrated circuit chips accelerated the realization of BCI implantation. The BCI's wireless data communication technique facilitates real time neural activity signal processing and decoding into command signals. However, wired power connection is a huge impediment for the clinical application of BCIs. Most current BCIs have only been designed for immobile users in a carefully controlled environment.

2.2 IMPLANTED ANTENNA WITHIN THE HUMAN ENVIRONMENT

2.2.1 Antenna Geometry and Miniaturization Techniques

In antenna theory, antennas can be divided into six groups according their structure type: wire antennas, microstrip antennas, aperture antennas, array antennas, reflector antennas and lens antennas (33). Among them, wire antenna and microstrip antenna are commonly designed as antenna for implanted medical devices. For wire antennas, there are various shapes, such as straight wire (like a dipole), loop and helix. The classic dipole antenna has been used for diverse theoretical and basic studies, but it is not suitable for implantation use since it requires a large stiff extension from the implanted medical devices. For microstrip antennas, their drawback is that the physical volume of this antenna is difficult to reduce because of the need of a dielectric substrate material to separate the metal and ground plane. Therefore, miniaturization techniques should be used to modify classical antenna dimensions and geometries while maintaining the desired radiation performance.

Miniaturization techniques (34) include lumped-element loaded antennas, antennas loaded with materials, using ground planes and short circuits, and adding slots and notches. Among these techniques, dielectric loading, the use of grounding planes (like planar inverted-F antennas) and normal-mode helical antennas have been shown to be very effective ways of reducing the dimensions of antennas.

2.2.2 Wireless Data Transmission and Power Transmission

Antenna and RF wave propagation techniques have already been applied in BCI. For example, Chae et al realized the transfer of raw data from 128 recording channels at a data rate of 90Mb/s by using RF technology (35). For RF telemetry data communication or wireless data transfer, maximum available power is calculated to characterize the performance of a communication link between the designed antennas and an exterior antenna: when the delivered power is 1W, the radiated power in the head model is 0.0057W (36). This indicates that the power could be transferred into a human head through RF waves.

Although wireless RF power transfer will use implanted-antenna techniques and wave propagation theory as well, the aim of energy transfer is different from the aim of transmission of data information. For wireless power transfer, the gain of the antenna is the most important design parameter. This is in contrast to an antenna used to transfer wireless data in which the crucial design parameter is the data rate/bandwidth. The design method of a wireless energy antenna could be totally different than the design of an antenna for telemetry communication. The proposed research will present techniques on how to optimize the designs of implanted antenna in order to miniaturize the antennas' dimensions and at the same time keep good radiation performance.

Thanks to the development of integrated circuits (ICs) and microelectromechanical system (MEMS) techniques, an implanted BCI system consumes less and less power: B. Gosselin proposed a circuit working in the sub-microwatt range and it dissipated just 780nW of power in 0.07 mm²(37). With the lower threshold value of the power supply for implanted BMI system set as 780nW for 0.07 mm², this could mean that for a 1mm by 2mm chip, only about 30μW of power is needed.

2.2.3 RF Safety

The upper threshold value of the power supply from the wireless power transfer system would be limited by safety regulations. Human tissue is a special environment: layered tissue with high conductivity and high permittivity. RF power absorption in the tissue may lead to an increase in temperature, which may cause damages at the cellular level. SAR and temperature increment in brain tissues will be characterized to ensure they meet the guidelines proposed by FCC/FDA/IEC. The temperature change in the human brain due to the operation of an internal antenna is evaluated (38). As thermal heating due to SAR was insignificant, this study suggests that wireless electromagnetic, i.e. RF, may be a viable option for brain machine interfaces in clinical applications.

2.3 MAGNETIC RESONANCE IMAGING

Spin is a physical property of nuclear particles: electrons spin on their own axis and orbit the nucleus; the nucleus spins about its own axis. For MR active nuclei (nuclei with odd mass

numbers), spin directions are not equal and opposite; hence the nucleus has a net spin. MR active nuclei act like magnet dipoles with spinning motion; therefore they will acquire a magnetic moment. Normally the magnetic moments are randomly oriented. They will align their axis of rotation when there is an external magnetic field. Low-energy nuclei align their magnetic moments parallel to the applied external field (spin-up) and high-energy nuclei align their magnetic moments in anti-parallel (spin-down) fashion. High-energy nuclei are always less than low-energy nuclei; this relative difference produces a net magnetic moment vector. Protium (H^1) has one proton and it is the MR active nucleus widely used in clinical MRI, because hydrogen (H) is very abundant in the human body and it can create a significant magnetic moment vector which is called net magnetization vector (NMV). NMV is the reason for a detectable MR signal; visible tissue contrast is generated by the differences of the NMV inside different tissues.

2.3.1 Static Magnetic Field

The static external magnetic field is called B_0 and is applied along the Z direction in most contemporary commercial scanners. MRI systems primarily use a superconducting electromagnet to generate the static magnetic field. This field generates an additional spin of the NMV following a circle path around B_0 , which is called precession. The precessional frequency is known as the Larmor frequency (ω). The strength of the static magnetic field determines the quantities of the spin-up and spin-down nuclei; Larmor frequency is linearly related to the B_0 strength and defined as:

$$\omega = \gamma B_0 \quad (2-1)$$

where γ is the gyromagnetic ratio, which is a constant for any given nucleus. For proton MRI, it is 42.56 MHz/Tesla. 1.5 Tesla and 3.0 Tesla are most commonly used in the clinical environment. For a research system, field strengths up to 16 Tesla are obtainable.

2.3.2 RF Excitation

When an oscillating perturbation is applied on a nucleus (for MR system, refers to the proton in H^1 , since there is no neutron), the nucleus will gain energy. If the energy is delivered at the precessional frequency, the nucleus will resonate at the Larmor frequency. This phenomenon is called resonance. In a MRI system, the energy at the Larmor frequency is normally carried by an RF pulse and is generated by a transmit RF coil. Some spin-down nuclei that have gained energy will become spin-up nuclei. Therefore the absorbed energy is used to increase the number of spin-down hydrogen nuclei and this procedure is called RF excitation. The resonance also moves the NMV out of B_0 direction Z with some flip angle. The flip angle depends on the RF pulse energy and duration. The angled NMV will induce a voltage in a receive RF coil based on Faraday's Law. When the RF pulse is switched off, the NMV will move back to the B_0 direction after a period of time, and this procedure is called relaxation. T_1 (spin-lattice relaxation) and T_2 (spin-spin relaxation) measure the recovery time of longitudinal magnetization (Z direction) and decay time of transverse magnetization (XY plane). Images obtain tissue contrast mainly through T_1 recovery, T_2 decay and proton density.

2.3.3 RF Coils

RF Coils are used to achieve and detect proton resonance. Based on the coil function, the coils that transmit signals are named transmit coils and the coils used to detect signals are named receive coils; and the coils used for transmit and receive at the same time are called transceivers. Based on the coil excited field pattern, coils can be divided into volume coils, which excite the entire region of interest, and surface coils, which excite the localized region of interest. The birdcage coil (39) is one of the most famous commercial volume coil designs for 1.5 Tesla and 3 Tesla MRI. The transverse electromagnetic (TEM) resonator (40) uses transmission lines to reach the resonance. Dielectric resonators (41) are based on hollow cylinders and their intrinsic capacitive and inductive characters of the cylinder constitute the modes of the cavity; the modes that carry energy at specific directions and specific modes are normally useful in MR. Travelling-wave (42) can generate a more uniform coverage. Transmit and receive arrays are widely used in contemporary MRI systems to increase excitation homogeneity and to increase signal to noise ratio (SNR) respectively (43-46). In this dissertation, a new transmit array is and optimized to generate a homogeneous field distribution. The coil performance is compared with TEM performance.

RF coils are also known as RF resonators. The resonant frequency is given by:

$$f = \frac{1}{2\pi\sqrt{LC}} \quad (2-2)$$

where L is the inductance of the coil and C is the capacitance of the coil.

The field generated from RF coil is:

$$\vec{B}_1 = \bar{x}B_{1x} + \bar{y}B_{1y} + \bar{z}B_{1z} \quad (2-3)$$

From an electromagnetic perspective, only the clockwise circularly polarized component at transverse plane (XY plane) can be used for RF excitation (47) and the transmit field is represented as:

$$B_1^+ = \frac{B_{1x} + jB_{1y}}{\sqrt{2}} \quad (2-4)$$

Receive field is represented as:

$$B_1^- = \frac{B_{1x} - jB_{1y}}{\sqrt{2}} \quad (2-5)$$

In this dissertation, MRI transmit fields generated from the simulation are all calculated using equation (2-4).

2.3.4 Spatial Encoding

Spatial encoding is achieved by the superimposition of linearly-varying gradient fields upon the uniform static magnetic field, so MR frequency varies linearly with spatial position. Fourier transformation of the received signal can separate signals from each frequency and represent the signal intensity at one specific physical position. Gradient coils are the hardware used to generate the linearly-varying gradient fields and to produce 2D/3D images. There are normally three orthogonal gradient coils (X, Y, Z) used for phase encoding, frequency encoding and slice selection respectively. The gradient coil structures discussed in this dissertation will be shown in Chapter 6.

2.3.5 Pulse and Sequence Design

RF pulse conveys the RF energy and can create a torque to rotate magnetic moment towards the transverse (XY) plane. It's designed to resonate with the Larmor frequency to deliver the energy. Slice-selective SINC pulse is the most often used RF pulse, where it excites spins within a slice. Multi-dimensional spatial-selective pulses or spectral-spatial pulses can also be applied in MR system. The behavior of RF pulses can be illuminated by the Bloch equation:

$$\frac{d\vec{M}}{dt} = \gamma\vec{M} \times \vec{B} - \frac{M_x\vec{i} + M_y\vec{j}}{T_2} - \frac{(M_z + M_0)\vec{k}}{T_1} \quad (2-6)$$

where \vec{M} is magnetization, \vec{B} is the combined magnetic field vector from three types of the magnetic field: static field B_0 , gradient field, and RF field B_1 . There is no closed form solution for the Bloch equation for the B_1 field by given the desired magnetization pattern and gradients waveforms. Therefore, for specific applications, different methods have been used to solve the Bloch equation and design RF pulses based on various assumptions. For small-flip-angle pulse design, $\vec{M}_z \approx \vec{M}_0$. Large flip angle pulse design depends on the method used to solve the nonlinear Bloch equation; higher order terms have to be added to reduce image distortions.

Sequence is a combination of RF pulses and gradients and it controls the way a MR system applies the pulses and gradients. There are many different sequences available and designed for specific applications. The major aim of a sequence design is pursue a particular tissue contrast with minimal artifacts as quick as possible. Pulse sequences are normally divided into two categories: Spin Echo pulse sequences and Gradient echo sequences. The main difference between these two sequences is the way the echo or spin re-phase is achieved.

2.4 FINITE DIFFERENCE TIME DOMAIN METHOD

The finite-difference time-domain method (FDTD) employs finite differences as approximations to both the spatial and temporal derivatives in Maxwell's equations. It is a full-wave electromagnetic computational method. It has been widely used to study the interaction between RF waves and human biological-tissues (48-56). In this dissertation, FDTD is used to calculate implanted antenna performance (Chapter 3), and MRI RF coil transmit field distributions (Chapter 4, 5, 6).

2.4.1 The Finite-Difference Time-Domain formulation

The FDTD algorithm was introduced by Kane Yee in 1966 (57). The basic idea is to solve the electric and magnetic fields in the time and space using the coupled Maxwell's curl equations. The differential operators of the curl equations are replaced by second-order accurate central difference approximations. Yee Cells (57) are selected to spatially sampling the electric and magnetic field vector components.

Maxwell's equations (58) in linear, isotropic and non-dispersive materials are given as:

$$\nabla \times \vec{E} = -\frac{\partial \vec{B}}{\partial t} - \vec{M} \quad (2-7)$$

$$\nabla \times \vec{H} = \frac{\partial \vec{D}}{\partial t} + \vec{J} \quad (2-8)$$

$$\nabla \cdot \vec{D} = \rho_e \quad (2-9)$$

$$\nabla \cdot \vec{B} = \rho_m \quad (2-10)$$

Electric and magnetic flux densities are:

$$\vec{D} = \epsilon \vec{E} \quad (2-11)$$

$$\vec{B} = \mu \vec{H} \quad (2-12)$$

Electric and equivalent magnetic current densities are:

$$\vec{M} = \vec{M}_{source} + \sigma^* \vec{H} \quad (2-13)$$

$$\vec{J} = \vec{J}_{source} + \sigma \vec{E} \quad (2-14)$$

where

\vec{E} : electric field (volts/meter)

\vec{D} : electric flux density (coulombs/ meter²)

\vec{H} : magnetic field (amperes/meter)

\vec{B} : magnetic flux density (webers/ meter²)

\vec{J} : electric current density (amperes/ meter²)

\vec{M} : equivalent magnetic current density (volts/ meter²)

ϵ : electrical permittivity (farads /meter)

μ : magnetic permeability (henrys /meter)

σ : electric conductivity (siemens / meter)

σ^* : equivalent magnetic loss (ohms /meter)

ρ_e : electric charge density (coulombs / meter³)

ρ_m : magnetic charge density (weber/ meter³)

For FDTD algorithm, Faraday's Law (2-7) and Ampere-Maxwell equation (2-8) will be used to solve the wave equation. For general three-dimensional objects, the curl operators in Cartesian coordinates can be rewritten as six coupled scalar equations:

$$\mu \frac{\partial H_x}{\partial t} = \frac{\partial E_y}{\partial z} - \frac{\partial E_z}{\partial y} - (M_{source_x} + \sigma^* H_x) \quad (2-15)$$

$$\mu \frac{\partial H_y}{\partial t} = \frac{\partial E_z}{\partial x} - \frac{\partial E_x}{\partial z} - (M_{source_y} + \sigma^* H_y) \quad (2-16)$$

$$\mu \frac{\partial H_z}{\partial t} = \frac{\partial E_x}{\partial y} - \frac{\partial E_y}{\partial x} - (M_{source_z} + \sigma^* H_z) \quad (2-17)$$

$$\varepsilon \frac{\partial E_x}{\partial t} = \frac{\partial H_z}{\partial y} - \frac{\partial H_y}{\partial z} - (J_{source_x} + \sigma E_x) \quad (2-18)$$

$$\varepsilon \frac{\partial E_y}{\partial t} = \frac{\partial H_x}{\partial z} - \frac{\partial H_z}{\partial x} - (J_{source_y} + \sigma E_y) \quad (2-19)$$

$$\varepsilon \frac{\partial E_z}{\partial t} = \frac{\partial H_y}{\partial x} - \frac{\partial H_x}{\partial y} - (J_{source_z} + \sigma E_z) \quad (2-20)$$

where H_x is the magnetic field in x direction and the other components following the same naming format.

Yee introduced notation (58) to represent a space point and time point for any function u as $u(i\Delta x, j\Delta y, k\Delta z, n\Delta t) = u^n(i, j, k)$, where Δx , Δy and Δz are the space increments in the X, Y and Z coordinate directions, Δt is the time increment, i, j, k and m are integers. Central-difference expressions (obtained from Taylor's theorem) for the space (X direction as the following example) and time derivatives for the function u are shown below respectively:

$$\frac{\partial u}{\partial x}(i\Delta x, j\Delta y, k\Delta z, n\Delta t) = \frac{u^n(i+1/2, j, k) - u^n(i-1/2, j, k)}{\Delta x} + O((\Delta x)^2) \quad (2-21)$$

$$\frac{\partial u}{\partial t}(i\Delta x, j\Delta y, k\Delta z, m\Delta t) = \frac{u^{m+1/2}(i, j, k) - u^{m-1/2}(i, j, k)}{\Delta t} + O((\Delta t)^2) \quad (2-22)$$

To achieve second-order accuracy, the error term $O((\Delta x)^2)$ and $O((\Delta t)^2)$ can be dropped. Therefore, the FDTD equations become:

$$\begin{aligned}
E_x^{n+1}(i + \frac{1}{2}, j, k) &= \left(\frac{2\varepsilon - \sigma\Delta t}{2\varepsilon + \sigma\Delta t} \right) E_x^n(i + \frac{1}{2}, j, k) + \left(\frac{2\Delta t}{2\varepsilon + \sigma\Delta t} \right) \\
&\left[\frac{H_z^{n+\frac{1}{2}}(i + \frac{1}{2}, j + \frac{1}{2}, k) - H_z^{n+\frac{1}{2}}(i + \frac{1}{2}, j - \frac{1}{2}, k)}{\Delta y} - \right. \\
&\left. \frac{H_y^{n+\frac{1}{2}}(i + \frac{1}{2}, j, k + \frac{1}{2}) - H_y^{n+\frac{1}{2}}(i + \frac{1}{2}, j, k - \frac{1}{2})}{\Delta z} - J_{source_x}^{n+\frac{1}{2}}(i + \frac{1}{2}, j, k) \right]
\end{aligned} \tag{2-23}$$

$$\begin{aligned}
E_y^{n+1}(i, j + \frac{1}{2}, k) &= \left(\frac{2\varepsilon - \sigma\Delta t}{2\varepsilon + \sigma\Delta t} \right) E_y^n(i, j + \frac{1}{2}, k) + \left(\frac{2\Delta t}{2\varepsilon + \sigma\Delta t} \right) \\
&\left[\frac{H_x^{n+\frac{1}{2}}(i, j + \frac{1}{2}, k + \frac{1}{2}) - H_x^{n+\frac{1}{2}}(i, j + \frac{1}{2}, k - \frac{1}{2})}{\Delta z} - \right. \\
&\left. \frac{H_z^{n+\frac{1}{2}}(i + \frac{1}{2}, j + \frac{1}{2}, k) - H_z^{n+\frac{1}{2}}(i - \frac{1}{2}, j + \frac{1}{2}, k)}{\Delta x} - J_{source_y}^{n+\frac{1}{2}}(i, j + \frac{1}{2}, k) \right]
\end{aligned} \tag{2-24}$$

$$\begin{aligned}
E_z^{n+1}(i, j, k + \frac{1}{2}) &= \left(\frac{2\varepsilon - \sigma\Delta t}{2\varepsilon + \sigma\Delta t} \right) E_z^n(i, j, k + \frac{1}{2}) + \left(\frac{2\Delta t}{2\varepsilon + \sigma\Delta t} \right) \\
&\left[\frac{H_y^{n+\frac{1}{2}}(i + \frac{1}{2}, j, k + \frac{1}{2}) - H_y^{n+\frac{1}{2}}(i - \frac{1}{2}, j, k + \frac{1}{2})}{\Delta x} - \right. \\
&\left. \frac{H_x^{n+\frac{1}{2}}(i, j + \frac{1}{2}, k + \frac{1}{2}) - H_x^{n+\frac{1}{2}}(i, j - \frac{1}{2}, k + \frac{1}{2})}{\Delta y} - J_{source_z}^{n+\frac{1}{2}}(i, j, k + \frac{1}{2}) \right]
\end{aligned} \tag{2-25}$$

$$\begin{aligned}
H_x^{n+\frac{1}{2}}(i, j + \frac{1}{2}, k + \frac{1}{2}) &= \left(\frac{2\mu - \sigma^* \Delta t}{2\mu + \sigma^* \Delta t} \right) H_x^{n-\frac{1}{2}}(i, j + \frac{1}{2}, k + \frac{1}{2}) + \left(\frac{2\Delta t}{2\mu + \sigma^* \Delta t} \right) \\
&\left[\frac{E_y^n(i, j + \frac{1}{2}, k + 1) - E_y^n(i, j + \frac{1}{2}, k)}{\Delta z} - \right. \\
&\left. \frac{E_z^n(i, j + 1, k + \frac{1}{2}) - E_z^n(i, j, k + \frac{1}{2})}{\Delta y} - M_{source_x}^n(i, j + \frac{1}{2}, k + \frac{1}{2}) \right]
\end{aligned} \tag{2-26}$$

$$\begin{aligned}
H_y^{n+\frac{1}{2}}(i + \frac{1}{2}, j, k + \frac{1}{2}) &= \left(\frac{2\mu - \sigma^* \Delta t}{2\mu + \sigma^* \Delta t} \right) H_y^{n-\frac{1}{2}}(i + \frac{1}{2}, j, k + \frac{1}{2}) + \left(\frac{2\Delta t}{2\mu + \sigma^* \Delta t} \right) \\
&\left[\frac{E_z^n(i + 1, j + \frac{1}{2}, k + \frac{1}{2}) - E_z^n(i, j + \frac{1}{2}, k + \frac{1}{2})}{\Delta x} - \right. \\
&\left. \frac{E_x^n(i + \frac{1}{2}, j, k + 1) - E_x^n(i + \frac{1}{2}, j, k)}{\Delta z} - M_{source_y}^n(i + \frac{1}{2}, j, k + \frac{1}{2}) \right]
\end{aligned} \tag{2-27}$$

$$\begin{aligned}
H_z^{n+\frac{1}{2}}(i + \frac{1}{2}, j + \frac{1}{2}, k) &= \left(\frac{2\mu - \sigma^* \Delta t}{2\mu + \sigma^* \Delta t} \right) H_z^{n-\frac{1}{2}}(i + \frac{1}{2}, j + \frac{1}{2}, k) + \left(\frac{2\Delta t}{2\mu + \sigma^* \Delta t} \right) \\
&\left[\frac{E_x^n(i + \frac{1}{2}, j + 1, k) - E_x^n(i + \frac{1}{2}, j, k)}{\Delta y} - \right. \\
&\left. \frac{E_y^n(i + 1, j + \frac{1}{2}, k) - E_y^n(i, j + \frac{1}{2}, k)}{\Delta x} - M_{source_z}^n(i + \frac{1}{2}, j + \frac{1}{2}, k) \right]
\end{aligned} \tag{2-28}$$

Position of the electric and magnetic field vector components about a cubic unit cell of the Yee space lattice are shown in Figure 2.1. Field component is a function of its one-time-step-before value and the half-time-step-before of the surrounding fields. For electric field components, the surrounding fields are magnetic field components; for magnetic field

components, the surrounding fields are electric field components. Spatial step is chosen based on the minimum wavelength of the problem; a good choice of the spatial step is: $\frac{\lambda_{\min}}{(15 \sim 20)}$,

where λ_{\min} is the minimum wavelength inside the medium. The time step is chosen based on

Courant-Friedrichs stability criterion; $\Delta t \leq \frac{1}{v_{\max} \sqrt{\frac{1}{(\Delta x)^2 + (\Delta y)^2 + (\Delta z)^2}}}$, where v_{\max} is the

maximum wave speed inside the medium.

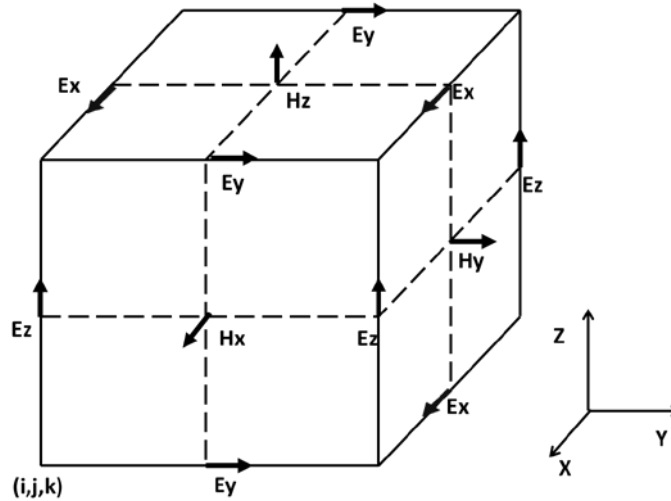


Figure 2.1: Electric and magnetic field vector components with a Yee cell at (i,j,k) position

2.4.2 One Dimensional Transmission Line Excitation

Accurately realizing the electromagnetic wave excitation is a generic issue in FDTD modeling.

A simple model is often used for the feed region of the antenna to save computational resources or to separate the analysis of the antenna from the balun. In the most often configuration, hard-sourced E and H fields, J and M current sources and waveguide sources have been discussed

(58). Another feed model is a one-dimensional transmission line (59) and the computer run-time is significant less than that of the hard source (60). The coaxial cable is modeled with the use of the transmission line equations given by (61):

$$I^{n+\frac{1}{2}}(k'+\frac{1}{2}) = I^{n-\frac{1}{2}}(k'+\frac{1}{2}) - \frac{1}{Z_0} \frac{v\Delta t}{\Delta z} [V^n(k'+1) - V^n(k')] \quad (2-29)$$

$$V^{n+1}(k') = V^n(k') - Z_0 \frac{v\Delta t}{\Delta z} \left[I^{n+\frac{1}{2}}(k'+\frac{1}{2}) - I^{n+\frac{1}{2}}(k'-\frac{1}{2}) \right] \quad (2-30)$$

where V is voltage and I is current inside the transmission line, Z_0 is the characteristic impedance, v is the phase velocity in the transmission line and Δz is the spatial step. The bottom of the transmission line will be terminated by an absorbing boundary condition. Source is defined at $k' > 0$.

At the aperture $k' = k'_{top}$ shown in Figure 2.2, the current is calculated from the magnetic field and voltage is used to update the electric field.

$$I^{n+\frac{1}{2}}(k'_{top} + \frac{1}{2}) = -\Delta z [H_z^{n+\frac{1}{2}}(i_a, j_a + \frac{1}{2}, k_a) - H_z^{n+\frac{1}{2}}(i_a, j_a - \frac{1}{2}, k_a)] \quad (2-31)$$

$$+ \Delta y [H_y^{n+\frac{1}{2}}(i_a, j_a, k_a + \frac{1}{2}) - H_y^{n+\frac{1}{2}}(i_a, j_a, k_a - \frac{1}{2})]$$

$$V^n(k'_{top}) = -\Delta x \left[E_z^n(i_a, j_a + \frac{1}{2}, k_a) \right] \quad (2-32)$$

where i_a , j_a and k_a are the transmission line positions at x, y and z directions.

This hybrid algorithm (1D transmission line and 3D FDTD Yee cell) is conditionally stable. Continuous adjustment has to be done according to the geometry, structure and properties of the object in the calculation. Therefore it is not used in commercial FDTD software. In this

dissertation, the stability is carefully tuned for BCIs and MRI applications to simulate the coaxial cable transmission line excitation.

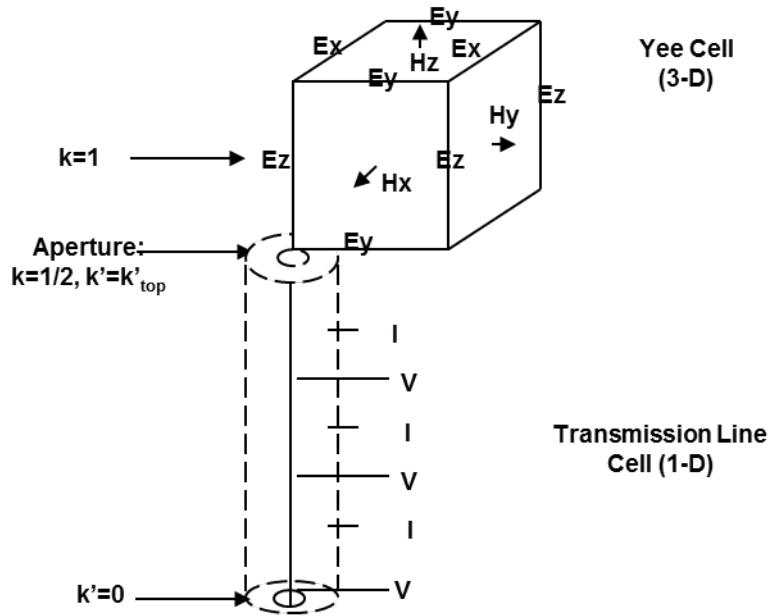


Figure 2.2: The 1D transmission line model to the 3D grid

2.5 FINITE ELEMENT METHOD

Finite element method (FEM) is a great tool to solve thermal, fluid dynamics, and electromagnetic problems. This method stems from Ritz 1909 (62) and Courant 1943 (63). Clough introduced the term “finite element” for the first time in the paper “The finite element method in plane stress analysis” (64). In this dissertation, FEM is used to calculate low frequency gradient field generated eddy currents’ performance (Chapter 6).

2.5.1 Finite Elements in Electromagnetics

FEM is very popular for solving electromagnetic fields, particularly in a region that has curved surfaces. This is because the curved surface can be modeled perfectly by triangles and quadrilaterals. The method is to discretize a complex problem domain into a collection of simple structure element (mesh). Then these sub-element equations are recombined into a global system equation (governing equation or stiffness matrix). The global equation together with initial values and boundary conditions will be solved to obtain the numerical solutions of the problem. The fundamental idea of this method is to evaluate the energy in all the elements and then minimize it. The widely used mathematics methods to create the equations are projective solution and variational reformulations.

In the electromagnetic problem, the four Maxwell's equation (2-7) - (2-10) can be reduced to two wave equations:

$$\nabla^2 \vec{E} = \mu\sigma \frac{\partial \vec{E}}{\partial t} + \mu\varepsilon \frac{\partial^2 \vec{E}}{\partial t^2} - \nabla \left(\frac{\rho}{\varepsilon} \right) \quad (2-33)$$

$$\nabla^2 \vec{H} = \mu\sigma \frac{\partial \vec{H}}{\partial t} + \mu\varepsilon \frac{\partial^2 \vec{H}}{\partial t^2} \quad (2-34)$$

In electrostatic regime, they can be reduced into a Poisson problem:

$$\nabla^2 \vec{E} = -\nabla \left(\frac{\rho}{\varepsilon} \right) \quad (2-35)$$

or

$$\nabla^2 V = -\nabla \left(\frac{\rho}{\varepsilon} \right) \quad (2-36)$$

When there is no charge, it becomes Laplace's equation:

$$\nabla^2 V = 0 \quad (2-37)$$

For cases that an object is very small compared to a wavelength, quasi-static approximations generally provide more efficient solutions.

FEM will be used to solve those electromagnetic differential equations. For a 2D problem, the elements are triangle or quadrilaterals having a node at each corner; for a 3D problem, tetrahedra, bricks, and prisms are most common choices. The size and shape of the elements could be various to achieve a given degree of accuracy. The elements are transformed to a set of normalized local coordinates. Local basis function then can be written in a concise form. Interpolation function is usually implemented as scalar basis function and edge element is usually for vector basis function. Computer programs are used to generate the mesh of nodes and automatically index the elements and nodes. Sub-matrix is calculated for each element. The global system combines the submatrix of each element and then the problem is reduced to solve one full matrix problem. Often times, high percentage of the entries of the stiffness matrix is zero, so sparse matrix solutions have been used for a lot of cases. Iterative solver is implemented to solve the sparse matrix equation. The output from the finite element should converge to a unique correct solution; normally at least two solutions to the same problem are checked: a solution compares with another one of increased accuracy. In classical FEM, convergence is obtained by global or local refinement of the fundamental mesh. In this process, the order of approximation on each element is fixed; the error in the numerical solution can be reduced by increasing the number of unknowns (meshes). High order FEM increases the polynomial order for each element when mesh is fixed and it can reduce the error too.

3.0 IMPLANTED MINIATURIZED ANTENNA FOR BRAIN COMPUTER INTERFACE APPLICATIONS

3.1 INTRODUCTION

Brain Computer Interfaces (BCIs) are devices designed to establish a communication link between the human brain and neuroprosthetic devices to assist individuals with neurological conditions. However, because of the limitation of the power supply, most BCIs require a direct power connection with the external devices. The BCIs could only be kept implanted inside the subjects' brain for a very limited time, which limits functionality and therefore limits the clinical applications.

Batteries can be used as BCI power supply units (60,65,66). However, batteries present significant challenges due to the size, mass, toxic composition, and finite lifetime. There are several research groups using the inductive coupling method to transfer the power wirelessly (67-69). The coupling coils have been typically designed to operate at 10 MHz or below (quasi-static conditions). The drawback of the inductive coupling is that its transmission mainly depends on the changing of magnetic field flux, which requires a relatively large (diameter of several centimeters) implanted coil precisely aligned with an external coil. The maximum distance between two coupling coils is limited to approximately one centimeter in order to maintain effective coupling results (70).

There are some groups studying implanted antennas to transmit data wirelessly into the human body (36,71-76). Most of these implanted antennas have been designed to operate at the medical implant communication service (MICS) band of 402-405 MHz. The implantable small profile patch antennas' characteristics and their radiation were evaluated (36,71). The transmission and reflection of microstrip antennas affected by different superstrates and substrates were studied (72), through numerical analysis and measurements. The effects of different inner insulating layers and external insulating layers and power loss were discussed (73) analytically, using a spherical model. Besides, the radiation efficiency impacts of insulating layers were presented (74). For GHz and above operating frequencies, the impact of the coating on antenna performance was studied by an implanted antenna radiation measurement setup (75). A pair of microstrip antennas working at microwave frequencies (1.45 GHz and 2.45 GHz) established a data telemetry link for a dual-unit retinal prosthesis (76).

Recent research reveals that the electromagnetic field penetration depth inside the tissue can be asymptotically independent of frequency at high frequencies, and the optimal frequency for the millimeter sized implanted antennas is in the gigahertz range (77). An implanted antenna operating in the gigahertz range could be designed into a very small profile and also solve the difficulties in designing efficient high data rate (78). Therefore, an implanted antenna (operating in the gigahertz range) provides a promising approach to accomplish long term implantation of a BCI in users as well as allowing the efficient transmission of power.

Most of the abovementioned works are assuming that the implanted antennas are connected with 50 Ohm transmission lines. It is noted however, that the ratio between received RF power and tissue absorption depends on the input impedance of the receive antenna (77). To realize the conjugate matching (i.e. optimal performance), the antenna loads including connected

wires and implanted chips could be designed to other values rather than being restricted to 50 Ohms. For example the optimal choice was a 5.6 Ohms load in Poon's study (77). In our work, we simulate and characterize the input impedance of the implanted BCI RF power receiving antenna operating above 1GHz. The input impedance and efficiency of wireless implanted antenna is evaluated for different 1) thickness of insulating layers 2) dielectric properties of insulating layers 3) location of implants, and 4) tissue compositions. Lastly, three miniaturized implanted antenna designs are compared and the maximum received power under the SAR regulations are calculated based on the FDTD simulation results.

3.2 MATERIALS AND METHODS

3.2.1 FDTD Simulation and the Transmission Line Feed Model

The input impedance of an antenna of the classic structure could be calculated analytically when the antenna is placed in free space, buried in materials (79), or even when an insulated antenna is embedded inside a homogeneous lossy material (80). However, it is extremely challenging to analytically calculate the impedance of an insulated antenna with arbitrary structures embedded in the human brain, which integrates many different lossy tissue materials.

The FDTD method has great advantages for simulating interactions of electromagnetic waves with biological tissues (81). In this work, a one dimensional transmission line feed model (58,60) is implemented into our in-house three dimensional (3D) FDTD method package in order to study the input impedance of the implanted antenna. This simulation package developed in Dr. Ibrahim's Laboratory has been widely utilized and verified in many papers (49,51,82,83).

The perfectly matched layers (PML) are used as the absorbing boundary conditions and the power radiated from the antenna in the FDTD model propagates similarly as it does in the lossless/lossy medium of infinite extent. The material of the antenna is simulated as a perfect electric conductor (PEC) to model very good conducting materials. To get accurate computational results, the integration contour of the currents is shifted one cell from the antenna drive point to avoid the electric fringing field in the gap (60). To analyze the ultra-thin (micrometers) insulating layers effects on the antennas performance, thin material sheets are modeled using a three dimensional sub-cell modeling formula in FDTD (84). This efficient sub-cell modeling method removes the limitation that spatial information should be much larger than the cell grid and therefore greatly reduce the computer storage requirement and computational time.

At the feeding location, the antenna is excited by the virtual transmission line (85), which is injected with a differentiated Gaussian pulse with sufficient frequency content around the intended operational frequency. The differentiated Gaussian pulse is:

$$G(t) = \frac{1}{T \times 10^{-12}} (t - S \times T \times 10^{-9}) \exp\left(-\left(\frac{t - S \times T \times 10^{-9}}{T \times 10^{-9}}\right)^2\right) \quad (3-1)$$

The parameter T affects the pulse-width and the time delay of the pulse. S is a temporal delay parameter. A set of suitable parameters for S (5.8) and T (0.1) have been chosen for a wideband spectrum of frequencies ranging from 1GHz to 4GHz according to the geometries of the antennas to be simulated.

3.2.2 Antenna Geometry and Antenna Performance Parameters

The antenna reciprocity theorem (33) guarantees that a good transmitting antenna is also a good receiving antenna. The transmission/radiation efficiency is in part proportional to the radiation resistance (33,74). Generally for one specific antenna design, the radiation resistance of the antenna increases when the antenna size is larger (86). In addition, the chip circuitry (attached to the implanted antenna) typically possesses high input impedance values (~80-200 Ohms). Therefore, for efficient operation (minimal mismatch), it is highly favorable to have the input impedance of the implanted antenna in the same range (~80-200 Ohms). The input impedance of a folded dipole antenna is approximately four times the impedance of a dipole antenna when the length of the folded dipole equals to half wavelength (33), which is on the order of about 300 Ohm in the free space. As a result, a modified folded dipole antenna (rectangular antenna) was chosen for the following analysis.

Due to the inhomogeneous and lossy environment (human head), the relation between power reception and the implantation depth of the antenna does not strictly follow the Friis transmission formula as it is not a far field RF problem. Therefore the radiation pattern is not used to study the antennas' performance in this work. Since the RF power is absorbed by the body and can result in tissue heating, the major concern about the wirelessly powering the BCI devices is mainly related to this safety issue. As a result, the main performance parameter of the BCI implanted antennas mainly depends on power reception in relation to tissue absorption i.e. SAR rise. Thus any geometry/feeding design of the antenna will aim at achieving maximum power reception for a given local SAR. Furthermore, from circuit theory, a maximum transfer of power from a given voltage source to a load occurs when the load impedance is the complex conjugate of the source impedance. Therefore, the input impedance of the implanted antenna is

studied as the major power transmission indicator. The antennas can be used at any frequency where they exhibit enough power receptivity for a given local SAR. The input impedance and the received power of the implanted antenna are calculated through voltage and current information from the transmission line feed model (58,60) used in this study.

3.2.3 Human Head Model

Antennas are implanted inside a 3D 19 materials head model which is developed from 1.5 tesla MRI images (87). The tissue properties are defined (49) based on the study (88). In order to compare the different effects of phantoms and the head model, two phantoms (different shapes) with the same single tissue material are also implemented, which are shown in Figure 3.1. The size of the head model/phantom is 182 mm×187mm×230 mm. The implantable electrode arrays are normally implanted inside the cortex and the processing chip is between the dura and the grey matter (65). Therefore, the dielectric properties of these two single-tissue head phantoms are calculated from the average of properties of the dura and the grey matter (88) (relative permittivity of 46 and conductivity of $\sigma=1.6$ S/m).

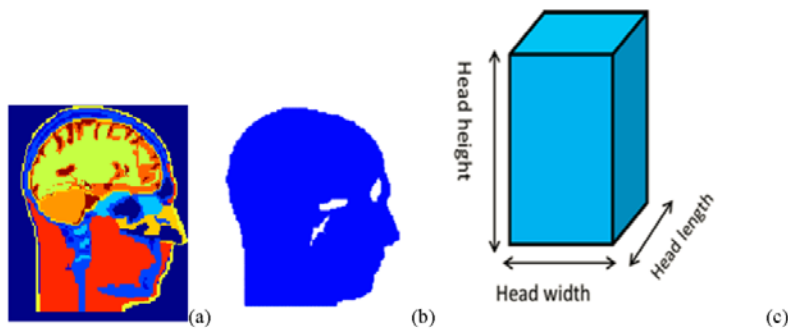


Figure 3.1: Three different human model phantoms used for antenna performance analysis. a) Sagittal cross sections of the multi-tissue head model at the middle slice; b) Sagittal cross section of the homogenous head-shaped phantom model at the middle slice; c) Homogeneous rectangular shape phantom model.

3.2.4 Antenna Measurement Set-up

In this work, the accuracy of the FDTD simulation package results is also verified by antenna measurement results. The test setup consisted of a vector network analyzer (Agilent, 300 kHz -3 GHz) incorporating an SMA connector to attach the antenna. This connector is calibrated into the connected coaxial cable, in order to account for the connector's effect (phases and impedances) on the measurements. A 5 cm monopole antenna is built up by a copper rod (diameter is about 2.6 mm) and measured in the RF lab to characterize the antenna performance, in terms of its input impedance and resonance frequencies. The measurement set-up is shown in Figure 3.2.

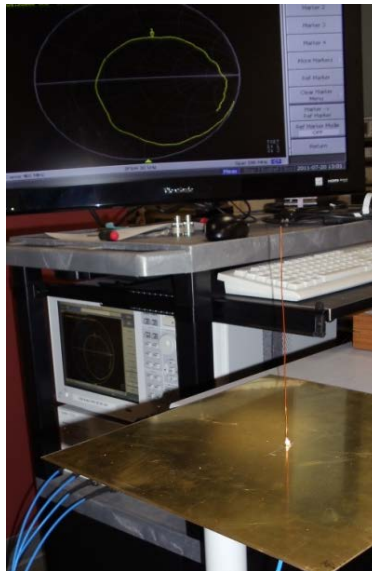


Figure 3.2: Monopole antenna measurement set up

3.3 RESULTS

3.3.1 Measurement Validation of the FDTD Simulations

The operation of a 10 cm dipole antenna including its excitation using transmission line feeding is simulated in order to compare with the measurements of a monopole antenna (60). The simulation results of the dipole antenna in free space/air are divided by a factor of two in order to compare with the monopole antenna measurement results (60,89). Comparison of the antenna's input impedance obtained using simulations and experimental measurements are shown in Figure 3.3. The excellent agreement between the simulation results and the measurement results from 0.5 GHz to 3 GHz verifies the accuracy of the simulation including the FDTD method as well as the implemented virtual transmission line feed model. The FDTD package was also verified by analytical analysis inside lossy materials (49).

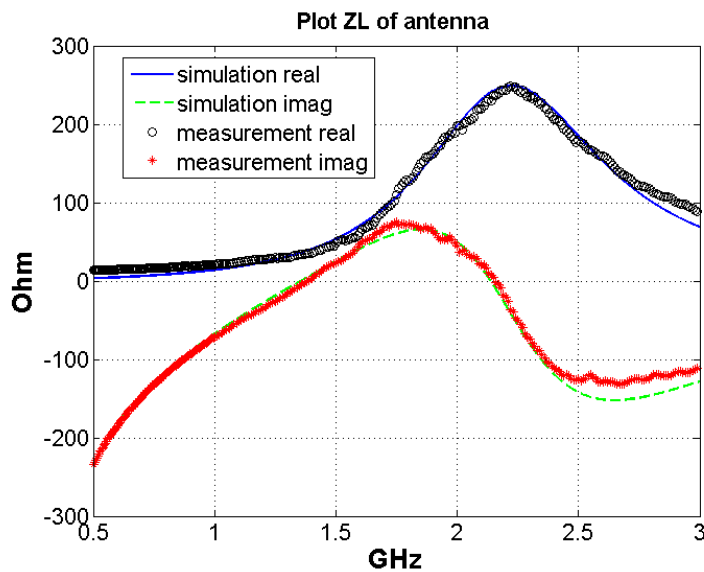


Figure 3.3: A comparison of the FDTD simulation results with the measurements for the input impedance of the monopole antenna

3.3.2 Effects of Ultra-thin Insulating Layers

Biocompatible insulating materials are used to surround implanted antennas in order to prevent metallic oxidation and avoid the short circuit effect from high conductive human head tissues. These biocompatible insulating layers could even the electromagnetic wave transition between the source and the head model and reduce the coupling with the lossy human tissues (73). From the antenna miniaturization techniques aspect, the dielectric loading (biocompatible insulating material) has also been shown to be a very effective way of reducing the dimensions of the antenna (34). Furthermore, the tissue model in the area immediately surrounding the implant affects the antenna performance considerably (71). In this work, the impacts from the micrometer scale insulating layers are studied.

A physical description of the rectangular antenna with a length of 13 mm and width of 3 mm (the thickness and width of the wire of this implanted antenna is negligible) surrounded by the insulating layer is shown in Figure 3.4(a). In the Figure 3.4(a), the dark rectangular line is the antenna wire and the grey part is the biocompatible insulating material mesh. The excitation is located at one of the longer parallel wires. The antenna surrounded by the insulating layer is numerically implanted into the center of the brain of the 3D anatomically detailed human head model (Figure 3.4(b)).

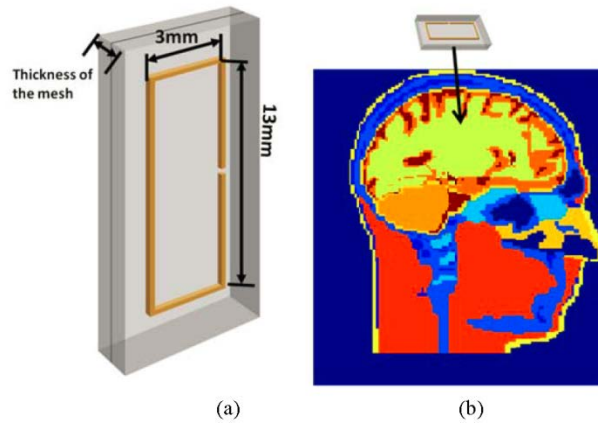


Figure 3.4: Geometry of the antenna and head model a) Implanted rectangular antenna; b) Antenna position inside the head model (sagittal view of the head model is shown), the color bar scale represents the relative permittivity values

The simulation's spatial resolution is set to 1mm in this study. The thicknesses of the insulating layers are changing from 25 μm to 330 μm (thin material sheets are modeled using the three dimensional sub-cell modeling formula in FDTD (84)). Since the biocompatible materials are usually polymers and ceramics, which are low conductivity materials, the relative permittivity of the insulating layers is simulated as 2.1 (polycarbonate) in this simulation and the conductivity is approximately zero (90,91).

The results in Figure 3.5 demonstrate that the thickness of insulating layers significantly impacts the antenna's resonance frequency and input impedance, which in turn will affect the antenna's radiation efficiency. The results could be explained: when an antenna is implanted inside the human head model, the dielectric constant of insulating layers (2.1 in this case), is much smaller than that of the head tissues. The velocity of the electromagnetic wave is higher in the small dielectric constant material thus yielding longer operating wavelength. Therefore the resonant frequency with the same length antenna will shift to higher frequency when compared

to non-insulating cases. This effect increases when the insulating layer becomes thicker (from 25 μm to 330 μm). The real part of the input impedance also increases because of the decreased average dielectric constant of the whole surrounding volume of the implanted antenna, including the insulating material and the brain tissues. In other words, the lossy human tissue material is moved away from the near field of the implanted antenna with a micrometer insulating layer which will lead to higher radiation efficiency. For example, with the 330 μm insulating-layer antenna the real part of the input impedance (which is 420 Ohm) more than doubles that obtained with the 25 μm insulating-layer antenna (which is 180 Ohm) as shown in Figure 3.5.

From the simulation results plot of the frequency and input impedance in Figure 3.5, the input impedance values don't change dramatically for insulating layers with different thickness if the operating frequency is larger than the resonant frequency (1.7 GHz -4 GHz). Therefore, for this implanted antenna, if the operational frequency is chosen in this frequency band, the mismatch from the thicknesses changing will be minimal.

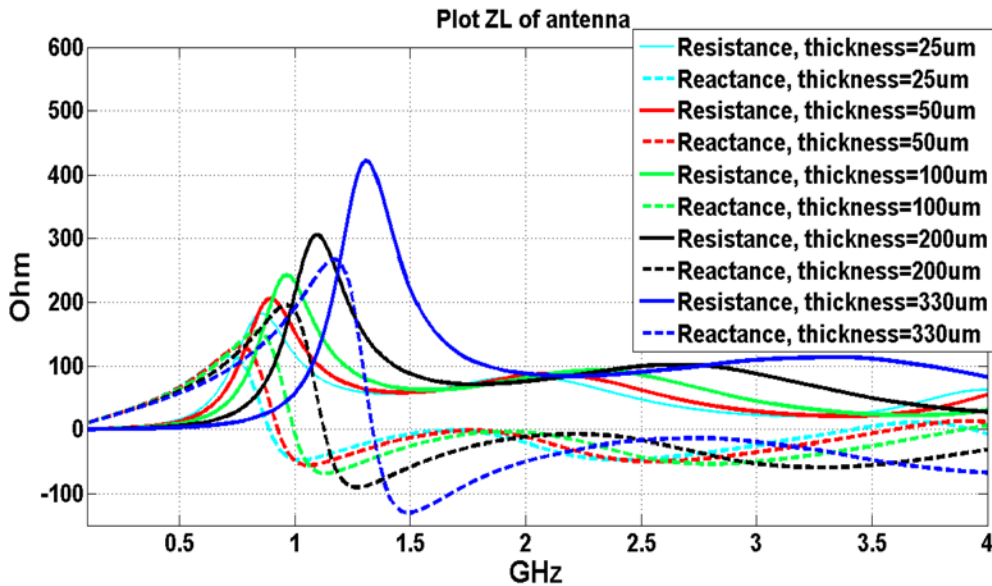


Figure 3.5: Effects of thin insulating layers on the input impedance of the implanted antenna inside the head model

3.3.3 Effects of the Insulating Layer Dielectric Properties

The same geometry of the rectangular implanted antenna shown in Figure 3.4(a) is simulated with two different biocompatible insulating layers (the simulated insulating layers have the same thickness of 0.33 mm in the two simulations) inside the human head model. The simulation results are shown in Figure 3.6.

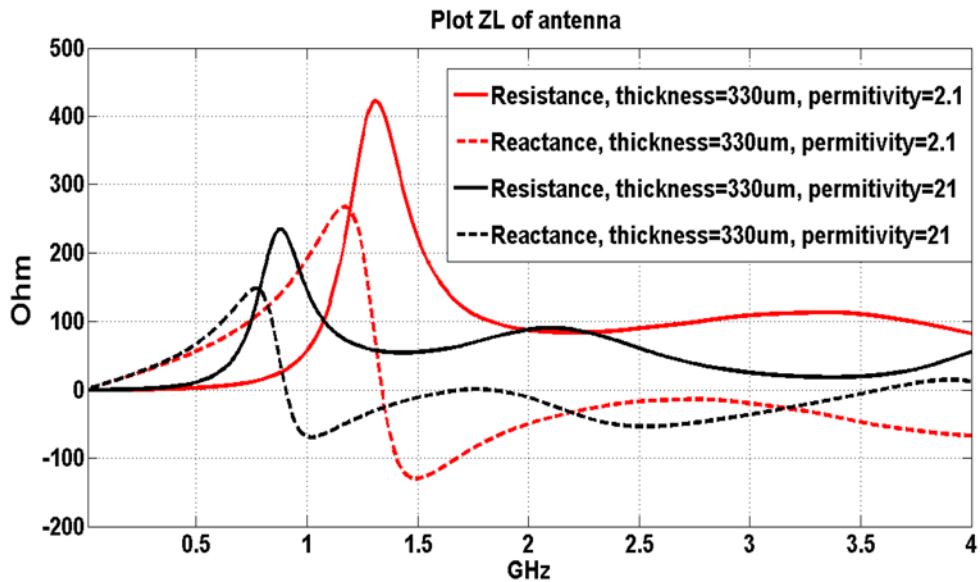


Figure 3.6: Simulation results of antennas surrounded with insulating layers with the same thickness but the different dielectric properties

The simulation results in this section show not only that the thickness of the insulating material affects antenna performance, but also the dielectric property of the insulating materials influence the performance of the implanted antenna inside the human brain. The results reveal that the antenna resonant frequency shifts to a lower frequency when the antenna is embedded inside a high dielectric constant insulating layer. Figure 3.6 also shows that the first resonant frequency is around 1.4 GHz if the relative permittivity is 2.1. If the antenna is embedded in the

material with relative permittivity of 21, the center resonant frequency will be around 0.9 GHz. Higher averaged dielectric constant of the media surrounding the antenna reduces the wavelength of the electromagnetic waves inside the media. As the length of the antenna depends on the wavelength of the antenna's operational frequency, high dielectric constant insulating layer consequently facilitates the reduction of the antenna's geometric dimensions. However, a high dielectric constant insulating layer may reduce the real part of the input impedance of the antenna, which in turn may hamper the radiation efficiency. Therefore, a balance design of high radiation efficiency and smaller dimensions is crucial to achieve optimal performance.

3.3.4 Effects of the Head Tissues Properties

The performance of the implanted antenna is influenced by all surrounding materials, which include the biocompatible insulating layers and the lossy human head tissues. In this section, the same rectangular antenna is simulated at three different locations inside the human brain model. For clinical usage, the BCI devices are normally implanted between the dura and the grey matter (65). Hence, the three different locations are all proposed around the dura, which is responsible for keeping in the cerebrospinal fluid. In Figure 3.7, the dura is represented by the light orange color around the brain cortex. Above the dura is the cortical bone and below the dura are the combination tissues of the dura and grey matter in the head model. Their constitutive properties and the simulated antenna positions in this head model are listed in Table 3.1. The same insulating layer (thickness of 1 mm and relative permittivity of 2.1) is used for three different simulation cases.

Table 3.1. Dielectric property of three adjacent major tissues at three different locations inside the human head (Figure 3.8) at 2.4GHz

Tissue and distance from the surface	Conductivity[S/m]	Relative permittivity
Bone Cortical, 1.6 cm	0.385	11.41
Dura , 1.9 cm	1.639	42.099
Brain Grey Matter, 2.24 cm	1.773	48.994

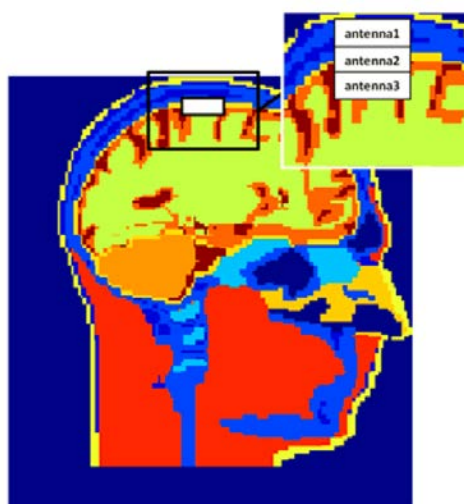


Figure 3.7: Implanted antenna at three different locations inside the human head model

Table 3.1 shows that at 2.4 GHz the conductivity and relative permittivity of grey matter (1.773 S/m and 48.994 respectively) are similar to the dura's dielectric property (1.639 S/m and 42.099 respectively) and different from that of the bone (0.385 S/m and 11.4) (88). These similarities and differences hold true for all other frequencies of interest. Figure 3.8 displays input impedance of the implanted antenna at the three different implanted positions inside the human brain shown in Figure 3.7.

Since these three implantation positions are adjacent to each other, we assume that any performance difference of the antenna is not caused by the implantation depth. The results show that the implanted antenna performs differently in bone and in the dura while the same antenna performs relative similar when the antenna is implanted in the dura and directly under the dura. In addition, the brain tissues are separated from the implanted antenna by the biocompatible insulating layers. The frequency shifts and the impedance variations caused by the changes in the tissues properties changes are not as significant as the biocompatible insulating layers' impacts.

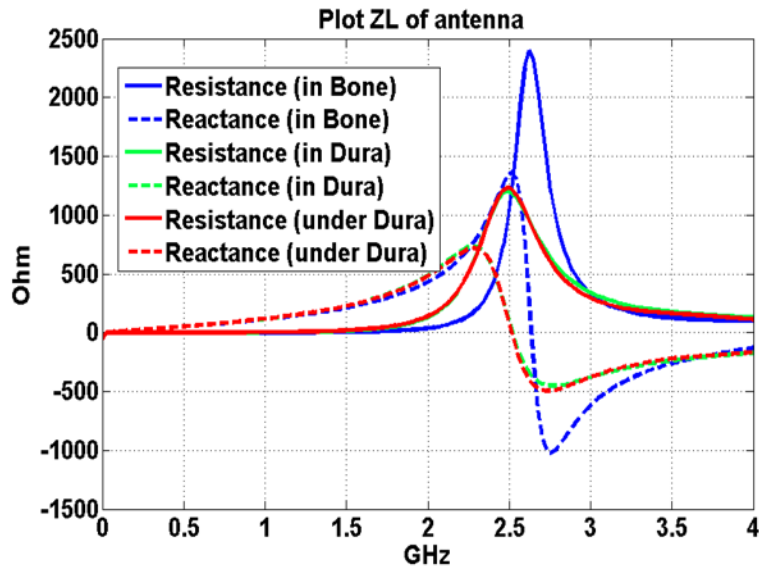


Figure 3.8: Input Impedance of the implanted rectangular antenna at three different locations inside the human head (Figure 3.7)

The input impedance of the antenna implanted above the dura, where cortical bone is present, is larger than the other two cases. Therefore, the antenna implanted in low conductivity tissues (e.g. cortical bone) may facilitate the antenna radiation efficiency. In addition, the antenna frequency could be altered with time caused by saline absorption (75) resulting in instability in the antenna performance. The brain tissues, with properties that are stable over

time and have less saline content (i.e. the cortical bones), may be preferable for antenna implantations from the considerations of antenna transmission efficiency as well as RF circuit stabilization. This of course will impact the design and dimensions of the micro wires and applicability of the BCI.

3.3.5 Effects of the Human Head Phantom Shape and Dielectric Properties

A head shaped phantom with single liquid mixture was experimentally used by other groups to test the human head's effects on the implanted antenna. For example, in (92) the return loss and transmission parameters were measured using a head shape phantom by Schmidt & Partner Engineering for the dosimetric assessment system. To answer whether a multi-tissue head phantom is necessary for measuring the implanted antenna performance accurately, and whether a head shaped phantom with one homogeneous material could be used to test implanted antenna performance (frequency bandwidth and input impedance), the antenna performance is studied inside three different 3D phantom models. We utilized a multi-tissue head model, a homogenous head model, and a rectangular phantom model, all of which have the same head height, length, and width (see Figure 3.1.) As mentioned, the relative permittivity is $\epsilon=46$ and conductivity is $\sigma=1.6$ S/m for the rectangular phantom model and the homogenous head model.

The 3mm by 12mm rectangular antenna with 1mm insulating layer is implanted 19 mm under the top of the multi-tissue head model (Figure 3.1(a)) (the spatial resolution of the simulation is 1mm), which is just under the dura of this head model. It is centered at the coronal and axial directions. The same insulated rectangular antenna is implanted at the exactly same physical positions inside the homogenous head shape phantom and the rectangular shape phantom model respectively.

The simulation results are presented in Figure 3.9 and demonstrate that the performances of the implanted antenna are highly similar inside the three head/phantom models, although the shapes of the head phantoms are different. Especially, the results are identical when the antenna is implanted inside the homo-head model and when it is inside the homo-phantom model. This verifies that the phantom model shape is not necessary to assess the implanted antenna's performances (input impedance and resonance frequency) for this application. A rectangular homogenous phantom could be used instead of a more complex head-shaped phantom to assess the BCI implanted antenna's specific characteristics (frequency band and input impedance).

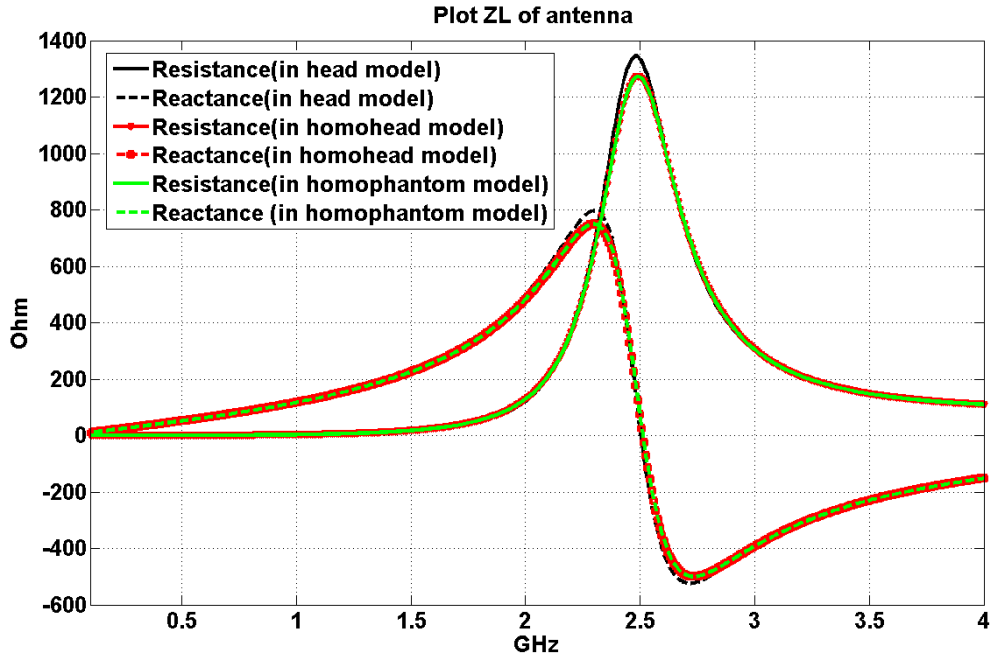


Figure 3.9: Input Impedance of the antenna when implanted 19 mm inside the multi-tissue head model, the head shaped homogenous phantom model and the rectangular homogenous phantom model

While an homogenous rectangular head-sized phantom could be used to study the implanted antenna's bandwidth and input impedance, the head shape as well as the presence of different types of tissues is necessary to study heating/SAR/power transmission. This is because

SAR as well as the power will change when RF waves go through different tissues, therefore the rectangular homogenous phantom may not be accurate to advise such information.

3.3.6 Designs of the Implanted Antennas

Around 2.4 GHz, a minimum wavelength (15mm) shows up in high water content material—the Cerebra Spinal Fluid (CSF) in human head tissues. Results of the one-cell-gap-feeding models show convergence to the true value if using fine grids (60,93), so spatial resolution of 0.165 mm ($\lambda_{\min} / \Delta x = 90$) is implemented for the following miniaturized antenna designs. The time resolution of FDTD is calculated based on the stability conditions to satisfy the stability criterion.

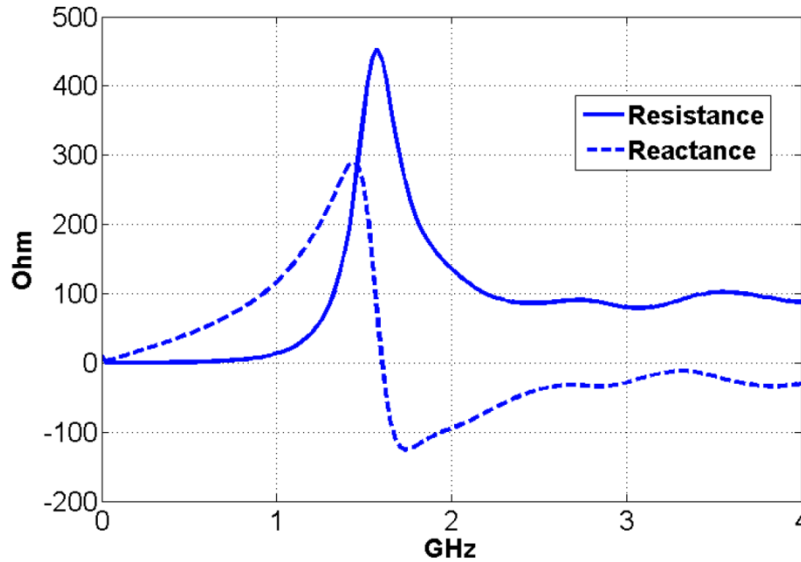
Three implanted antenna designs are simulated and compared in this study. The same insulating material is used for these implanted antenna simulations (the thickness is 0.33mm). The thickness of 0.33 mm is chosen because it is a feasible thickness to manufacture and assemble. The surrounding biocompatible material is peek (73) polymer (the relative permittivity is 3.2), which has excellent mechanical properties (stiffness, toughness and durability).

The first antenna design considered is a rectangular antenna. The detailed geometry is shown in Figure 3.10(a). Its input impedance as a function of frequency was calculated using the FDTD model and is shown in Figure 3.10(b). The first resonant frequency (when the imaginary part of the input impedance is zero) is around 1.6 GHz. In order to reduce the circuit mismatching effect, the frequency bandwidth could be chosen between 2 GHz and 4 GHz (because the impedance of the antenna is relative stable in this frequency band).



(a)

Plot ZL of antenna

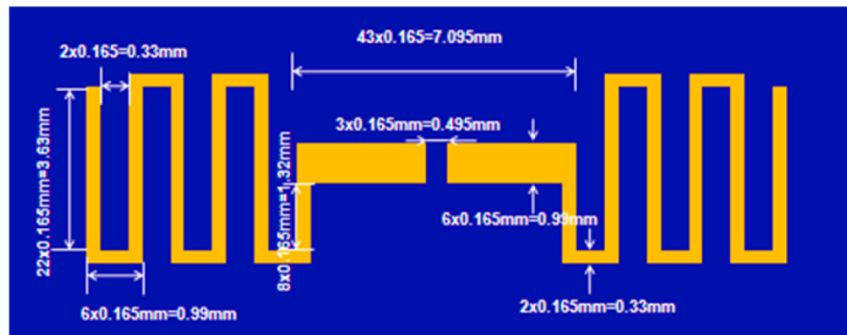


(b)

Figure 3.10: Geometry (a) and input impedance of the implanted rectangular antenna (b)

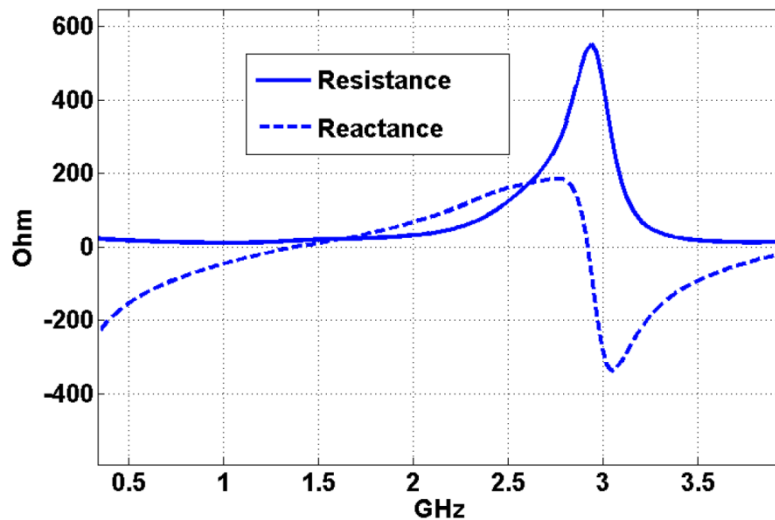
The second implanted antenna design considered is a serpentine antenna or a meander line antenna (94) which substantially has the greater length in a specific surface area. The geometry detail of the implanted serpentine antenna is shown in Figure 3.11(a). The size of the implanted serpentine antenna (length of 13.695 mm and width of 3.96 mm) is almost the same as the length of the implanted rectangular antenna (length of 13.695 mm and width of 4.29 mm), but has a much longer physical wire length (55.935 mm for the serpentine antenna and 31.35 mm for the rectangular antenna). From the simulation results of the input impedance and frequency in Figure 3.11(b), the first resonant frequency is around 1.38 GHz, which is 220 MHz lower than the

first resonant frequency of the implanted rectangular antenna. The frequency bandwidth could be chosen between 1 GHz and 2 GHz (the impedance of the antenna is relative stable in this frequency band). The real part of the input impedance of the serpentine antenna is almost one fifth of that associated with the rectangular antenna at their respective bandwidths (stable resistance slope as a function of frequency); 18 Ohm around 1.5GHz for the serpentine antenna and 100 Ohm around 2.4 GHz for the rectangular antenna.



(a)

Plot ZL of antenna



(b)

Figure 3.11: Geometry (a) and input impedance of the implanted serpentine antenna (b)

The third implanted antenna design considered is a dipole antenna. The geometry detail of the implanted dipole antenna is shown in Figure 3.12. The first resonant frequency is around

5.2GHz, which shows that the dipole antenna is electrically shorter than the other two antennas. Since the 5.2 GHz falls out of our accurate simulated range (1 GHz to 4 GHz), the impedance and frequency plot is not shown here. The real part of the input impedance around 2 GHz is around 14 Ohm.

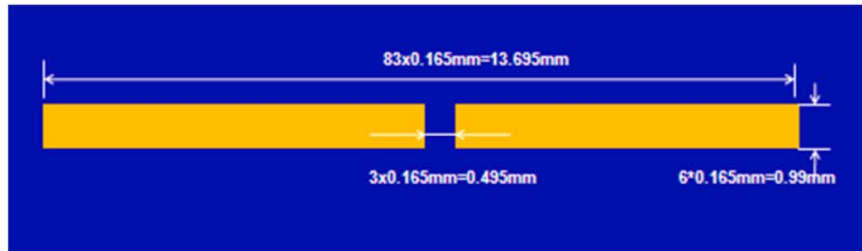


Figure 3.12: Geometry of a dipole antenna

3.3.7 Maximum Power Reception without SAR Violations

The SAR safety regulations regarding RF power deposition in the head varies for different applications. In this work, the power receptions of the implanted antennas are analyzed based on the IEEE RF safety Standard developed by the International Committee on Electromagnetic Safety (ICES) IEEE 2005 (95) and the International Commission on Non-ionizing Radiation Protection (ICNIRP) safety regulations (96) with respect to human exposure to radiofrequency electromagnetic fields up to 300 GHz. With respect to SAR limits, the frequency is from 100 kHz to 3 GHz in IEEE regulation and 100 kHz–10 GHz in ICNIRP regulation. According to these two SAR regulations, the local SAR peak averaged over any 10g of tissue in the head must be less than or equal to 2 W/kg.

In order to calculate the maximum power reception under the SAR limitations, a dipole antenna is chosen as the external transmitting antenna and the three different implanted antennas

are simulated as the receiving antennas. Based on the analysis of these three designed antennas (especially the rectangular antenna and the serpentine antenna), the common preferred frequency band is around 2GHz. Therefore, the length of the external antenna is defined as 75 mm (with negligible thickness). Its resonant frequency is around 2GHz (simulated and analyzed when the head model existing in the environment near the antenna). The distance between the transmit and receive antennas is about 30 mm; the inner antenna is just under the dura and the outside antenna is about 10mm away from the surface of the head. Their excitation positions of transmit and receive antennas are vertically centered and placed at the same plane. The multi-tissue head model is used to study the maximum received power from the implanted receiving antenna without violating the SAR limits.

Considering the implanted rectangular/serpentine/dipole antennas' input impedance characteristics, the simulated load of implanted chip and circuits (virtual transmission line connected to the antenna ports) are modified to match with the real part of input impedance of the implanted receiving antenna at frequency 2.0GHz. Considering there are also reactive parts, it is not a perfect match. Hence the calculated (in this work) maximum available power will represent a less optimized scenario: while the real part of impedance is identical for both the implanted receiving antenna and the chip circuitry/transmission lines, no matching circuit is utilized to compensate for the mismatch in the imaginary part. The calculated maximum power received by the three antenna designs at the SAR limit is shown in the Table 3.2. The results could be changed from the calculated results in this work (more power can be received potentially) once the source is matched to the load perfectly.

Table 3.2 shows the serpentine antenna allows for more power reception at the SAR limit than the rectangular antenna: the maximum received power is 1.8 mW at the SAR limit when the

serpentine antenna is implanted around the dura. While the results show the superiority of the serpentine antenna in terms of power reception, the higher input impedance of the rectangular antenna allows for better interfacing with the typically expected high input impedance of the chip circuitry (less impedance mismatch).

Table 3.2. Maximum power reception under IEEE and ICNIRP SAR limit (2 Watts perKg per 10gm) at 2 GHz when the implanted antenna is placed right under the dura

Antenna	Maximum power reception (mW)
Rectangular antenna	1.3
Serpentine antenna	1.8
Dipole antenna	0.578

Furthermore, the maximum power reception has also been investigated when the rectangular antenna was implanted inside the cortical bone. The calculated result shows that the rectangular antenna implanted at the bone could receive about 2.5 times more RF power at the SAR limit than that obtained when the antenna is implanted at the dura.

3.4 CONCLUSION

Miniaturized antenna designs for the BCI application were simulated and analyzed in this work. The simulation results show that the micrometer thickness insulating layer can significantly impact implanted antenna performance. The proper selection of the dielectric properties of the

biocompatible insulating layers and the implantation position inside head brain tissues would facilitate the RF power transmission/reception. The shape of the head model may not be a critical factor, but the dielectric properties of surrounding tissues can impact the implanted antennas' input impedance and its operational frequency bandwidth.

Based on three miniaturized antenna designs' simulation results, maximum power of 1.8 mW could be received by an implanted serpentine antenna when it is implanted inside the dura at the IEEE and ICNIRP SAR limit. Assuming a 25% RF/DC conversion efficiency (due to the switching nature of the harvester circuits), the implantable BCI device can consume 450 uW or less based on the results in this work. Our current designs of simple implantable chip consume about 35 uW (97) which means the designed miniaturized antenna could provide sufficient power to this available chip design if placed in the dura.

4.0 IN-DEPTH ANALYSIS OF THE ELECTROMAGNETIC PSEUDO MODES PRODUCED BY A 20 CHANNEL TIC-TAC-TOE TRANSMIT ARRAY

4.1 INTRODUCTION

Ultrahigh-field ($\geq 7\text{T}$) MRI can be exploited for many different medical research purposes and applications through higher resolution anatomical imaging, better localization imaging and improved spectroscopic imaging. However, there are technical and physical limitations associated with ultrahigh-field imaging that have not yet been fully combated: a) the inhomogeneous distribution of the transmit fields B_1^+ (9-12), b) potential high power deposition inside the human tissues (13,14) and the difficulty to supervise the local specific absorption rate (SAR) (15), c) the accuracy of B_1^+ field mapping methods challenged by the large dynamic range of the transmit fields (98), etc.

Innovative RF coil designs have been proposed in order to optimize the RF (SAR and B_1^+ field) performance of ultrahigh field MRI (99-101). Among many techniques, the eigenmode approach has been applied to solve various electromagnetic problems. 2D image uniformity of a spherical phantom was improved by linearly combining 8 harmonic modes where the addition of higher-order harmonics was shown to significantly affect the RF uniformity (102). Eigenmode approaches have also been utilized to analyze the signal to noise ratio (SNR) behavior of phased array receive coils (103,104). The higher-order resonant modes were also used to facilitate

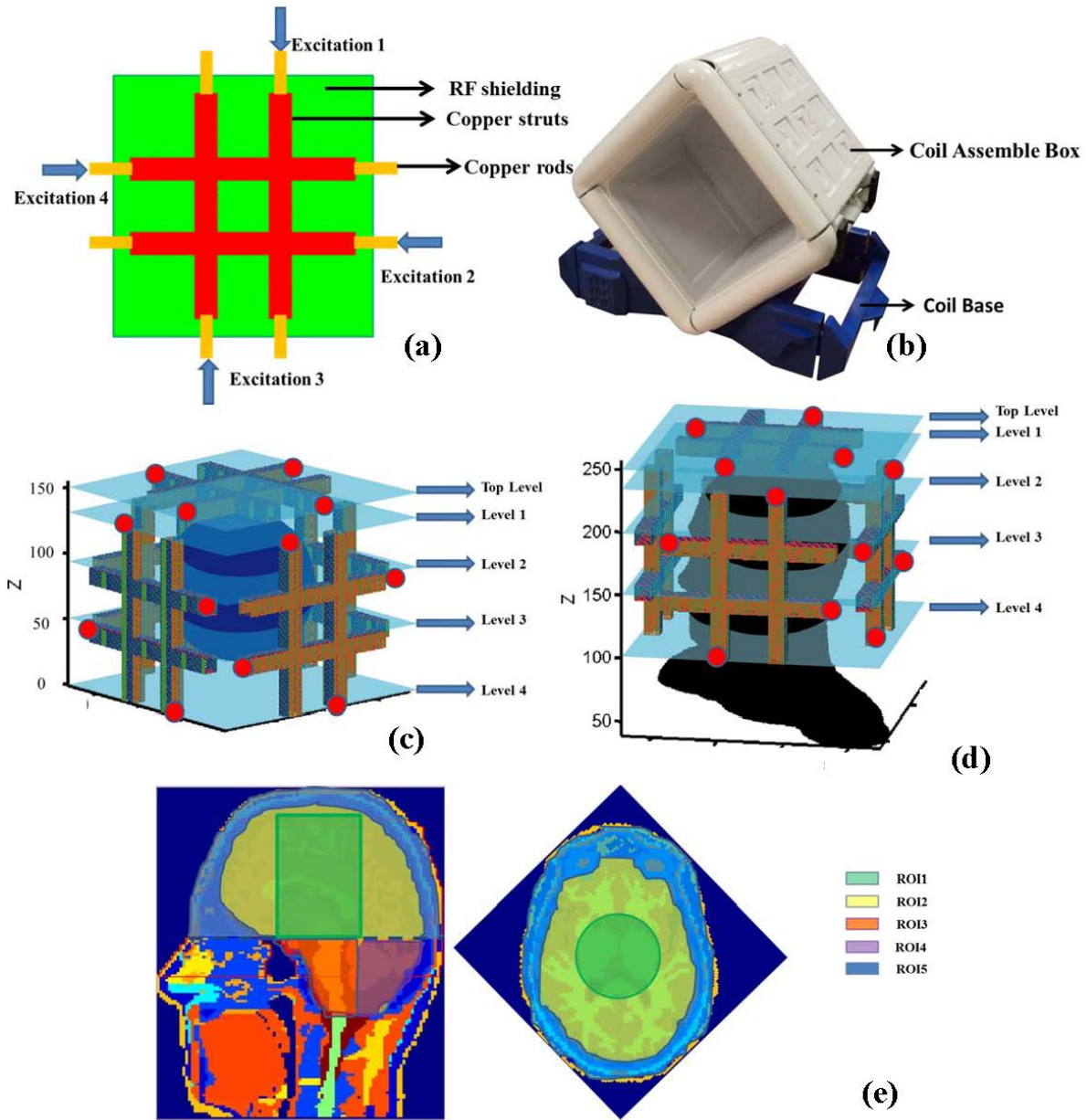
parallel imaging performance in order to improve g-factor or to increase acceleration factor (105).

In this work, an excitation paradigm is presented utilizing a new 20-channel, 5-sided Tic-Tac-Toe based RF transmit array design for 7T MRI (100). The coil performance was studied using the eigenmode approach. Eigenmodes were numerically calculated from the simulated magnetic fields by using finite difference time domain (FDTD) method, and experimentally compared using a 7T human MRI scanner. The design of the transmit array renders 20 transmit elements that are positioned into 5 different Z (direction along the magnet axis) levels, where each level is composed of 4 transmit elements that are positioned at shifted locations in the XY plane; i.e. the XY positions of the transmit elements differ at each level. For each of the 5 levels, there are 4 different distinctive modes that can be generated (named as Quadrature, Opposite-phase, Anti-quadrature and Zero-phase modes in this work); hence there are 20 distinct modes that can be excited in total. While the array is inherently coupled by design, the computed fields were calculated as well as experimentally demonstrated when all the channels are taken into consideration. As a result, five of these modes (one from each level) can be exactly and simultaneously excited with power splitters (the splitter number could be arranged based on how many parallel transmission lines are available in the MRI system). The eigenmodes performance is successfully tested on a 7T MRI scanner by scanning a phantom and *in-vivo* with 7 human subjects. These modes are consistent between different human subjects.

4.2 MATERIAL AND METHODS

4.2.1 The RF Coil

In this work, a 20-channel head transmit array was studied. Figure 4.1 (a) shows the schematic diagram of a four-element, 2x2 Tic-Tac-Toe transmit array design (100,106,107). The red part is composed of 4 crossed hollow copper struts. The yellow parts, which represent the copper rods, are partially inside the copper struts. The copper struts and copper rods work together as four crossed coaxial transmission lines. Tuning and matching of the coil are done by changing the length of the copper rods inside the copper struts. The green part represents an RF copper shielding, which is placed at the back of the crossed transmission line structures. This RF copper shielding functions as the ground of a cavity resonator. The RF copper shielding is slotted with specific patterns to reduce eddy currents while the RF performance is maintained (108). The 4 excitations are also shown in Figure 4.1(a). Figure 4.1 (b) shows an assembled RF coil system composed of 5 sets/sides of the 2x2 Tic-Tac-Toe transmit array (total of 20 transmit elements). All the coil structures, including the coil base, coil assemble box, and coil struts base (not shown in the figure) were printed by a 3D printer and the coil system was tuned and tested using an Agilent Network Analyzer (Santa Clara, US). These 5 sets of coils are decoupled ($S_{12} \sim -20\text{dB}$). For each set/side (shown in Figure 4.1(a)), the coupling is higher: $S_{12} \sim -7\text{dB}$ (adjacent elements) and $S_{13} \sim -3\text{dB}$ (opposite elements.) Figure 4.1 (c and d) shows the relative position between the 20 transmit channels loaded with a water phantom model (c), and a human head model (d). The excitation locations are also indicated by the red dots.



$$(ROI6= ROI1+ROI2; ROI7=ROI3+ROI4; ROI8=ROI1+ROI2+ROI5)$$

Figure 4.1: Coil schematic diagrams and load positons.

(a) Schematic diagrams of a four-element, 2x2 Tic-Tac-Toe transmit/receive array design. The copper rods are partially inside the copper struts. They function as four crossed coaxial transmission lines. (b) An assembled RF coil system, composed of 5 sets of the 2x2 Tic-Tac-Toe transmit array (total of 20 transmit elements). (c) The resolution is 1/16 inch. Spherical water phantom (108 by 108 by 108 FDTD Yee cells). The red dots indicate the excitation points of three sets of the 2x2 Tic-Tac-Toe transmit/receive arrays; other

excitations are at the back of this 3D plot. (d) Human head model (114 by 117 by 144 FDTD Yee cells). (e) The head model was divided into 8 different regions of interest (ROIs) for this study. Central Main Brain (ROI1) is indicated by green and it is a cylinder (Seen from the sagittal view, it is a rectangular box and seen from the axial slice, it is a circle and the radian is 25 mm). ROI2 Peripheral Main Brain (yellow region) is the brain outside of the ROI1. The Brain Stem ROI3 is indicated by light red. The Cerebellum ROI4 is purple. ROI5 including the skin, skull, eyes and CFS is indicated by blue.

The B_1^+ field is then analyzed inside 8 regions of interest. They are shown in Figure 4.1(e). Based on human head characteristics as well as the electromagnetic characteristics of the transmit array, we divided the regions of interest into the following:

- 1) Central Main Brain = ROI1,
- 2) Peripheral Main Brain = ROI2,
- 3) Brain Stem = ROI3,
- 4) Cerebellum = ROI4,
- 5) Surrounding the Main brain (skin + bone + eyes + CSF) = ROI5,
- 6) Main Brain = ROI6 = ROI1+ROI2,
- 7) Lower Brain = ROI7 = ROI3+ROI4,
- 8) Upper Head = ROI8 = ROI5+ROI6= ROI1+ROI2+ROI5.

4.2.2 Determination of Eigenmodes

Mathematically, the direct sum of the eigenspaces is equal to the whole space; the superposition of eigenfunctions can be used to represent arbitrary function conditions (109). For MRI applications, current distributions can be controlled through manipulating the amplitude and phase between coil elements. A specific current distribution on the array elements determines an

eigenmode (110). Targeted field distributions can then be represented by the superposition of eigenmodes.

In this work, B_1^+ field distributions are arranged by:

$$C = \begin{pmatrix} B_{1(1)} & \dots & B_{L(1)} \\ \vdots & \ddots & \vdots \\ B_{1(n)} & \dots & B_{L(n)} \end{pmatrix} \quad (4-1)$$

$C = \begin{pmatrix} B_{1(1)} & \dots & B_{L(1)} \\ \vdots & \ddots & \vdots \\ B_{1(n)} & \dots & B_{L(n)} \end{pmatrix}$ where C is the B_1^+ field matrix which is generated by an array with L

transmit channels. There are n points/pixels inside the region of interest (ROI). C^*C shows the correlation between the array channels. The eigenmodes can be calculated by:

$$(C^*C)v = \lambda v \quad (4-2)$$

where v is a unitary matrix of eigenvectors; $\lambda = \begin{pmatrix} \lambda_1 & \dots & 0 \\ \vdots & \ddots & \vdots \\ 0 & \dots & \lambda_L \end{pmatrix}$ is a diagonal matrix of

eigenvalues. With solutions for (4-2), Cv will be the spatially pseudo independent fields or eigen channels/modes of this transmit coil; v gives the phase and amplitude between each coil channel; λ_i represents the field energy for eigenmode i .

4.2.3 Helmholtz Equation and Current Requirements

For source-free fields, Helmholtz equation (111) is:

$$\nabla^2 A + k^2 A = 0 \quad (4-3)$$

where A is the magnetic vector potential which is defined by the magnetic fields B : $B = \nabla \times A$. Thus if we can find A of a current distribution, B can be obtained from A by a differential (curl) operation (112); if B is a constant everywhere (homogeneous fields), curl of A should be a non-zero constant and A should be non-zero. ∇^2 is the Laplace operator, k is the wavenumber. If A is non-zero and k^2 is non-zero, $\nabla^2 A$ will also be non-zero value, which means the vector potential is a second-order changing factor.

In this work, along the static field B_0 direction (Z direction in Figure 4.1 (c) and (d)), the transmit array can be grouped as 5 different rows/levels of 4 elements: Top Level, Level1, Level2, Level3 and Level4. From each level, MRI useful field distributions can be generated. We identify the eigenmodes for each of the 5 levels. Based on the eigenmode (4-2), there are 4 different excitations/channels for each level. As a result, the current can be changed not only at the XY plane but also along the Z direction. The freedom to manipulate the current distribution of different coil elements can contribute to the generation of homogenous magnetic fields (113-115). However, coil arrays have typically shown the capability to control current distributions at the XY plane, while not very commonly in the Z direction. It is worth noting that there are some coil designs that can potentially generate Z plane current control. For example multi row/ring transmit arrays that allow parallel transmission approaches (116-118); a rotating RF coil approach has been studied (119,120); a spiral volume coil has been discussed (121) to improve the RF field homogeneity.

4.2.4 Simulations and Experiments

An in-house Finite-difference time-domain (FDTD) package with an accurate transmission-line feed mechanism is implemented to model the RF performance of the Tic-Tac-Toe transmit coil (122). The transmission-line feed model properly simulates the excitation/reception source and thus can provide more accurate quantitative values of a coil's input impedance, power input and coupling between coil elements. This simulation package has been previously utilized and verified (48,49,83,108,122,123). The magnetic fields are calculated with a spherical phantom model (diameter=17.1cm, conductivity=0.46 S/m and relative permittivity=79) and a human head model (18.1cm × 18.6cm × 22.9cm), which was rescaled from the virtual family Duke Model (124). They are both shown in Figure 4.1(c) and (d). Eigenmodes are calculated using simulated field distributions by (4-2) and readily realized with sets of amplitudes and phases through different array element combinations. Since the simulation package accurately accounts for coupling between the transmit array elements (successfully verified with network analyzer measurements), which is high between elements on each Tic-Tac-Toe side/set and low between elements on different sides, the calculated eigenmodes (B_1^+ distributions) are also successfully verified by experiments done with a similar-sized phantom and *in-vivo* human subjects on a Siemens 7T human scanner (Erlangen, Germany) equipped with 8 parallel transmission lines (PTX). *In-vivo* B_1^+ maps were acquired using saturated turbo FLASH methods (SatTFL) and 8 flip angles were acquired for each measurement.

4.3 RESULTS

4.3.1 Eigenmodes inside the Phantom and the Head Model

By applying (4-2), the calculated relative phases are shown in Table 4.1 for each level of the coil elements with each eigenmode. The relative phase between elements is uniformly distributed: being 90° for Mode1, 180° for Mode2, 270° for Mode3 and 0° or 360° for Mode4. There are small phase errors ($\leq 10^\circ$) between different levels, which may be generated by the aligning of the phantom or the human head model within the coil. The amplitude differences are also very small (between different elements) - within 14%. In our experiences, the phase will be the major factor that impacts the field distribution patterns for most cases.

Table 4.1: Relative Phases of the 5 Levels of the Coil for the Phantom

	Mode1 (Quadrature)	Mode2 (Opposite-phase)	Mode3 (Anti-quadrature)	Mode4 (Zero-phase)
Top Level	(0, 90.2, 180.4, 270.2)	(0, 179.0, -0.1, 180.9)	(0, -91.6, -181.1, -269.4)	(0, -0.4, -0.5, 0)
Level1	(0, 90.8, 181.8, 271.1)	(0, 179.6, -1.3, 179.1)	(0, -87.7, -172.9, -264.8)	(0, -2.3, -7.6, -5.0)
Level2	(0, 89.0, 176.4, 267.4)	(0, 175.1, 10, 173.3)	(0, -96.0, -186.5, -270.0)	(0, -2.3, 1.8, -3.5)
Level3	(0, 89.7, 179.5, 269.8)	(0, 178.6, -3.5, 178)	(0, -92.9, -183.0, -270.1)	(0, -1.8, 0, -1.7)
Level4	(0, 90.0, 180.8, 270.7)	(0, 179.8, -0.6, 179.6)	(0, -89.6, -179.5, -269.9)	(0, 0, 0.7, 0.5)

4.3.1.1 B_1^+ Field and SAR Comparison for Mode 1 at Different Levels

The B_1^+ field distribution of Mode 1 for all levels is displayed in Figure 4.2. Figure 4.2 (top section) shows that the Mode1 provides center brightness for both head and phantom and the brightest spots along the Z directions are at different locations for the different levels. For the phantom with Mode1 of the Top Level, the bright spot is toward the highest point of the top part of the phantom; for Level1 and Level4, the bright spot is at the lower half of the phantom; for Level2 and Level3, the bright spot is at the top half of the phantom, while the highest

excitations are lower than that of the Top Level. The same analysis is also applied on the human head model: Mode1 of Level1 and of Level4 excite lower regions than that with the Top level. The B_1^+ field intensities of Mode1 of Level2 and Level3 are lower than that of Level1 and Level4. The asymmetric shape (front and back) of the head changed the field distribution and the modes are not as independent as inside the homogeneous spherical phantom.

The B_1^+ field phase distribution maps are shown in the mid-section of Figure 4.2. The phase distributions of Mode1 are symmetrically centered and are slowly varying (note that $-2\pi = 2\pi$, i.e. the intense blue color equals the intense red color in the colorbar). Comparing the phantom and the human head model, the phase patterns are very similar.

The locations of the peak SAR per average B_1^+ are also comparable between the phantom and the head model (bottom section of Figure 4.2). Furthermore, the locations of the high B_1^+ intensities per average SAR won't always generate high local SAR: note that for Level4 locations with the brightest B_1^+ field intensity correspond to a minimum SAR at the same locations.

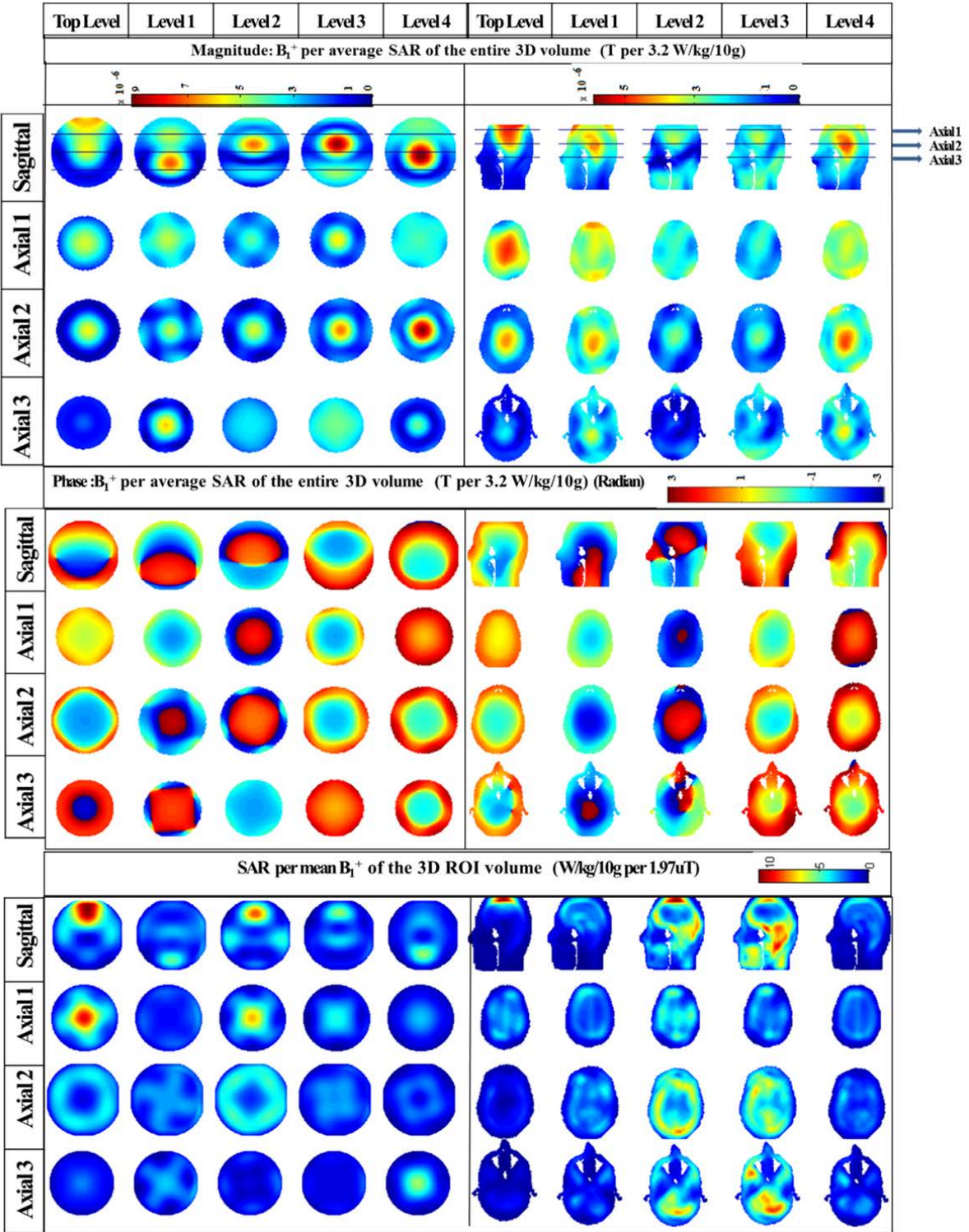


Figure 4.2: Central sagittal, and 3 axial slices of 1) B_1^+ field distributions (phase and intensity maps) per average SAR over the entire 3D volume that is equal to 3.2 W/kg/10g and 2) SAR distributions per average B_1^+ field intensity inside the ROIs (B_1^+ field intensity is normalized to 1.97uT).

For the phantom the 3D ROI is the entire 3D phantom, and for the human model it is the ROI8. The 3 axial slices were chosen together with the sagittal slices to show the 3D information. The three axial slices are equally distributed along the B0 direction inside the phantom. The three slices inside the human head model are at the exact same locations with respect to the coil elements as the three slices shown inside the phantom. Spherical water phantom: 108 by 108 by 108 FDTD Yee cells and Human head model: 114 by 117 by 144 FDTD Yee cells.

4.3.1.2 B_1^+ Field and SAR Comparison for Other Modes at Different Levels

Transmit field distributions for different modes at different levels are compared in Figure 4.3. The B_1^+ field distributions and intensities (per average SAR = 3.2 W/Kg) over the specified 8 ROIs for different modes and levels are shown in Figure 4.4. When comparing to other modes and with different intensities along the Z axis (depending on which level is utilized) the following observations are noted:

- a) Mode1 generally excites the Central Main Brain (ROI1) and Brain Stem (ROI3).
- b) Mode2 generally excites the Peripheral Main Brain (ROI2) and Cerebellum (ROI4).
- c) Mode4 generally excites the Cerebellum (ROI4), while the intensity is 15% less than that of Mode2 on an average;
- d) Inside the Main Brain (ROI6), average B_1^+ field intensities of Mode1 are 13% higher than that of Mode2 over all the coil levels while similar inside Upper Head (ROI8). Average B_1^+ field intensities of Mode3 are similar to Mode4's. Average B_1^+ field intensities of Mode1 and Mode2 are approximately twice of that with Mode3 and Mode4 inside Main Brain and Upper Head (ROI6 and ROI8).
- e) Inside Lower Brain (ROI7), average B_1^+ field intensities of Mode3 are similar to Mode1's and Mode2's.

f) Inside the Cerebellum (ROI4), average B_1^+ field intensities of Mode1 and Mode2 are higher than that of Mode3. Compared to other ROIs (intensities are generally less than $1 \times 10^{-6} T$ per 3.2 W/kg), average B_1^+ field intensities of Mode3 are most localized at ROI5 (intensities $\sim 2 \times 10^{-6} T$ per 3.2 W/kg).

g) For most ROIs, the average B_1^+ field intensities of Mode1 of Level2 and of Level3 are about a third less than that of Mode1 of Level1 and Level4.

h) For several ROIs, Mode3 and Mode4 have similar average B_1^+ field intensities. Nonetheless, the average B_1^+ field intensities of Mode4 are almost twice of that of Mode3 inside Brain Stem (ROI3) and Cerebellum (ROI4) and hence the Lower Brain (ROI7).

i) The maximum values of the average B_1^+ field intensities over Main Brain (ROI6) and Lower Brain (ROI7) per average SAR = 3.2 W/kg are $3.2 \times 10^{-6} T$ and $2.94 \times 10^{-6} T$ respectively.

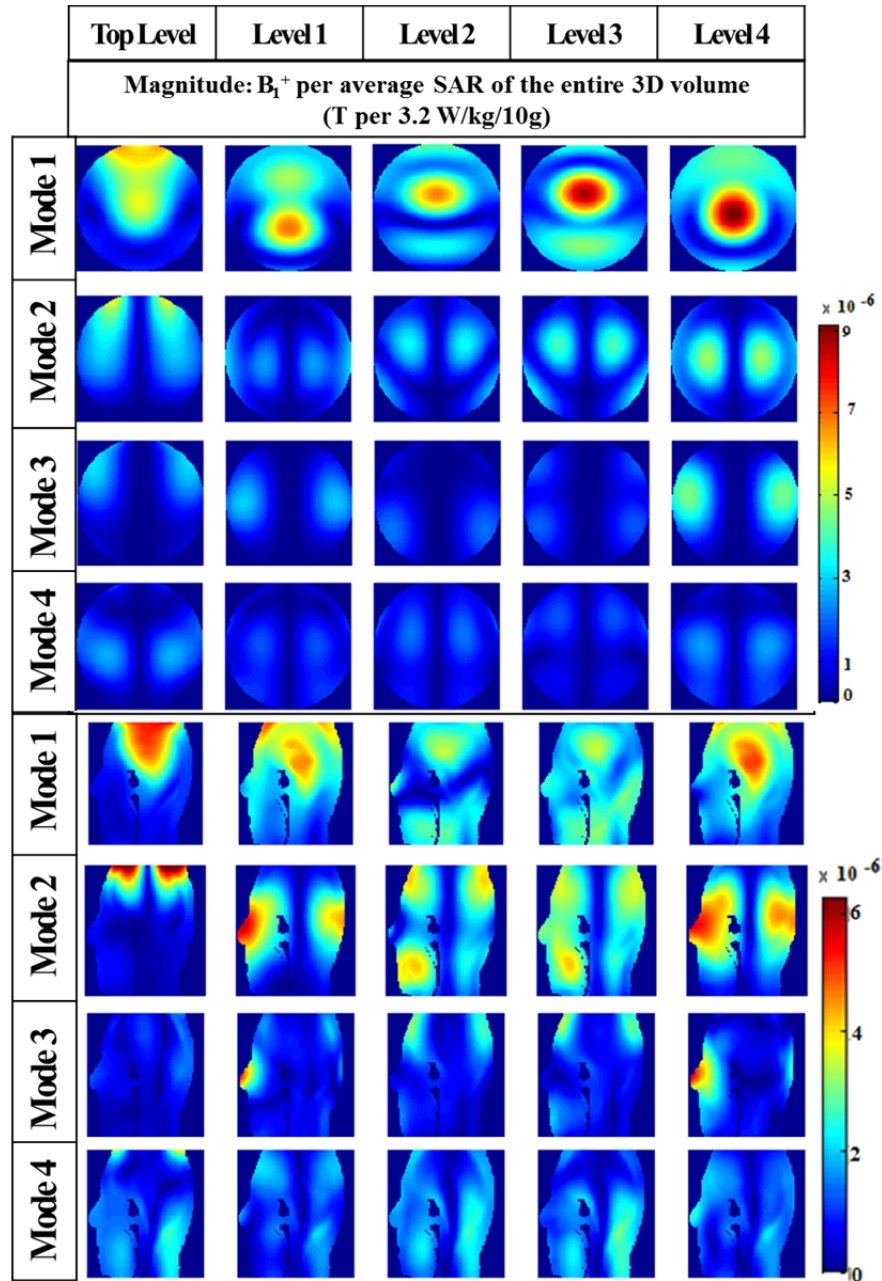


Figure 4.3: B_1^+ distributions for different modes. Center sagittal slices of B_1^+ field distributions per average SAR over the entire 3D volume (normalized to 3.2 W/kg/10g) are presented. Field patterns inside the phantom and human head model are comparable.

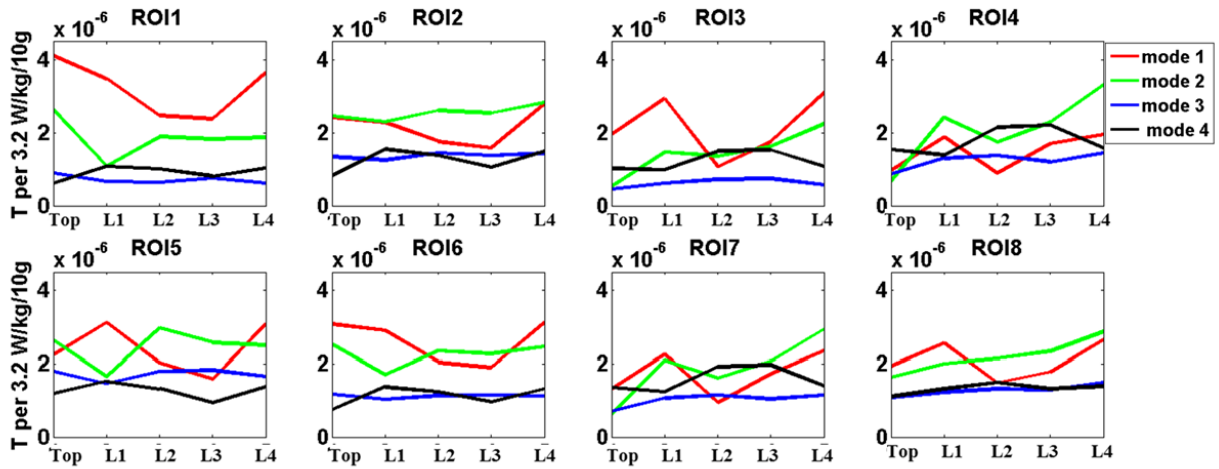


Figure 4.4: Average B_1^+ intensities calculated inside 8 different ROIs (shown in Figure 4.1.) The values of the average B_1^+ intensities are normalized to an average SAR over the entire 3D head volume. The unit is Tesla per 3.2 W/kg/10g.

4.3.1.3 Peak Local SAR

The peak local SAR is regulated by IEC/FDA safety regulations (<10 W/kg over any 10 gram of tissue). The ratios between peak local SARs and average SARs are normally considered (Figure 4.5). The following observations are also noted for peak local SARs:

a) The ratio is generally less than 6 for the human head model for the bulk of modes and levels.

b) The Top Level has higher peak over average SAR ratios when compared to the other levels. For example, the ratio for Mode1 of Top Level is 11.1. This can be explained by the SAR map in Figure 4-2. There is a hot spot inside the CSF just under the dura. If that mode on that level were to be utilized, such peak-to-average SAR can be reduced through a) RF shimming in combination with different levels and/or b) pushing the head down along the Z axis, in the current situation the top of the head is only 35 mm away from the copper of the top strut. It is noted however that the peak local SAR for Top Level Mode1 is about the same as that of Mode 1

of Level2 and Level3 while the average SAR is less which leads the peak to average ratio to be higher for Top Level Mode1.

c) For the human head, the best average SAR per average B_1^+ intensity is generated by Mode1 of Level4: the average SAR value inside ROI8 is 1.16 W/kg per 1.97uT. The preferable cases will be higher average B_1^+ intensity per average SAR and lower peak SAR per average B_1^+ intensity/SAR.

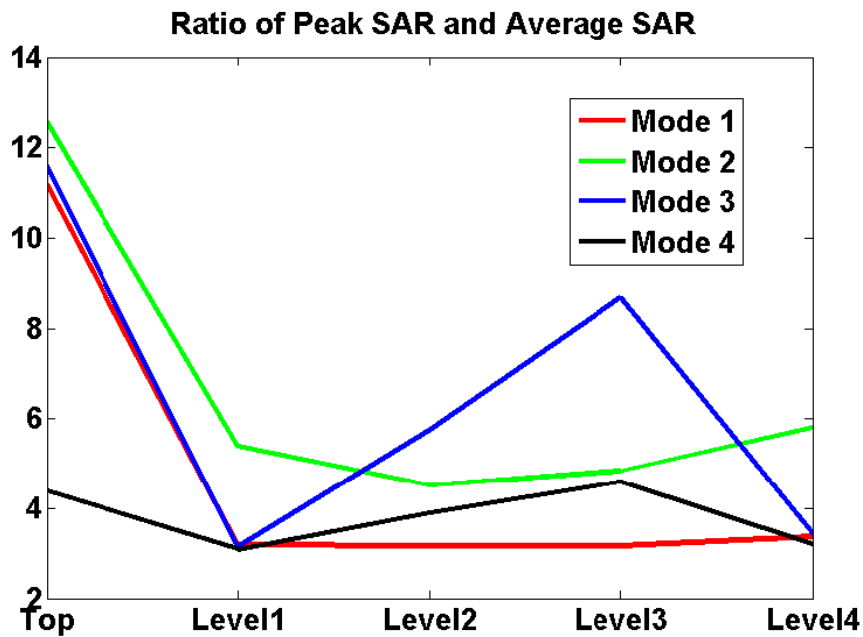


Figure 4.5: The ratio between the local peak SAR and average SAR over the entire 3D head volume for different levels and modes.

4.3.2 Experimental Demonstration

Modes inside the phantom and the head are compared with experimental measurements in Figure 4.6. Two sample B_1^+ field distribution maps (Top and Level1) within the water phantom are shown in central axial slices. Seven healthy human subject studies were conducted with signed consent forms approved by the Institutional Review Board at the University of Pittsburgh.

Three simulated B_1^+ field distribution maps inside the human head model are also shown in Figure 4.6 and compared with *in-vivo* B_1^+ maps in central sagittal slices. The comparisons are done for the *in-vivo* scans of all 7 human subjects. The 20-Channel Tic-Tac-Toe coil's modes are highly consistent with different human subjects.

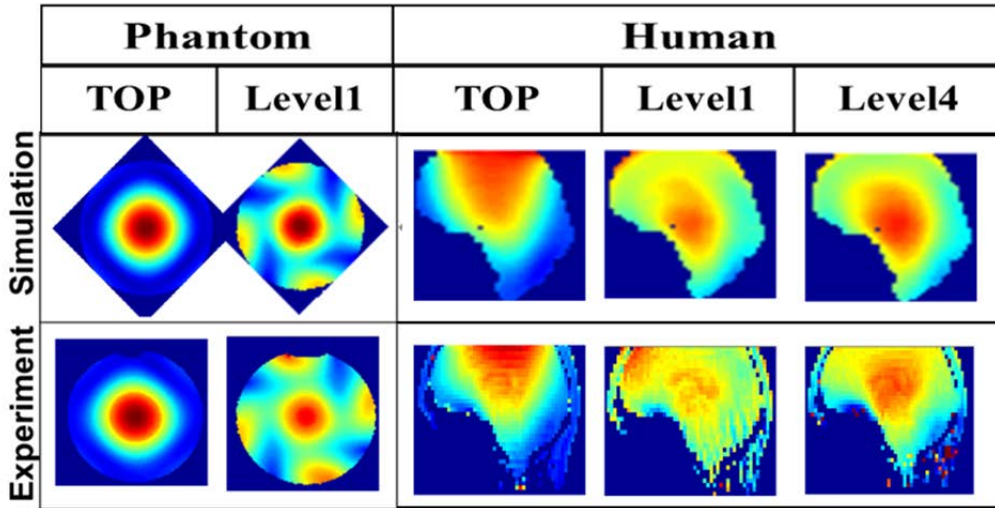


Figure 4.6: Experimental and simulated B_1^+ field distributions for the phantom and the human head. The two central axial slices of Mode1 are compared for the phantom and three central sagittal slices are compared for the human head

One preliminary uniform excitation pattern over ROI 8 (Upper Head: Central Main Brain, Periphery Main Brain plus eyes, CSF, skin and bones) with minimal average SAR was generated by a combination of these modes. The goal was to achieve the lowest possible average

SAR with $(COV = \frac{\sigma(B_1^+)}{mean(B_1^+)}) \leq 25\%$ and $(max/min = \frac{\max(B_1^+)}{\min(B_1^+)}) \leq 3$ (this optimization does

not aim at achieving best B_1^+ uniformity). Inside the ROI8, for two criteria COV and max/min are 23% and 3 respectively, the average (Watts per Kg) and peak SAR (Watts per Kg

per 10gm) were 1.47 and 5.5 respectively. The 3D B_1^+ experimental map is shown with axial slices in Figure 4.7.

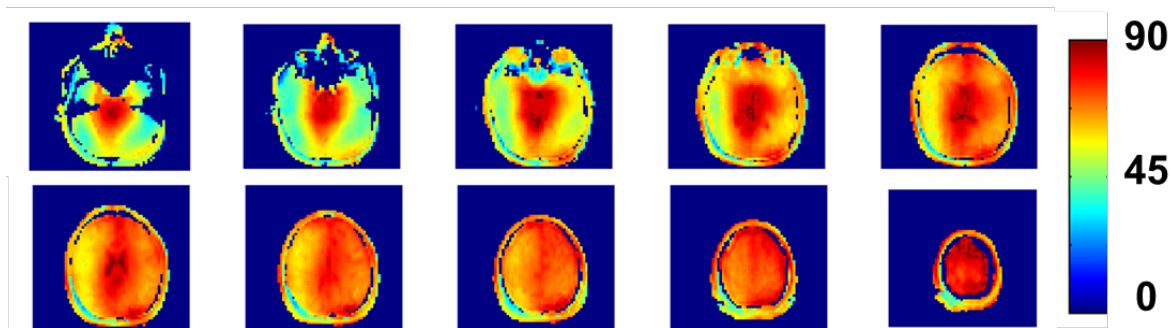


Figure 4.7: 3D *in-vivo* B_1^+ map of one optimized preliminary case. The map was normalized to maximum 90° flip angle to show the uniformity.

4.4 DISCUSSION AND CONCLUSION

Various methods have been explored to improve field homogeneity: the parallel RF excitation approach uses spatially tailored RF pulse design (125); however, it is sensitive to the measured B_1^+ maps, B_0 field shimming quality, and gradient field performance (126). There are several works suggesting the use of two modes to increase the homogeneity of the B_1^+ field distribution (126,127). The average of magnitudes over standard deviation of a 2D image can reach 1.57% by adding higher order of eigenmodes (102). However, this can come at a significant elevation of SAR and difficulties in simultaneously exciting several distinctive modes of a coil (110,128,129). In this work, a 20-ch modular coil based on Tic-Tac-Toe design performs as 5 groups of transmit arrays mounted at different locations/levels along the static magnet field (Z) direction. For each level of the coil elements, there are 4 different distinctive modes that can be generated. The modes of each group/level can be excited simultaneously. With power splitters

and phase cables, all 20 transmit channels combined into different modes and can be excited. The coil elements are physically distributed along the Z direction; hence they can be used to excite different regions in the load along the Z direction. The arrangement allows for the capability to control RF excitation not only at the XY plane but also along the Z direction.

While there can be many different solutions for the RF excitation that achieve a very similar fidelity to the targeted excitation pattern (e.g. homogenous B_1^+ field), minimizing the local SAR is the most important constraint of the optimization procedure. In this work, the average B_1^+ field intensities per 3.2 W/kg over 10 gram (average SAR) is compared for different levels, modes as well as regions. The field distributions of the eigenmodes have been tested inside a water phantom and *in-vivo* human subjects. The performance of the modes is consistent different human subjects.

The Z locations of highest B_1^+ field intensities in the load (Mode1) normally follow the physical excitation locations of Top Level, Level2, Level3 and Level4. Interestingly, the highest B_1^+ field intensity of Mode1 of Level1 (excitation locations are located near the top of the coil below Top Level) is at the lower half of the load. This can be explained by the method of mirror images where the top RF shielding cap is the ground plane. Level1 is positioned 4cm away from the ground plane. The fields close to the ground plane have been canceled while constructed at locations further down the Z axis. Since all coil elements are physically distributed along the direction of the static magnet field (Z), they can be used to excite different regions in the load along the Z direction. As such they can potentially be used for different applications. For example, the localization of Mode3 can potentially be used for the MR spectroscopy application (extracerebral lipids from the skin and skull can be suppressed to reduce the influence from this region while leaving the central brain regions unaffected (130)).

In conclusion, eigenmode arrangement of the 20-ch planer coil allows controlling RF excitation not only at the XY plane but also along the Z direction. The modes (superposed fields) from different levels can be excited simultaneously. The preliminary optimized case was presented to show that the eigenmode could be optimized and generate a uniform 3D B_1^+ excitation. RF shimming method (14,50,87,131,132) could also be used to find a uniform whole-head excitation pattern by manipulating the amplitude and phase of each of the excitation modes under specified SAR constraints, which is an ongoing effort in our work and results are presented in the next Chapter.

5.0 TRANSMIT ARRAY EIGENMODES OPTIMIZATION

5.1 INTRODUCTION

As discussed in Chapter 4, inhomogeneous distribution of the transmit fields B_1^+ (9-12) and potential high power deposition inside the human tissues (13,14) are the two major challenges that hinder the clinical application of ultrahigh field MRI. Innovative RF coil designs have been proposed to optimize the RF (SAR and B_1^+ field) performance for ultrahigh field MRI (99-101). Additionally, parallel RF transmission (PTX) is useful in improving 7T MRI B_1^+ inhomogeneity by using slice-selective RF pulses (114) and/or B_1^+ shimming methods (83,133). The eigenmode approach has also been used to solve electromagnetic homogeneity problems (98,102,103,105). For example, the image uniformity of a spherical phantom was improved by linearly combining the magnetization magnitudes with appropriate weighting factors for 8 harmonic modes (102).

Furthermore, some clinically useful images require high B_1^+ field intensity besides the field uniformity. For instance, MPRAGE, Turbo-Spin-Echo and FLAIR require a 180° pulse for the inversion/refocusing, which in turns require high B_1^+ field intensity in order to be clinically useful (228,229). This high field intensity requirement increases the difficulty to overcome the inhomogeneity and safety challenges. Therefore, the inhomogeneity and safety issues should be solved from fundamental electromagnetic theory, instead of conditional situations. From our

experience, construction of magnetic fields with destruction of electric fields will generate less SAR (44) for the required large flip angle imaging.

In this work, a 20-channel array coil (Tic-Tac-Toe based) elements are combined into 5 different rows/levels based on longitudinal (Z direction) spatial selectivity (as detailed in Chapter 4). This arrangement of the 20-ch coil allows controlling RF excitation not only at the XY plane but also along the Z direction. Eigenmodes for each level are calculated using FDTD numerical simulated fields. There are 4 distinct modes that can be excited (including quadrature, opposite-phase, anti-quadrature and zero-phase modes) for each level; there are 20 distinct modes in total that can be utilized for different excitation purposes. The B_1^+ shimming method is used to optimize these generated eigenmodes. The nonlinear optimization function used by the in-house optimization software finds a minimum of the test function with variables starting at an initial estimate of the scalar weighting. An exhaustive search is used to go through all possible eigenmode combinations. While there could be many different optimization solutions for the RF excitation that achieve a very similar fidelity to the targeted excitation pattern (homogenous B_1^+ field), minimizing the SAR and maximizing the B_1^+ intensity are two of the most important evaluation criteria. Based on the array structure, this new eigenmode excitation paradigm is able to generate uniform 3D B_1^+ fields with appropriate SAR. The optimized results have been compared with an 8-ch TEM coil. Finally, the optimization results have been verified by *in-vivo* experiments with different sequences on Siemens 7T MRI human whole body scanner equipped with 8 PTX channels. High quality whole brain (including cerebellum) 3D MPRAGE, 2D SWI and Turbo-Spin-Echo images are acquired successfully.

While PTX system can be used to generate uniform and high intensity excitation, PTX excitation may create distinct hot spots inside the human body by constructive interference of

electric fields, generated by the respective coil elements driven with individual amplitudes and phases. Monitoring global and local peak SAR is a challenging task. Pre-calculated 3D SAR modeling is widely used to estimate the SAR of the worst-case scenario. But calculations without consideration of different waveforms at different instances of time will limit their usefulness in clinical applications. The Virtual Observation Points (VOP) (15,135) method implemented on a PTX 7T MRI system shows promise in the online monitoring of the real-time peak local SAR by evaluating only a limited upper bounded set of matrices for real-time arbitrary RF waveforms. In this chapter, on-line real-time SAR monitoring workflow and verifications on the Siemens 7T MRI human whole body scanner equipped with 8 PTX channels are also presented.

5.2 MATERIALS AND METHODS

5.2.1 RF Coil and Eigenmodes

In this work, a 20-channel Tie-Tac-Toe (TTT) based head transmit array is used (detailed in Chapter 4). Figure 5.1(b) shows the assembled RF coil system, composed of 5 sets of the 2x2 TTT transmit array. The coil shielding (detailed in Chapter 6) has been designed for EPI like fast speed imaging applications (43). The 20 elements can be divided into 5 different groups/levels based on longitudinal (Z direction) spatial selectivity (107) which is also shown in Figure 5.1 (b).

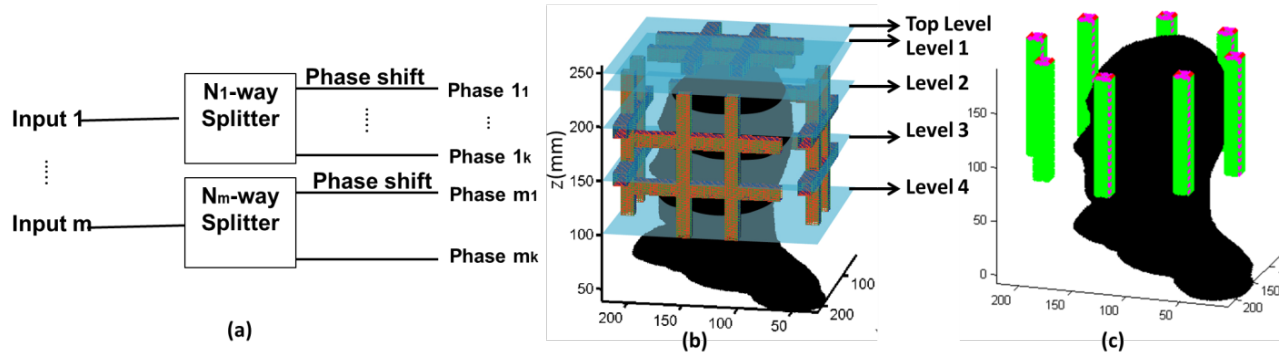


Figure 5.1: Coil arrangements. (a) Parallel transmit system connected to the coil by using N-way power splitters, phase cables are needed for specific applications. (b) TTT coil (without RF shielding) and the relative human head position. (c) TEM coil (without RF shielding) and the relative human head position.

For MRI excitation, an electromagnetic (EM) mode is determined by a specific current distribution on the array elements (110). Targeted field distributions can then be represented by the superposition of these modes. By using the field matrix (103,104), eigenmodes could be calculated as discussed in Chapter 4. For the grouped 20-ch array, there are 4 distinct modes that can be excited (including quadrature, opposite-phase, anti-quadrature and zero-phase modes) for each level; therefore 20 distinct modes can be utilized for different excitation purposes. Some of the modes excite the center area and periphery areas are excited by other modes (107) as shown in Chapter 4. Five of those modes, along the Z direction, can be simultaneously excited with power splitters (shown in Figure 5.1 (a)). The number and format of splitters used depends on specific amplitude combinations.

5.2.2 FDTD Simulations and Field Optimization

An in-house FDTD package with an accurate transmission-line feed model mechanism is implemented to model the RF performance of the TTT transmit coil (122) with a human head

model ($18.1\text{cm} \times 18.6\text{cm} \times 22.9\text{cm}$), which was rescaled from the virtual family Duke Model (124). An 8-ch TEM coil (Figure 5.1 (c)) is also simulated with the same human head model and the relative same position to compare the field distributions and SAR with the TTT coil. The transmission-line feed model properly simulates the excitation source and thus could provide more accurate quantitative values of the coil's input impedance, power input and coupling between coil elements. This simulation package has been widely utilized and been verified in many different applications (48,49,83,122,134). The nonlinear optimization function applied by the in-house optimization software finds a minimum of the test function with variables starting at an initial estimate of the scalar weighting. Since there are 1024 eigenmodes combinations (4 possible field combinations for each level, $4 \times 4 \times 4 \times 4$), an exhaustive search is used to go through all possible combinations to acquire a thorough study. For nonlinear optimization, applied initial values influence the acquired local minimum. Therefore, hundreds of random initial values are also used to fetch the global minimum for each eigenmode combination.

During the optimization procedure, the amplitude and phase of each excited eigenmode is modified with the updated scalar weighting. The uniformity of the fields that are calculated by superposition principle is the output of the optimization test function. The homogeneity is

evaluated by two criteria $COV = \frac{\sigma(B_1^+)}{mean(B_1^+)}$ and $max/min = \frac{max(B_1^+)}{min(B_1^+)}$. The calculation results

from the optimization software are processed by the in-house SAR- power calculation packages to get relative B_1^+ efficiency, absorbed power efficiency and SAR.

The transmit coil produces $B_1^+ = (B_{1x} + jB_{1y})/\sqrt{2}$, which is the circularly polarized component of the magnetic flux density that is responsible for exciting the spins. When two linearly polarized transmit fields are combined in this way, the generated B_1^+ field intensity will

be $\sqrt{2}$ times of the field intensity generated by one linear transmit field with the same applied

input power. The relative B_1^+ efficiency (130) is $B_{ef} = \frac{\sum B_1^+}{\sum |B_1^+|}$ and the relative absorbed power

efficiency is defined as $E_{ef} = \frac{\sum E^2}{\sum |E|^2}$. We aim at high relative B_1^+ efficiency to gain spin

excitation and low relative absorbed power efficiency to reduce SAR effects. Therefore, B_{ef} and

E_{ef} are used as the other two evaluation filters in the post processing procedure. The filtered

optimized cases can be optimized again to fine-tune the optimization results for specific

applications.

For the VOP method section, the field information of the human head model is also calculated by the in-house FDTD simulation package. The amplitudes and phases are processed by the SAR-power calculation package to calculate the local SAR per 10g tissue mass and absorbed power per input power. This SAR model is compressed by the VOP concepts (15,135) and set as input of the scanner VOP SAR monitoring system.

5.2.3 Experiments

All experiments in this chapter are acquired with a 7T Siemens Magnetom MRI scanner

(Erlangen, Germany). The scanner is equipped with 8 parallel transmission lines (PTX 2.2),

hence up to 8 pairs of amplitude and phase are adjustable. On the other hand, 5 independent

eigenmodes, consisting of 20 transmit channels, are optimized using the optimization software.

To get the best control ability out of the 8 equipped parallel-transmit channels and to realize the

highest power efficiency, the optimized 5 modes should be rearranged. Channels with higher

intensities could be used independently; the rest could be combined by 2-way or 4-way combiners. RF shimming profiles can then be implemented by applying various amplitude and phase combinations into the 8 parallel transmission channels.

The optimized uniform excitation pattern obtained from the shimming optimization method is tested by manipulating the amplitude and phase of each excited mode under allowed SAR constraints. The optimization results are tested using a water spherical phantom (107) and *in-vivo* (>15 human subjects who signed consent forms approved by the Institutional Review Board at the University of Pittsburgh). *In-vivo* B_1^+ maps are acquired using saturated turbo FLASH methods (SatTFL) and 8 flip angles are acquired for each measurement. 3D MPRAGE images, 2D SWI and Turbo-Spin-Echo are also acquired.

5.3 RESULTS

5.3.1 Slice Excitation Verification and Limits of Homogenous Slice via RF

Shimming

Slice-selection is important for MRI applications and RF pulse design methods including multi-band approaches (230). Before studies of 3D volume excitation in this chapter, the possibility of the slice selective homogenous excitation is demonstrated from axial and sagittal images of the phantom and the human head in this section. The cost to achieve the ultra-uniform slice selection images using the RF shimming method is also discussed. Testing is done with water phantom (dielectric constant = 78 and conductivity = 0.46 S/m) and 3 *in-vivo* human subjects.

The magnitudes maps of two modes that can be simultaneously excited using different groups of coil elements are shown in Figure 5.2. The phase maps are measured when all channels are in phase (relative phase being zero) and three of them are shown in Figure 5.2 phase map. Figure 5.3 displays the experimental and simulated B_1^+ maps associated with RF shimming that targets homogeneous excitation. The results show that the simulation results are in excellent agreement with the experimental measurements. The ratio of maximum to minimum B_1^+ intensity in the slice of interest is 1.1 in the simulation and approximately 1.2 in the experimental B_1^+ map for the phantom axial slice. For the sagittal slice, maximum to minimum ratio in the simulation is 1.5 and approximately 1.7 in the experimental B_1^+ map. These ratio differences between simulations and experiments could be caused by the measurement errors (from slice thickness, slice location, loading property changes, etc.). Unique excitation patterns are also in excellent agreement with experimental findings (Figure 5.4).

For the human studies, the maximum to minimum ratio inside the brain slice in addition to the skin/bone is 1.2 in the simulation (COV is less 4.6%), while 1.4 is achieved for the *in-vivo* B_1^+ map. With respect to global average SAR=2.6 Watts/Kg/10g (inside the 3D whole head and per 1.97uT). If considering the pseudo CP mode as an initial excitation to compare, its maximum over minimum is 5.4 at the same slice, the average SAR is 2.3 Watts/Kg/10g inside the 3D whole head. In general, homogenous slices come with more average SAR for this case.

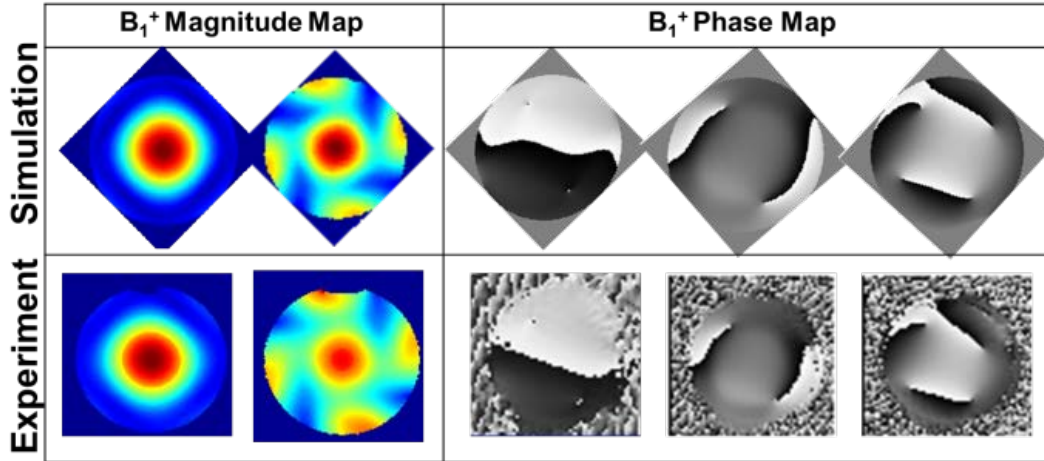


Figure 5.2: Experimental and simulated B_1^+ magnitude and phase maps

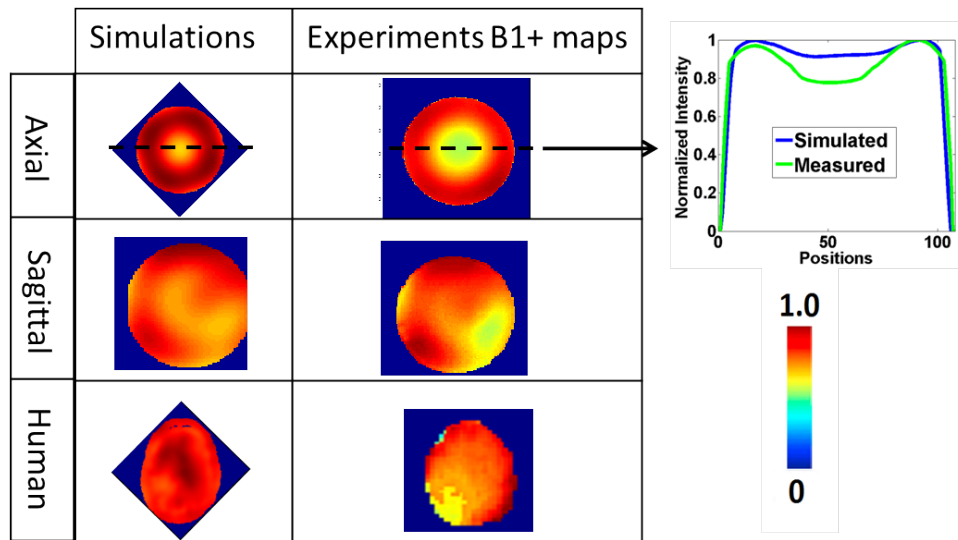


Figure 5.3: Experimental and simulated B_1^+ magnitude maps of axial and sagittal slices targeted for homogeneous excitation.

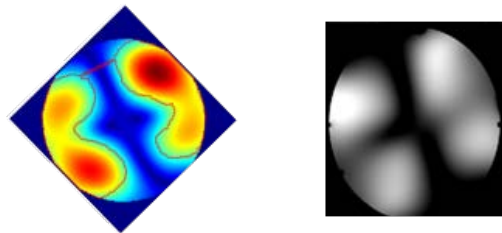


Figure 5.4: Phantom localization

In conclusion, simulation based ultra-homogenous slice excitation can be achieved by B_1^+ shimming in conjunction with this multi-channel highly coupled TTT array and PTX system, although average SAR and B_1^+ intensity may be sacrificed to achieve this goal.

5.3.2 3D Field Simulation Verification

In this section, the simulated 3D field distribution and intensity are verified by the *in-vivo* B_1^+ maps. One of the shimmed B_1^+ field distributions is verified by the *in-vivo* B_1^+ maps in Figure 5.5. In addition, the average of the measured flip angle inside the brain is 600° per 1000 V (nominal) for a 1ms square pulse. Considering the power loss between the system input and the coil input level ~ -3.5 dB and $\theta = \gamma B_1 T$ the average B_1^+ intensity = $56 \mu T$. In the simulations, for the same region of the interest average $B_1^+ = 60 \mu T$. This verification has been applied across different human subjects and different shimming excitations. Therefore, the FDTD simulation method can be applied not only to modify/optimize B_1^+ distribution but also to compare field efficiency in this work.

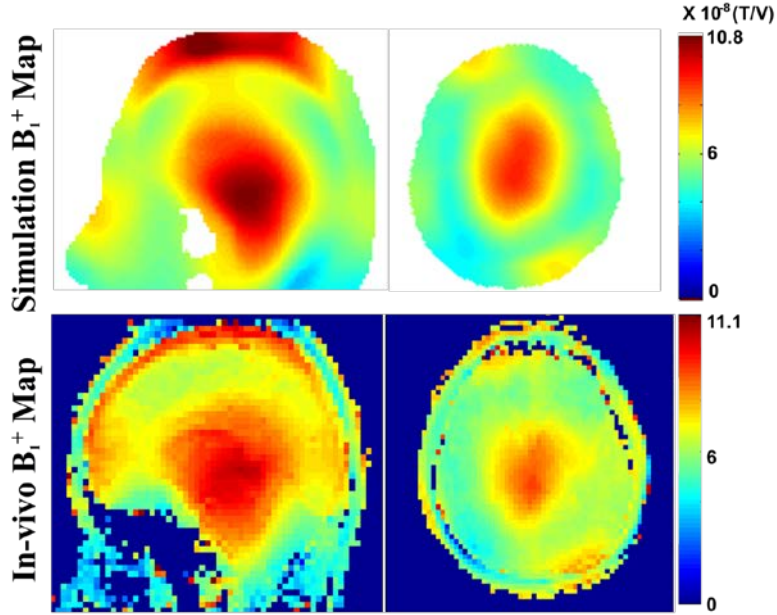


Figure 5.5: The 20 ch pseudo quadrature mode (not optimized for homogeneity nor SAR.) Simulated magnetic fields compared with measured magnetic field distribution (sagittal and axial slice). *In-vivo* B₁⁺ maps were measured using Saturated Turbo Flash method (1ms square pulse); cable loss was taken into consideration for the intensity calculation.

5.3.3 Transmit Field and Absorbed Power Efficiency

Examples of the simulated transmit fields and power efficiency comparisons are shown in Figure 5.6. For the top 4-ch quadrature polarization case: inside the whole head, B_{ef} is 85%, which indicates the B₁⁺ field is constructing in most of the volume and especially inside the middle of the brain; E_{ef} is 56%, max/min is 12.6 and COV is 0.54. For the 20-ch pseudo quadrature excitation case: B_{ef} is 65% E_{ef} is 32%; the B₁⁺ is uniquely constructed from the ventricle to the cerebellum (more than 90%); max/min is 2.97 and COV is 0.22. From the relative B₁⁺ efficiency and absorbed power efficiency, the 20-ch pseudo quadrature excitation case could generate about 30% higher B₁⁺ when absorbing the same amount of power. For both cases, there

is one small area where the absorbed power efficiency is almost zero, which indicates very low SAR in this area. Based on these analyses, optimized B_1^+ field uniformity could be obtained while reducing E field construction.

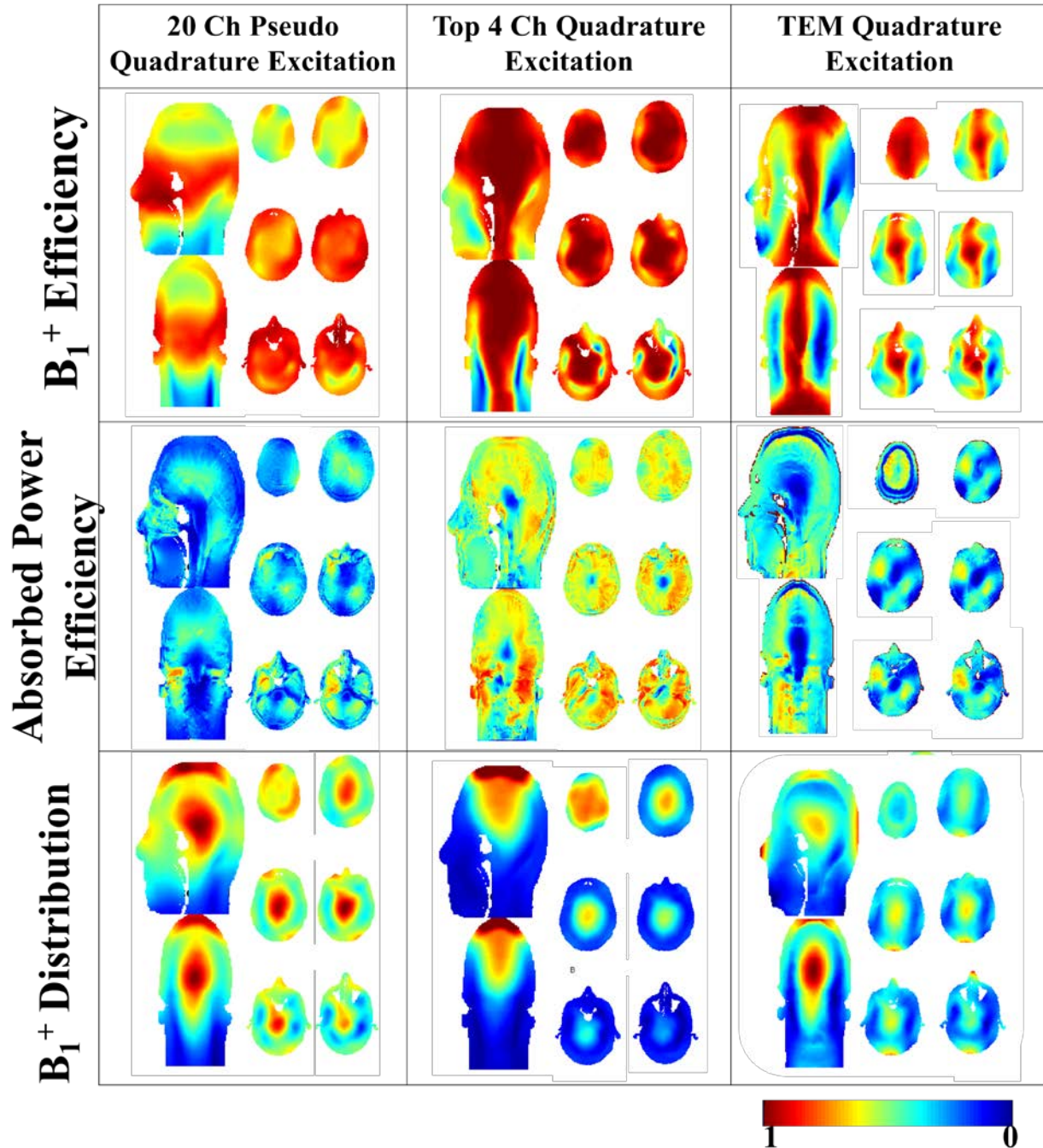


Figure 5.6: TTT 20-ch pseudo quadrature excitation and quadrature excitation generated by the top 4-ch quadrature excitation compared with TEM quadrature excitation.

5.3.4 Optimization Criteria Comparison

Characteristics of the field uniform are compared in Figure 5.7. In the subfigure of max/min with COV, the results are separated into two groups by max/min=25 line. Inside the two groups, max/min and COV are generally consistent with each other; i.e. good uniformity normally translates to low COV and max/min (shown in the zoomed subfigure). This separation between the two groups is mainly caused by two reasons: 1) mode combinations are totally random and there are some mode combinations that only excite the peripheral areas. Most of these cases will appear in the large max/min and COV region and 2) for the cases of large max/min with small COV. They represent the cases where there are “dark” local areas. These “dark” regions may only be one or two pixels having a minimum value which leads to a high max/min while COV is minimally affected.

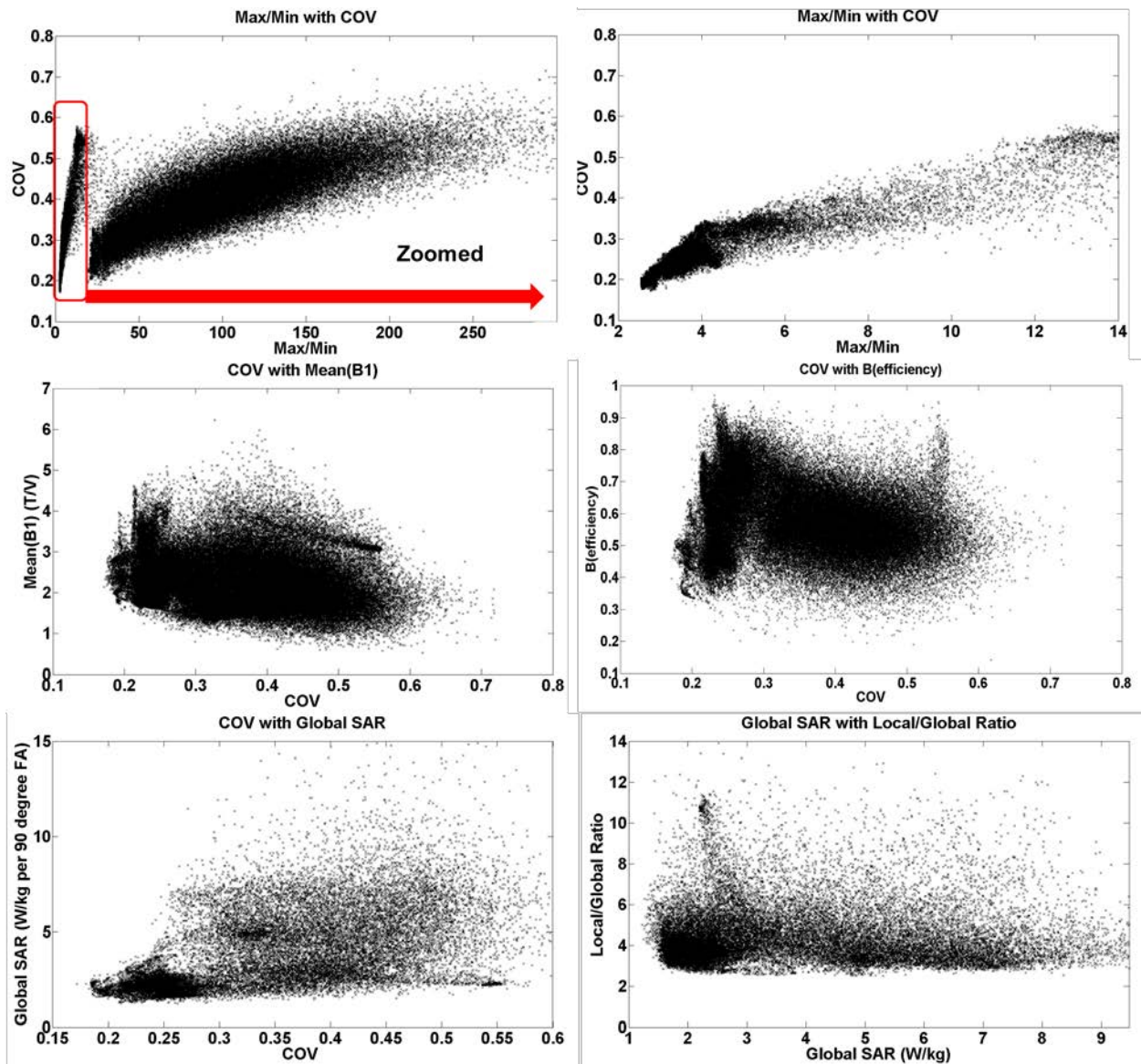


Figure 5.7: Field uniformity (COV, max/min), efficiency, SAR distribution for all of the optimization results.

Subfigures COV with Mean (B_1^+) and COV with B (efficiency) in Figure 5.7 show high B_1^+ intensity could be generated by a good uniformity case, although the most uniform case may not be the most efficient case. Subfigure COV with Global SAR in Figure 5.7 shows that although the nonlinear optimization function is only used to optimize the uniformity (COV and/or max/min), global SAR also decreases. For the ratio of peak local SAR over global SAR:

85% of the peak local SAR to global SAR ratio are less than 5 and 60% of them are less than 4. Notice that field efficiency and SAR in this work are normalized: average SAR (W/kg per $1.97 \mu T$ which is the field intensity required when using a 3ms square pulse generating a 90 flip angle excitation inside the ROI) and B_1^+ intensity (B_1^+ per input voltage) is normalized to the top 4-ch quadrature mode.

5.3.5 Comparison between Different Coils and Applications

In Figure 5.6, for the TEM quadrature excitation, the absorbed power efficiency map shows the E field constructs towards the periphery of the head while the for the TTT 20 Ch pseudo quadrature excitation the E field constructs towards the middle of the brain. Since the E field intensity is always high at the periphery, the E field construction at the periphery of the head could lead to high average/peak SAR values.

In order to generate a homogeneous field distribution with small SAR and high field intensity for large flip angle applications, field efficiency and SAR are used to evaluate and filter the optimized results. Then the selected cases are fine-tuned for two different optimizations (i.e. optimization 1 with good uniformity for SWI and optimization 2 with high intensity for MPRAGE). The B_1^+ distributions of these two optimization results are shown in Figure 5.8. The minimum and maximum flip angle values inside the two measured *in-vivo* B_1^+ maps are labeled inside the black circle and values are shown within the red boxes. TTT optimization 1 generates better uniformity than TTT optimization 2, while the mean intensity is ~30% less.

Their calculated parameters are also compared with the simulated TEM coil's quadrature excitation which is shown In Figure 5.6. The SAR values are: 2.1 W/kg for TTT optimization 1, 1.75 W/kg for TTT optimization 2 and 2.2 W/kg for TEM (per $1.97 \mu T$) inside the whole brain

including the cerebellum. However, the uniformity COV is significantly different: 18% for TTT optimization 1, 20.2% for TTT optimization 2 and 29.4% for TEM.

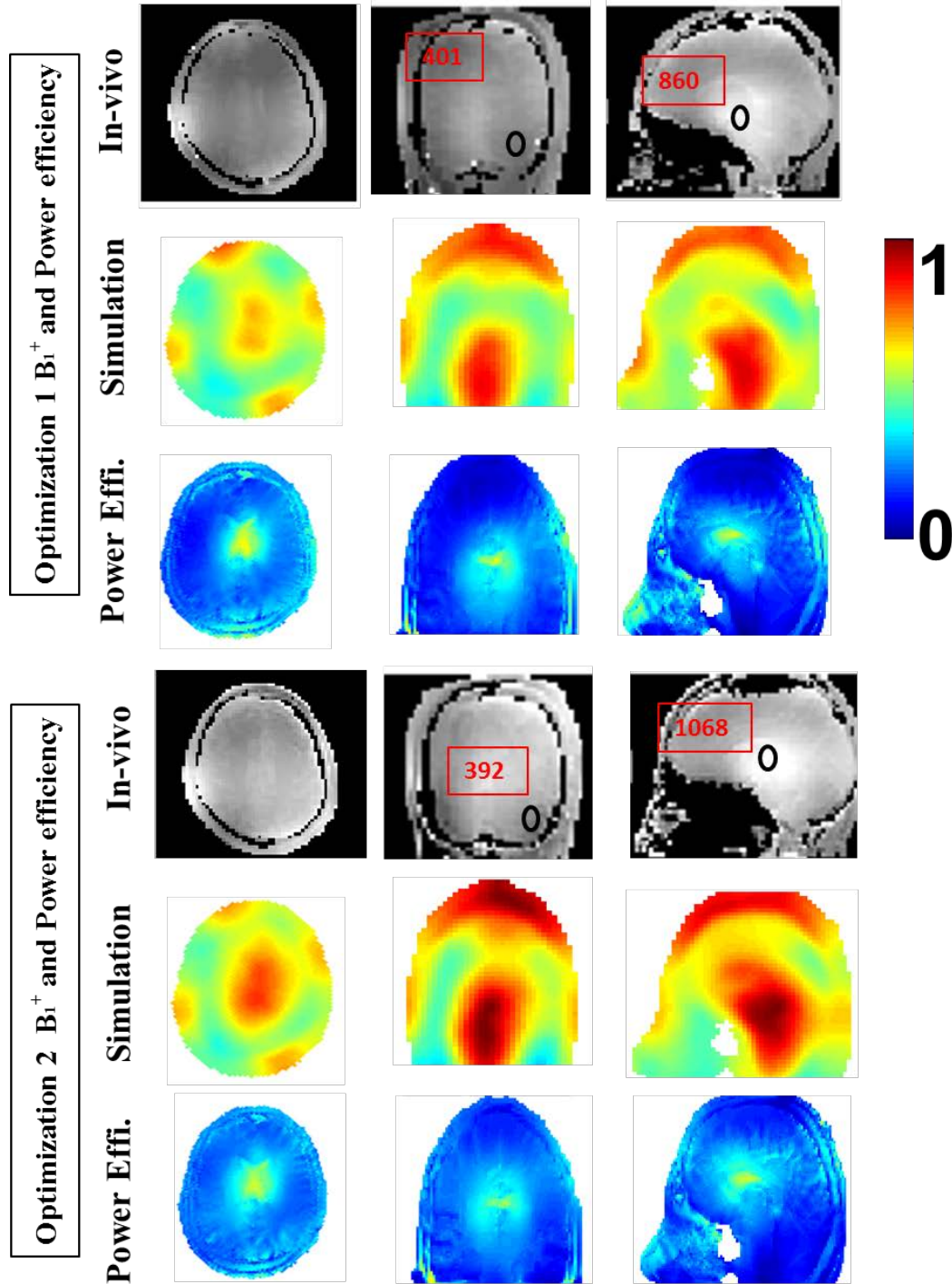


Figure 5.8: B_1^+ distribution from two different optimizations. B_1^+ efficiency is 52% and 61% for Optimization 1 and Optimization 2 respectively; absorbed efficiency is 20% and 19% respectively.

5.3.6 Experimental Verifications

The optimized cases are then implemented with the 7T MRI by varying the input phase and amplitude in the 8 PTX system. For the 3D MPRAGE images, resolution is $0.9\text{mm} \times 0.9\text{mm} \times 1\text{mm}$, TR 3000 ms, TE 2.32 ms, TI 1200 ms. The 3D MPRAGE images are shown in Figure 5.9 with axial, coronal and sagittal slices. This case has also been applied to TSE (Figure 5.10) and other sequence applications requiring large flip angles. Figure 5.11 are the coronal slices of MPRAGE and SWI images to demonstrate the excitation coverage.

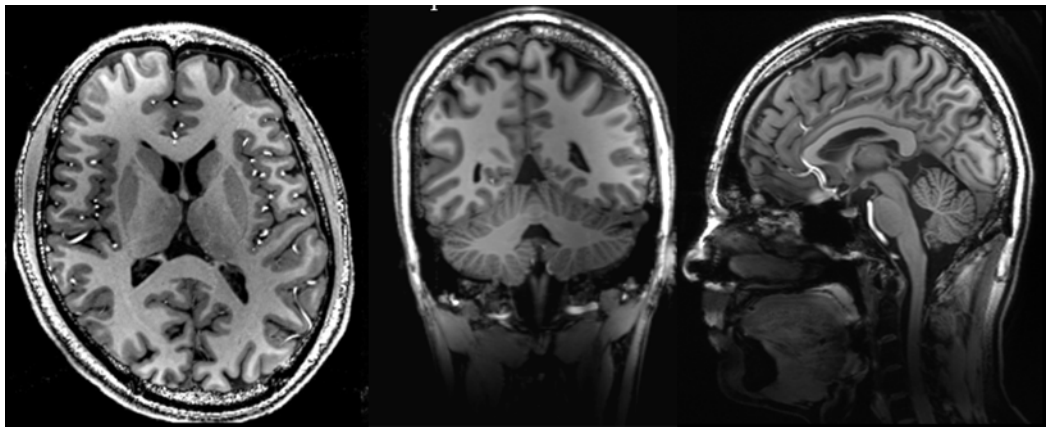


Figure 5.9: *In-vivo* 3D MPRAGE images ($0.9 \times 0.9 \times 1.0 \text{ mm}^3$, TR/TE/TI = 3000/2.32/1200 ms, ~10 minutes).

The images are obtained by Dr. Ibrahim's Lab.

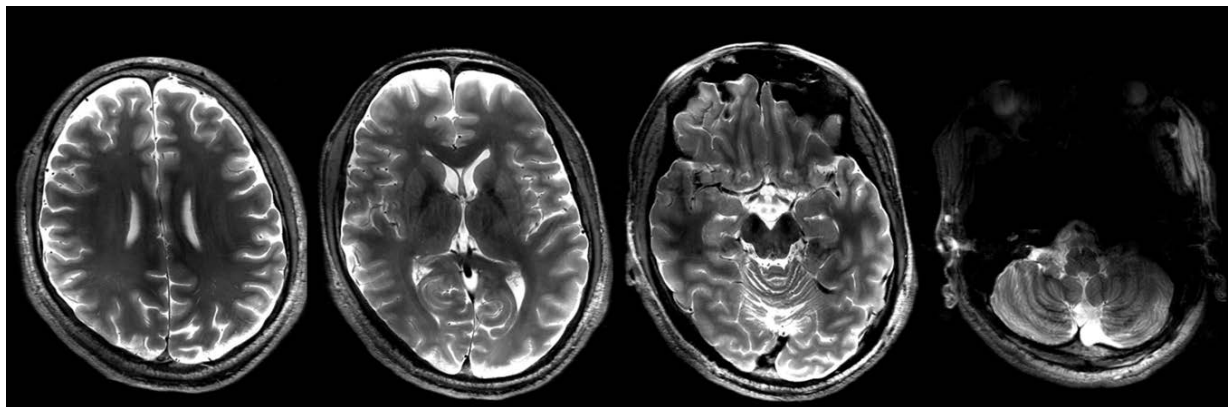


Figure 5.10: *In-vivo* Turbo Spin Echo with GRAPPA 2 ($0.4 \times 0.4 \times 2 \text{ mm}^3$, TR/TE=14000/54ms). The images are obtained by Dr. Ibrahim's Lab.

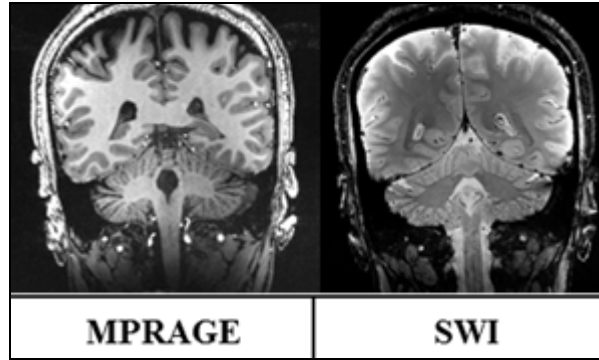


Figure 5.11: MPRAGE and SWI images to show the excitation coverage. The images are obtained by Dr. Ibrahim's Lab.

5.3.7 20 Modes and B_1^+ shimming Optimizations Comparison

The 20 channels can also be combined directly. In this section, 20 different eigenmodes are generated by 20 different amplitudes and phases. The mode order can be arranged following the field intensity or λ_i as illustrated in equation (4-2) and the maximum field intensity is the Mode 1. There are 20 modes can be generated and they have also been optimized by using the in-house optimization software and results are shown in Figure 5.12. This optimization is used to test the optimal uniformity from this 20-Ch coil and it is done with increasing number of the inputted modes. In Figure 5.12, the case #1 represents Mode1 with the second mode as the input; case #19 represents Mode1 with the other 19 modes (Mode2-20) as the input. The optimizations are done on the entire 3D head model (ROI 6) and the brain (ROI 8) (ROIs are shown in Figure 4.1).

Figure 5.12 shows that when more modes are included into the optimization procedure, the field's uniformity improved significantly. The best COV is 10% for this whole brain region and the max/min is 1.55, while for the whole head the best COV is 14.9% and the max/min is 1.89.

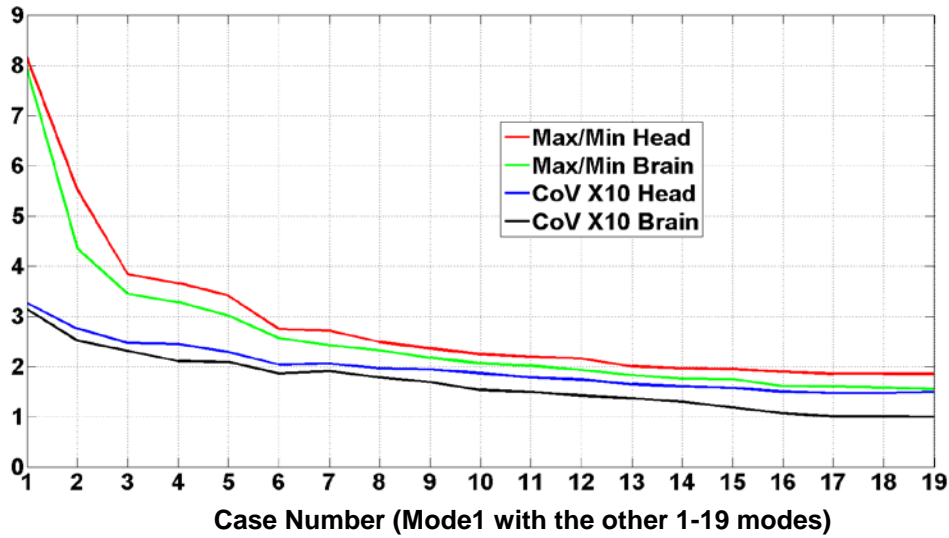


Figure 5.12: 20 modes optimization inside the head and brain

5.3.8 Virtual Observation Points Applications and Verification

All experiments in this section are done with a 7T Siemens MRI scanner (Erlangen, Germany) equipped with 8 channel parallel transition (PTX Step 2.2 system). The 8 directional couplers (DICO), shown in Figure 5.13, pick up the real-time amplitudes and phases of the transmitted RF pulses. The pulse information is used to calculate global power transmitted into the coil as well as an input to the VOP SAR model to calculate real-time local SAR. The 20-ch transmit/receive array (122) with the TR switch box is used to excite different transmission patterns driven by different phases and amplitudes.

From the conservation law, within the region of interest, the supplied power P_s is equal to the power P_e exiting the region plus the power P_d dissipated inside the region (absorbed by the

human body) plus the energies stored within that region (magnetic and electric energies \overline{W}_m and

$$\overline{W}_e) P_s = P_e + P_d + 2j\omega(\overline{W}_m - \overline{W}_e).$$

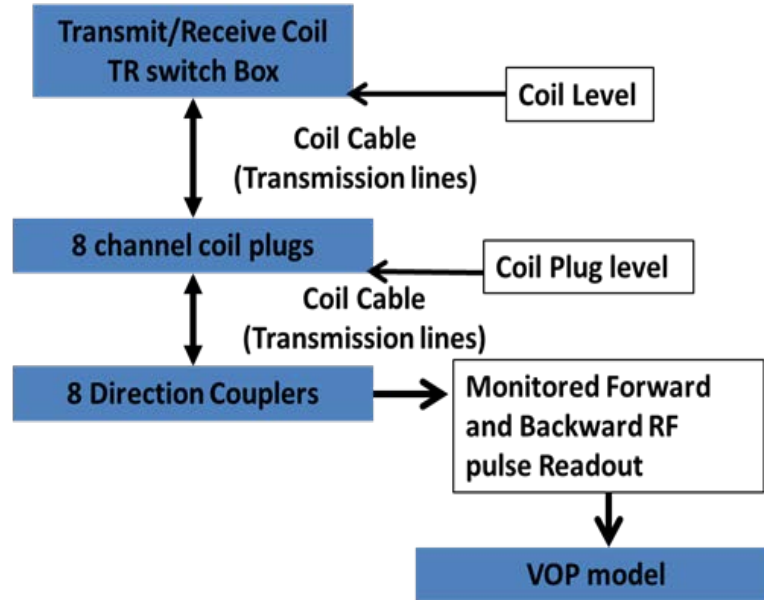


Figure 5.13: Global and local SAR monitoring pathway

An FID sequence is applied and the input voltage is 50 V per channel (at the coil plug level), the applied RF pulse is a 2 ms rectangular pulse, TR=200 ms, therefore the input power per channel is 0.5 W. Five different combination cases (Figure 5.14) are tested by driving different phases and amplitudes on the 20-ch coil. The results in Figure 5.14 show the excellent agreement between the calculated global power and the measured global power (forward-backward). The local SAR calculations also match the VOP measured results.

Taking one particular mode as an example (combination 3 in Figure 5.14), the real input forward power is measured to be 3.12 W at the DICO level (Figure 5.13) when counting the cable loss, and etc. The backward (from reflected and coupling) power is 0.31 W at the DICO level. As a result, the calculated total global power is 2.8 W (3.12 W-0.31 W) at the DICO level. The measured global power was 2.6 W at the DICO level from the PTX system.

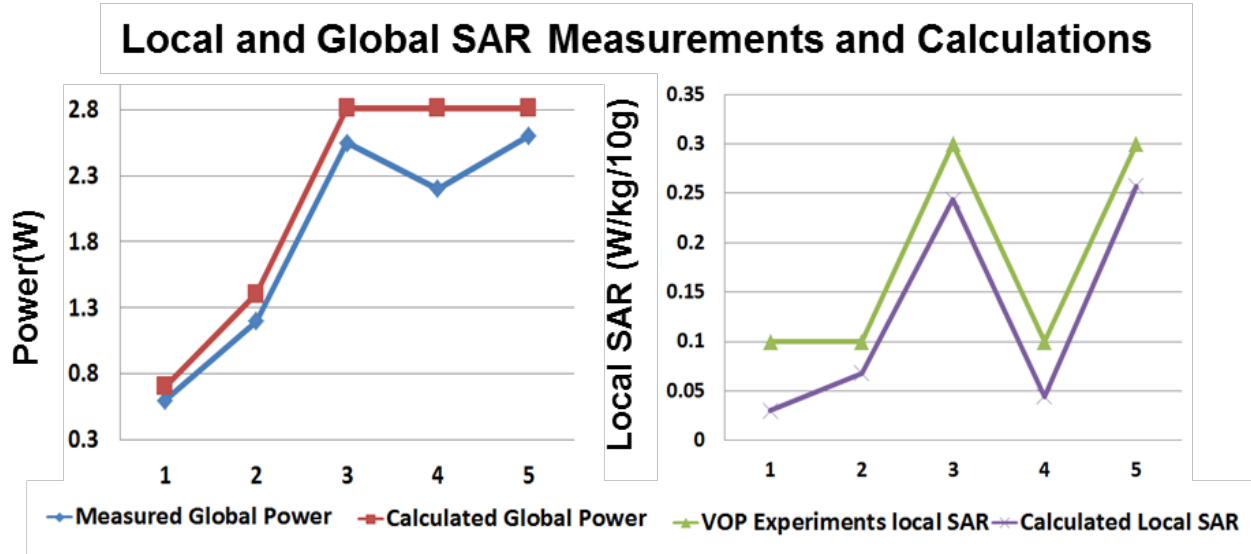


Figure 5.14: Global power and local SAR verifications with VOP supervision

To calculate the local SAR, it is noticed that the measured global power includes the power absorbed by the head and the power radiated out of the coil. For case 3, the absorbed ratio is about 28% of the total supplied real power. Taking the model mass and measured global power into considerations, the peak local SAR = 0.25 W/kg/10g which still closely matches the overestimated (because of the VOP theory) VOP local SAR measurement (0.3 W/kg/10g). As a margin of safety, the VOP measured peak local SAR is normally 10% more than the real/simulated peak local SAR, which is also shown in the Figure 5.14.

5.4 DISCUSSION AND CONCLUSION

In this work, the 20-ch modular coil operating as 5 groups of transmit arrays mounted at different locations along the static magnet field (Z) direction is evaluated. The coil elements are physically distributed along the Z direction; hence they could be used to excite different regions in the load along the Z direction. For each level of the coil elements, there are 4 different modes that can be generated. The modes of each group/level could be excited simultaneously. The field distributions of the eigenmodes have been tested inside a water phantom and *in-vivo* human subjects in Chapter 4. The modes are consistent with different human subject loads. Based on different criteria, different modes could be chosen for various applications.

The FDTD simulation method is verified by *in-vivo* B_1^+ maps: both the field distribution and field intensity are comparable to the measured fields. Therefore, the simulation results are applied not only to modify B_1^+ distribution but also to compare field efficiency. Field construction distribution is also studied where the left-right asymmetry inside the B_1^+ distribution, comes from the asymmetry of the human head from front-back (136).

The eigenmodes are calculated by the simulated fields and are then optimized with an in-house optimization tool box. RF shimming (B_1^+ optimization) is a complex procedure: magnetic field uniformity, magnetic field efficiency and power deposition (SAR) have to be considered together to get clinically useful images. In our experience, the shimming procedure could normally be separated into a macro optimization and micro optimizations. Macro optimization generates a generally good uniformity, efficiency and SAR. For specific applications, the macro optimization result could be used as an initial input and be optimized under specific conditions (SAR, uniformity, coverage, efficiency and etc.). The preferable cases should be high coil excitation efficiency and less SAR. In addition, COV provides more global information (how

wave propagates) and max/min provides more local information (how fields interfere with each other). A good COV case normally comes along with a symmetric field distribution. Normally one low max/min accompanies a low COV, while a low COV could generate high max/min when there is one tiny dark spot. By using the described eigenmode approach, we are able to reduce the fields' variation from an original level of ~30 % down to less than 18% inside the head and 10% inside the brain including the cerebellum; max/min reduced from ~8 to 1.89 inside the head and 1.55 inside the brain, when the 20 channels are combined directly.

Based on the exhaustive searches of the 5 levels' eigenmode optimizations, the nonlinear function used in this case could generate good SAR cases with high field efficiency, although RF shimming only optimized the field uniformity without consideration to the other constrains. One of the optimization cases is selected for large flip angle (e.g. MPRAGE) applications. This case has significantly better field uniformity inside the whole head (including the cerebellum) when compared with an 8-ch TEM coil. The uniform field distributions are validated across different human subjects. High quality 3D MPRAGE images are acquired. They are currently applied to late-life diseases studies.

The system global power and the local SAR from the VOP model in conjunction with rigorous RF modeling that incorporates coupling are demonstrated and verified by experiments acquired using the Parallel RF transmission system. The input simulated SAR model is also verified quantitatively using B_1^+ maps as well as local VOP SAR monitoring.

6.0 DUAL OPTIMIZATION METHOD OF RF AND QUASI-STATIC FIELD SIMULATIONS FOR REDUCTION OF EDDY CURRENTS GENERATED ON 7T RF COIL SHIELDING

6.1 INTRODUCTION

Gradient magnetic fields are used for information encoding in MRI. The gradient magnetic fields (≤ 10 kHz) (137) can induce eddy currents in conductive materials of the MRI system (superconducting magnets, RF and gradient coil shielding, etc.). The generated eddy currents decay exponentially with relatively long time constants, typically tens or hundreds of milliseconds (138), which in turn can generate a second, distorting, magnetic field in the region of interest (ROI). This second magnetic field can generate severe image artifacts (137); it can also offset the superconducting operation point of the main magnet and even cause quench problems (139). Previous works have proposed methods of calculation (139-144) and reduction of the eddy currents on the magnet cryostat (145); these include active gradient shielding (146) and pre-emphasis (147,148) methods. These system level eddy-current compensations are typically available on current clinical scanners. Besides these system level compensation methods, post-processing methods were also discussed for eddy current compensation (149-151). In general, the success of these gradient imperfection correction methods rely on the image

contrast differences, the accuracy of the measurement of the actual k-space trajectories, and/or the model of the gradient field distortions.

Less discussed are quantitative studies and correction of the eddy currents due to the RF shielding of RF coils. The RF shielding can play a major factor in improving transmit efficiency as well as maintaining the distribution of the excitation field (152). Especially for ultrahigh field ($\geq 7\text{T}$) MRI, the RF shielding is oftentimes one essential component for the transmit coils (17-21). Proper design of the RF shielding is particularly critical for echo-planar imaging (EPI) and 7T MRI parallel transmission (PTX) applications, since many of the PTX trajectories use spiral or EPI type gradient waveforms and these gradient waveforms can change rapidly (22,23). The fast changing gradient waveforms induce intensive eddy currents that can considerably distort the image quality. Furthermore, different transmit RF coils (i.e. head/knee/breast) are used with 7T MRI scanners and the RF shielding varies with the different coil designs, rendering the system eddy current correction possibly insufficient. In addition, the spatially non-linear eddy current behavior in regions close to the RF coil copper shielding may also render the above-mentioned post-processing methods less reliable. As a result, eddy currents induced on RF coil copper shielding could be very problematic.

Several works have analyzed methods of adding axial and azimuthal slots to reduce eddy currents on the RF shielding for birdcage coils and TEM coils (40,153-157). Capacitors are sometimes added at specified locations between the slots to avoid high-frequency RF field radiations (155). Fingerprint-like patterns have also been utilized (155,158). Multiple thin copper layers were discussed and their performance could be somewhat transparent for the MR gradient fields and efficiently block high frequency electromagnetic emission (137). Slotted double sided copper shields could be used to reduce gradient fields induced eddy currents as the

copper shielding will be close to opaque for the RF signal because of the large capacitance between the overlapped shields (157).

In this work, we propose a methodology that aims at minimizing eddy currents induced on RF-coil shielding. The induced gradient field distortion (due to eddy currents) is quantitatively studied in the time and frequency domains. Successful MRI gradient fields' measurement validation is delivered to verify the simulation results. Eddy current characterization is also studied based on the eddy current response function. A comprehensive optimization method, guided by full wave electromagnetic simulation combined with the eddy current simulation, is developed to maintain the RF-coil's RF characteristics and simultaneously reduce low frequency magnetic field distortions due to eddy currents on the RF coil shielding. The methodology is successfully tested on a Siemens 7T human whole body scanner with 1) a four-element, 2x2 Tic-Tac-Toe transmit/receive (Tx/Rx) array design (106,159) with an oil phantom and two *in-vivo* human subjects and 2) an RF coil system composed of 5 sets of the 2x2 Tic Tac Toe transmit coil (total of 20 Tx elements) in conjunction with a 32-ch receive coil insert with 10 *in-vivo* human subjects.

6.2 METHODS

6.2.1 The RF Coil

New RF coil designs are desirable (160) in order to approach optimal RF coil performance at ultrahigh fields (42,120,161-171). Various and extensive RF shielding designs, in terms of shape, thickness and dimensions, may be necessary in order to achieve the optimal RF coil

performance (transmit field distribution and field intensity). The proposed methodology is intended to be effective with any RF coil design, shape and/or geometry whether it is azimuthally symmetric or follows 4-fold symmetry and etc.; and/or possesses distinctive RF current patterns on the coil shielding. In this work, one set of a four-element, 2x2 Tic-Tac-Toe (TTT) head coil structure is selected and constructed. The view from foot to head of the assembled head coil is shown in Figure 6.1(a1). This four-element module is placed on the top of the head and functions as a Tx/Rx coil. The five flat and square-shaped copper RF shielding panels are positioned around the 2x2 coil structure. These panels are designed in a fashion that copper shielding could be easily switched to different types (172). The schematics of these 5 panels of RF copper shielding (3D) are shown in Figure 6.1(a2). The side view of the copper shielding is shown in Figure 6.1 (a3).

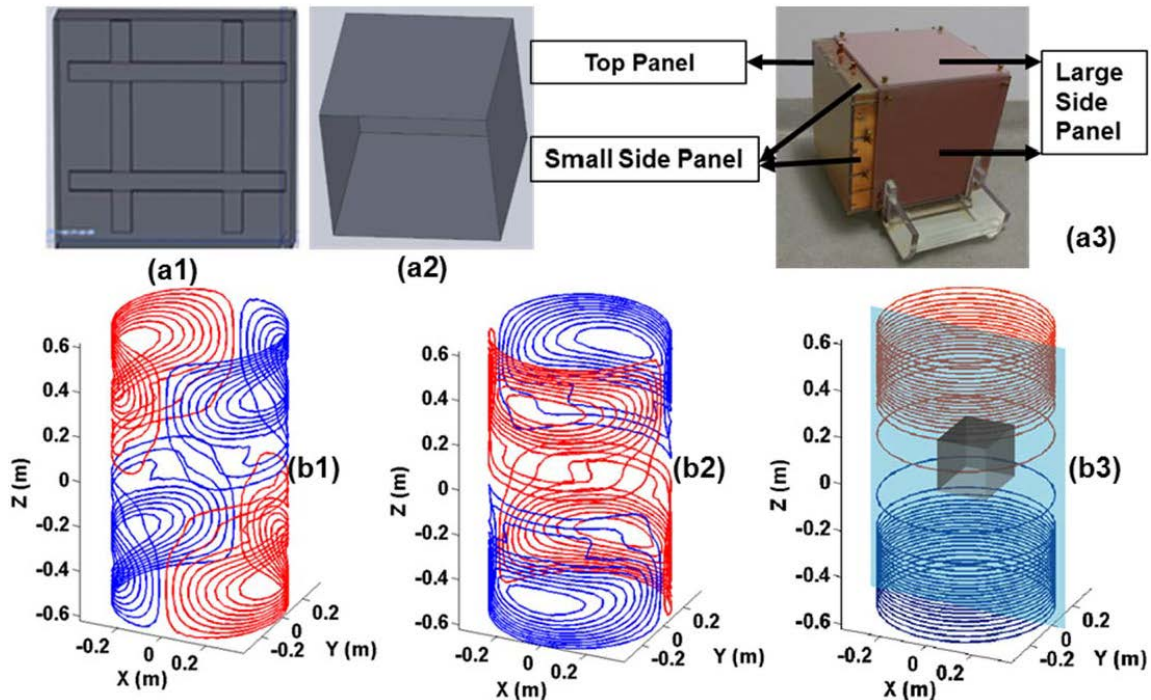


Figure 6.1: Schematics of the coil, RF shielding and gradient coils

(a1) Tic-Tac-Toe transmit/receive elements and (a2) RF shielding. (a3) Copper shielding components. Schematic diagrams of (b1) X gradient coil; (b2) Y gradient coil; (b3) Z gradient coil with the copper

shielding to show the coil relative position. Red and blue colors indicate opposite current directions. The Y=0 plane is represented by the light blue color plane.

In order to study the influences of different shielding shapes, another RF coil's shielding has been studied. RF shielding designs for TEM coils and birdcage coils were reported (40,173). The shielding of these RF coils are normally cylindrically shaped with a cap shielding on top of the coil. In this work, the eddy current distortion of two different RF shielding shapes that are associated with two 7T RF coil types- TEM coil and TTT coil- are simulated, measured and compared. The two copper shielding are defined as circular shielding and rectangular shielding because of the shape of the cross-section. The computation are performed *in-vivo* and in phantoms and using Tx-SENSE.

6.2.2 Gradient Field Induced Eddy Current Simulations (FEM)

Approximate models of the Siemens (Erlangen, Germany) 7T MRI whole body gradient coils have been designed using the Stream Function Method (174) to match the size and region of gradient linearity of the coils in the system. The designed gradient coil wire loops are shown in Figure 6.1(b1-b3). The Siemens whole body gradient coil has the following characteristics: the inner diameter is 683 mm; Gmax in X, Y, Z are 40/40/45 mT/m, respectively; maximum slew rate is 200 T/m/s; imaging FOV is 500×500×420 mm; linearity is 5%. Three gradient coils generate three essential gradient magnetic fields for image information encoding and they are: $B_z = G_x x$, $B_z = G_y y$, $B_z = G_z z$. Based on Maxwell's Equations, there are concomitant fields with these three gradient fields. For X gradient coil, $B_x = G_x z$, $B_y = 0$; for Y gradient coil,

$B_x = 0$, $B_y = G_y z$; for Z gradient coil, $B_x = -G_x x/2$, $B_y = -G_y y/2$. The Z component of the gradient fields is dominate at the center of the gradient coils, where the RF coil is placed (157).

Models of a 40- turn Z-gradient coil (radius of 341.5 mm and wire diameter of 6.7mm) and a 36-turn X-gradient coil (radius 341.5mm and wire diameter of 4.2 mm) were constructed in SolidWorks (Waltham, MA, USA). Z-gradient coil positions along the Z-axis are given in Table 6.1. The X and Z-gradient coils and the RF coil models are imported into ANSYS Maxwell 14.0 (Canonsburg, PA, USA). The passing currents are set up to mimic the current flow inside the gradient coil wires when applying different scan protocols. The eddy current distortions are calculated and studied in the time and frequency domains by the Maxwell Transient Solver and Eddy Current Solver respectively.

Table 6.1: Z-gradient coil arrangement

Coil positions along (\pm) z-axis (in mm)				
131	261	293	316	335
352	368	383	399	413
429	444	460	476	493
511	530	550	573	598

The simulated Z-gradient fields (time domain) are used to compare with the measurements. The eddy current characteristic is then studied based on a characterization method using the eddy current impulse response function (23,175). The eddy current-induced magnetic fields can be derived as the convolution of the negative time-derivative of the ideal gradient waveform and the eddy current response function $H(t, z)$ (175) (6-1). In this work, $B_d(t, z)$ is the ideal gradient field and $B_E(t, z)$ is the eddy current-induced gradient field. The eddy current impulse response function $H(t, z)$ is the sum of multiple exponential terms with constant time τ_n and variable amplitude parameters α_n (23,175) (6-2).

$$B_E(t, z) = -\left(\frac{dB_d(t, z)}{dt}\right) \otimes H(t, z) \quad (6-1)$$

$$H(t, z) = u(t, z) \sum_{n=0}^{N-1} \alpha_n(z) e^{-t/\tau_n(z)} \quad (6-2)$$

where $\mu(t, z)$ is the unit step function and N is the number of the exponential terms.

The frequency domain results are used to compare the distortions from 1) X and Z-gradient coils, 2) different copper thicknesses, and 3) the top panel, since there is no top shielding for some RF coils (17,18,152,153). These gradient field simulation results are used as a guide for the study of eddy current reduction.

Models of circular shielding (normally used for Birdcage coil and TEM coil) and rectangular shielding (used for Tic-Tac-Toe coils) are also constructed in SolidWorks (Waltham, MA, USA). The 3D models are shown in Figure 6.2. One cavity end is capped and the other is open. For the copper shielding comparison study, the two RF coils (TEM and TTT) used 18 μ m thick copper and had the same dimensions in terms of heights and widths. A 4-element Tic-Tac-Toe (TTT) transmit/receive array and a 4 channel TEM head array are built, shown in Figure 6.3.

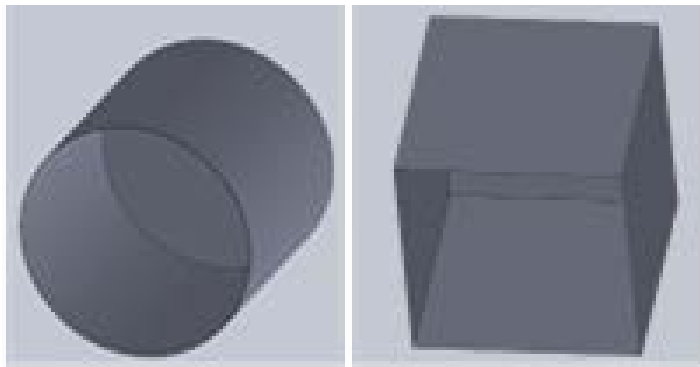


Figure 6.2: CAD models of circular and rectangular shielding

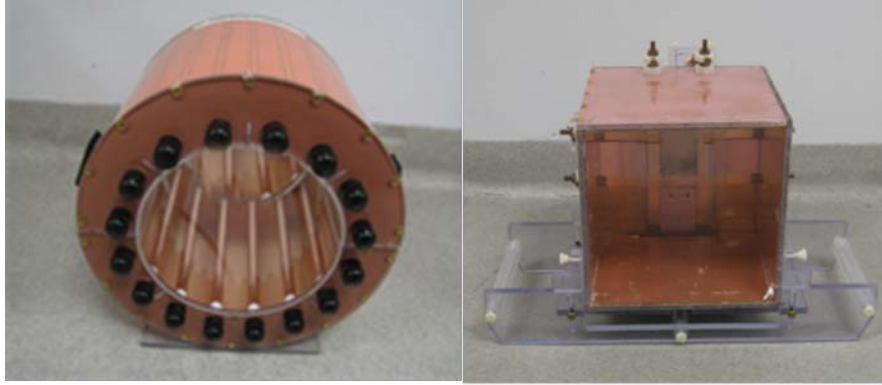


Figure 6.3 Built TEM coil and TTT coil

6.2.3 Full Wave RF Field Simulations (FDTD)

Effective RF shielding should provide efficient decoupling between the RF coil and the gradient coil without degrading the RF coils' performance (157). In other words, properly designed RF coil shielding should be transparent to low time-varying MR gradient fields and accommodating/supporting for high frequency RF fields. Therefore, the goal of the study is to maintain the characteristics of 7T RF coils (B_1^+ field distribution, B_1^+ intensity, E field distribution, and E field intensity) while reducing the induced low frequency eddy currents. An in-house Finite-difference time-domain (FDTD) package with an accurate transmission-line feed model mechanism is implemented to model the RF performance of the TTT coil (176). The RF magnetic field inside this four-channel TTT transceiver coil is modeled. The Discrete Fourier Transform (DFT) method is applied in order to calculate the RF currents (densities and directions) on the coil shielding at 297 MHz (7T MRI). The RF currents on the coil shielding are examined for multiple types of RF excitations (varying phases and amplitudes) resembling RF/ B_1^+ shimming on a PTX system.

6.2.4 RF Testing and 7T Experiments

The gradient field simulation is verified on the 7T Siemens whole body scanner using the gradient field raw data measured inside a spherical oil phantom (diameter = 165 mm). To measure the gradient fields, a pair of trapezoidal gradients is applied multiple times at different slice locations (23,172). The gradient amplitude is ± 2.0 mT/m, gradient slew rate is 40.0 mT/m/ms and pulse duration is 2.5 ms. Slots of the shielding and multiple thin copper layers are tested. S matrix measurements, B_1^+ maps and EPI sequences with the phantom and *in-vivo* human subjects are performed to verify the effectiveness of the proposed dual optimization. For EPI acquisition, the image resolution is 64 by 64; bandwidth per pixel is 2442 Hz/Px; TE and TR are 20 ms and 2000 ms respectively.

For the shielding comparison study, A model-based eddy current correction method (177) is applied to correct the eddy current for the two coils. The desired RF pulse excited pattern should be a smooth rectangle with FOV of 200mm x 200mm. The PTX acceleration factor, R, is 2 for both cases. Human BOLD image slices are also obtained.

6.3 RESULTS

6.3.1 Eddy Current Simulation Verification and Z Gradient Field Behavior along the Magnet Axis

The simulated Z gradient field in the time domain is displayed in Figure 6.4(a2). The ideal gradient strength and gradient strength associated with the presence of the TTT coil structure were compared at different positions along the Z direction (positive direction is defined towards the top panel of the RF coil). The isocenter was labeled as the center of the coil structure. The ideal gradient ramp up time is 50 μs . The results show that simulated Gz is deviating from the ideal Gz (0 to $\sim 200 \mu\text{s}$) due to eddy currents induced on the RF coil shielding. After $\sim 200 \mu\text{s}$, the simulated Gz becomes stabilized and equals to the ideal Gz. Figure 6.4(a1) shows the measured gradient waveform. The effective ramp up time of the measured gradient trajectories with the shielding is shown to be $\sim 200 \mu\text{s}$ in agreement with the simulation results. Similar to the simulation results, the experimental results also demonstrate that eddy current distortion is non-linear and asymmetric along the Z direction.

To further study the eddy currents along the magnet axis, the simulated information was used to obtain the pulse response function $H(t, z)$ the by equations (6-1) and (6-2). The results show that $H(t, z)$ has different characteristics at positive and negative positions due to the RF coil top panel. Figure 6.4(b1) demonstrates that $H(t, z)$ is not linear with respect to Z. The eddy current effects are more prevalent in the positive 60 mm position than the negative 60 mm position as shown in Figure 6.4(b2): $H(t, z)$ is (-80, -13, 0) at -60 mm and (133, 55, 15) at 60 mm, at 0 μs , 60 μs and 120 μs respectively.

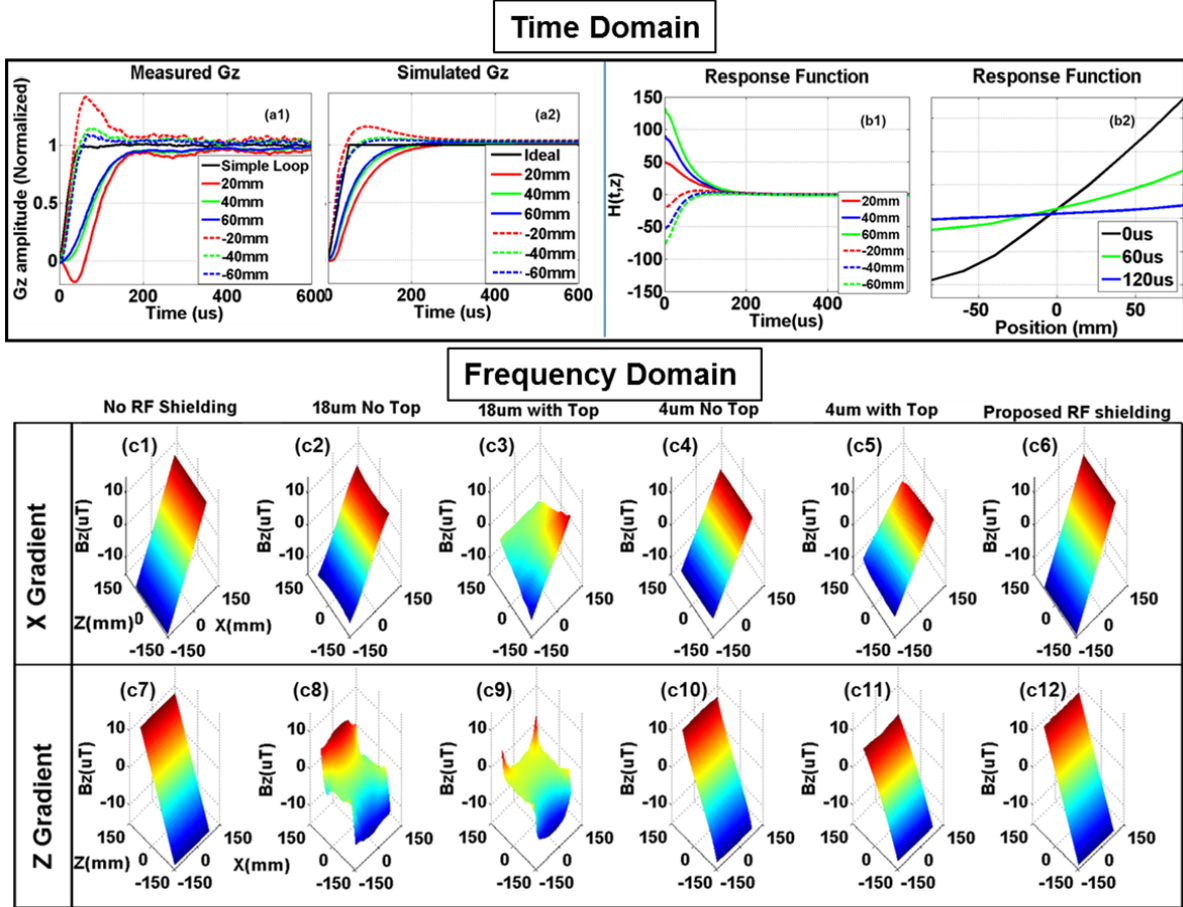


Figure 6.4: Time domain and frequency domain eddy current results.

(a1) Normalized measured gradient field G_z at different positions along the Z direction. The curve for the “Simple Loop” was obtained using a simple RF loop-array coil without any RF shielding (used to represent the ideal gradient field in the measurements). (a2) Normalized simulated gradient field G_z at different positions along the Z direction. The “Ideal” G_z is calculated when the TTT coil structure is not present. (b1-b2) Eddy current pulse response function “ $H(t,z)$ ” as a function of time and position (obtained by (6-1) and (6-2).) Frequency domain: Six different cases have been used to study the top panel and copper thickness influence for X-gradient and Z-gradient fields. Positive “ Z ” positions are towards the top panel. Simulated gradient field distribution at the $Y=0$ plane are shown for 6 cases: 1) distribution with no RF copper shielding 2) distribution with intact 4 sides 18 μm and no top copper shielding 3) distribution with intact 5 sides 18 μm copper shielding 4) distribution with intact 4 sides 4 μm and no top copper shielding 5) distribution with intact 5 sides 4 μm copper shielding and 6) distribution with 5 sides 4 μm copper shielding that includes the

proposed slots. (c1-c6) X-gradient field distributions at 10KHz and (c7-c12) Z-gradient field distributions at 10KHz.

6.3.2 Comparison of Rectangular and Circular Shielding

Figure 6.5 displays the gradient field distribution when there is no coil shielding (A), circular shielding (B), and rectangular shielding (C) (the dark dash lines represent position of the coil shielding.) The gradient field is linear along the B_0 direction when there is no shielding, while it becomes non-linear when there is RF coil shielding. The results show that the distortion is more severe for the circular shielding than rectangular shielding while the excitation current flowing in the gradient coil is the same. Figure 6.6 shows an experimental 7T Tx-SENSE excitation pattern in a head-sized phantom of uncorrected and corrected RF pulses for circular shielding (A and C) and rectangular shielding (B and D). Agreeing with Figure 6.5, the eddy current distortion caused by circular shielding is more severe when compared to rectangular shielding caused distortion, which agree with the simulation. Moreover, the model-based eddy current correction method is ineffective in correcting the circular shielding induced eddy current.

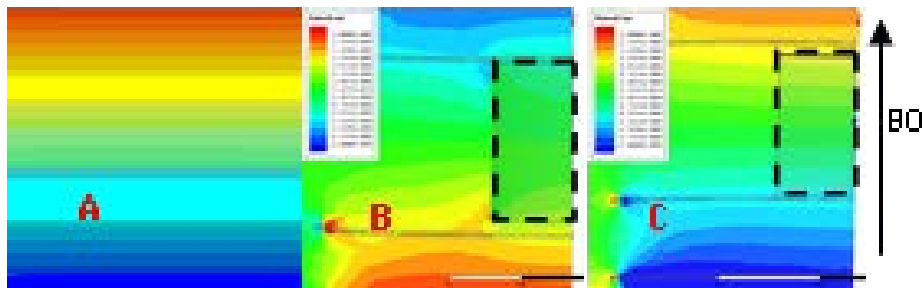


Figure 6.5: Gradient field distribution (simulations)

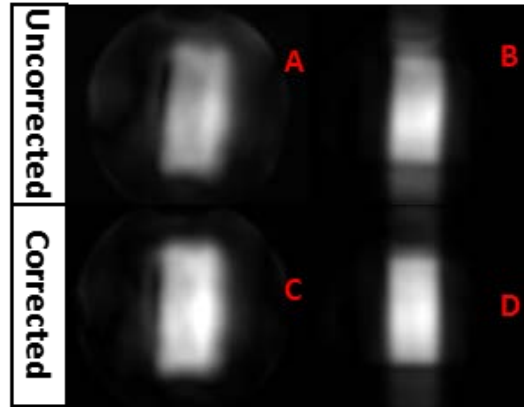


Figure 6.6: 7T Tx-SENSE excitation pattern for circular & rectangular coil shielding.

The ddy-current-generated gradient field (Figure 6.7) was measured at different positions along the B_0 direction for the two coils. Because of the cap copper shielding, the field distortion is not symmetric above and below the iso-center. The eddy current induced distortion decayed with time. Notice that the gradient field is oscillating around stabilized value until $\sim 1200\mu s$ for the circular shielding. This oscillation made the decay period much longer and produced larger field offset than the rectangular one. Therefore it induced more distortion of the gradient field. It also could make the model-based eddy current fitting pathway more intricate.

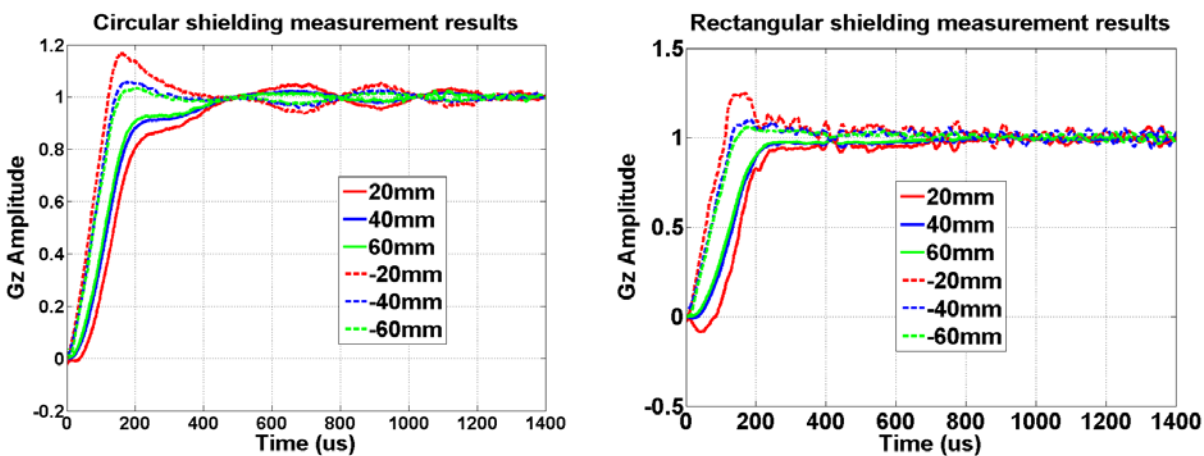


Figure 6.7 : Measurements of gradient field intensities at 7T.

7T human BOLD images are shown in Figure 6.8. While eddy current artifacts are apparent in both cases, the distortion is significantly higher with the circular shielding (A) than with the rectangular one (B).

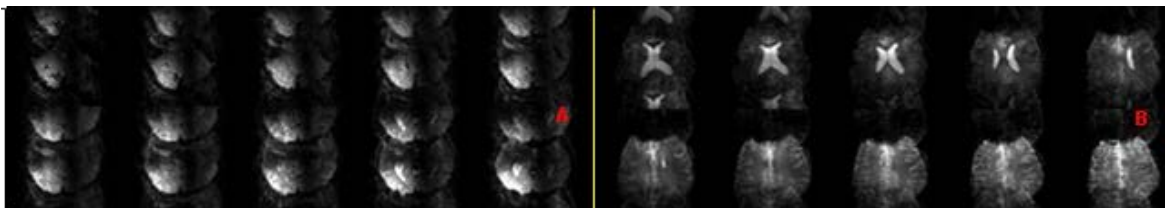


Figure 6.8: 7T *In-vivo* BOLD images

6.3.3 Effects of Thickness of Copper Layers and the Top Panel

Thin copper shielding could be applied to improve the transparency to the gradient fields. The skin depth of copper at 297 MHz is about 4 μm and 4 μm copper is also the thinnest copper we have found available in the market. We tested single 4 μm and double 4 μm (2x4 μm) copper shielding (Polyflon Company, Norwalk, CT, USA.) For the double layer copper shielding, the dielectric substrate between the two copper layers is 0.010" (0.25 mm) PTFE.

In order to compare the effects of 4 μm and a thicker (18 μm) copper shielding, simulation studies were performed. Figure 6.4(c1-c12) display the X and Z-gradient fields inside the RF coil at the Y=0 plane. When there was no RF shielding, the field was spatially linear along the X and Z directions for the X and Z gradient coils respectively (Figure 6.4(c1) and (c7).) When the 18 μm and 4 μm copper shielding were present, the field was distorted (Figure 6.4(c2), (c4), (c8) and (c10).) In general, X-gradient fields induced less distortion than Z-gradient fields. Although the 4 μm copper sheets generated much less eddy current distortions than 18 μm copper, there were still observable residual distortions near the top panel (Figure

6.4(c3), (c5), (c9) and (c11).) Simulation studies (not shown) also demonstrate that the field distortion is more severe at higher gradient field frequencies.

The 4 μm intact (no slots) copper shielding panels are shown in Figure 6.9(a1-a2). They are square shaped and the length of the copper panel is approximately 23 cm. The EPI images (Figure 6.9(b1)-3(b2)) were acquired to show the image distortions generated by the eddy currents when all 5 copper panels are present. In every subfigure, there are 11 slices shown at adjacent positions along the B_0 direction (one slice in one red frame box is used to point out the relative position within the EPI images.)

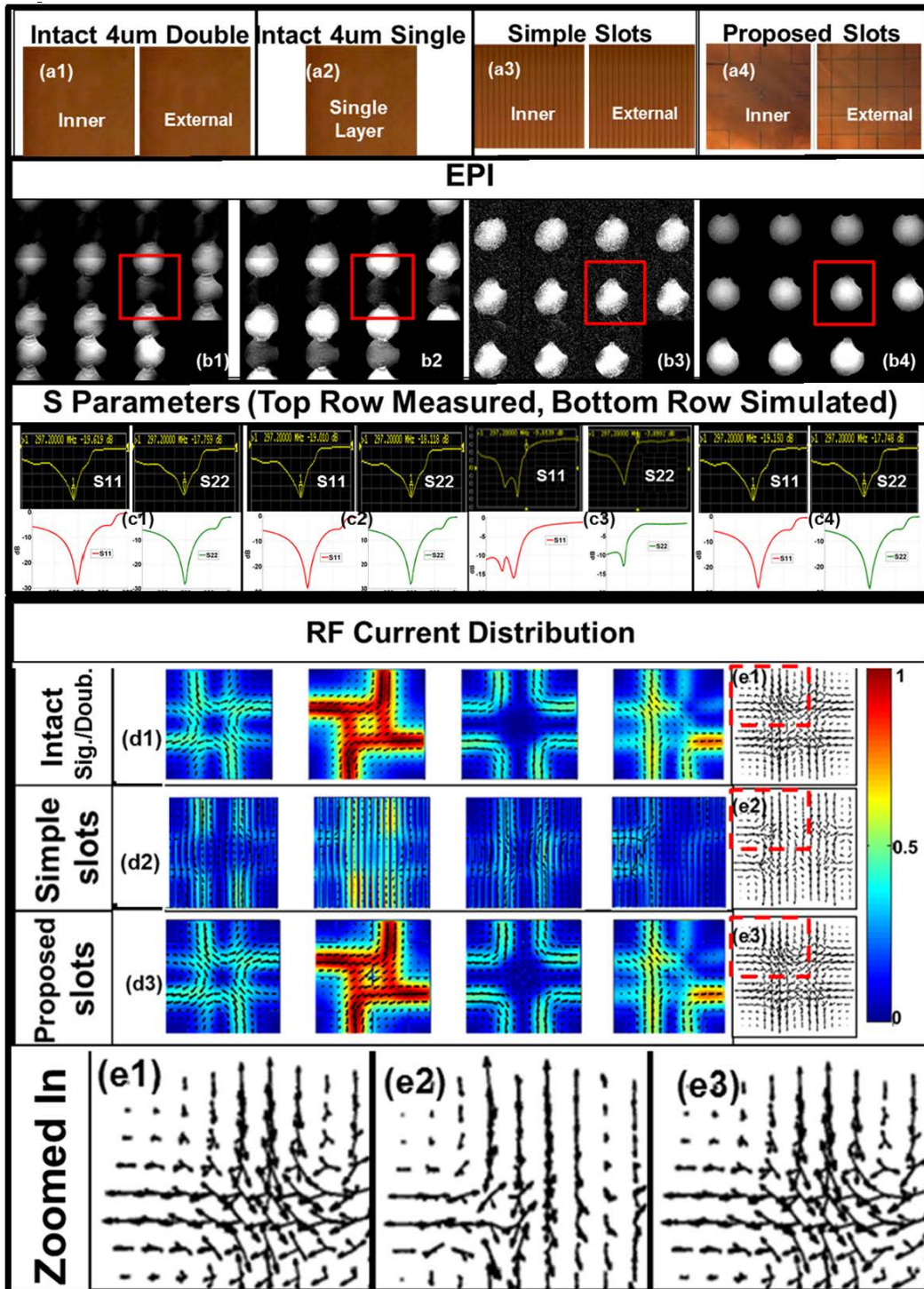


Figure 6.9: Four different copper shielding comparisons.

(a1) intact double 4 μm ($2 \times 4 \mu\text{m}$) copper shielding, (a2) intact single 4 μm copper shielding, (a3) 18 longitudinal slots in the double 4 μm ($2 \times 4 \mu\text{m}$) copper shielding and (a4) proposed copper slots in the double 4 μm ($2 \times 4 \mu\text{m}$) copper shielding. The inner copper layer slots are based on the RF current distribution

patterns and external copper layer slots are based on the eddy current simulations. (b1-b4) represents 11 slices of EPI images for the above-mentioned 4 copper shielding. (c1-c4) Reflection coefficients (measured and simulated using FDTD) for the transmit coil with the above-mentioned 4 copper shielding. (d1-d3) RF currents on the copper shielding with four different excitation modes (uniform phase, quadrature, 180° phase shift between adjacent channels and one arbitrary set of 4 phases). The RF current distribution maps are presented at 297 MHz; plotted on the top of the density maps are the instantaneous current vectors. (e1-e3) Overlaid instantaneous RF current vectors of the four different excitation modes. The current vectors inside the red dashed box are zoomed in to show the vector patterns. (d1) and (e1) are for intact 4 μm single/double layer copper shielding, (d2) and (e2) are for the simple slots and (d3) and (e3) are for the proposed copper slots.

6.3.4 Effects of Simple-Structured Slots

Simple-structured slots along the axial direction were shown to be an effective way to reduce the eddy current effects (157). Simulation studies demonstrate that:

1) slots along the gradient field's changing direction are effective in reducing eddy current artifacts. As the X-gradient coil and Z-gradient coil generated fields are changing along the X direction and the Z direction, respectively, the slots should be cut along the X and Z direction respectively;

2) three slots on each of the 4- μm shielding panels considerably suppress the eddy currents at 10 kHz. Since the distortion from the eddy currents is a function of the thickness of the copper sheets and the frequency of the gradient fields, more copper slots will be needed at higher frequencies and with thicker copper shielding: e.g., for 18 μm single copper, five slots can get similar suppression of the generated eddy currents; and

3) slots orthogonal to the gradient field changing direction don't reduce eddy currents.

The simple-structured slots have been physically applied to the double $4\ \mu\text{m}$ ($2 \times 4\ \mu\text{m}$) copper shielding and 18 slots were etched on both sides of the copper shielding Figure 6.9(a3). The slots were staggered at both sides in order to minimize RF field leakage through the gap. EPI images (Figure 6.9(b3)) show the eddy current suppression was achieved, while the signal to noise (SNR) is very low. S parameters were measured to study the coil performance with different copper shielding. Figure 6.9(c1-c2) represent the network analyzer measured and FDTD simulated reflection coefficients with the intact $4\ \mu\text{m}$ copper shielding. All reflection coefficients (S_{xx}) of the four ports are less than -18 dB. Figure 6.9(c3) shows the reflection coefficients (simulated and measured) for the simple-structured slot panel. For the pair of coil elements along the direction of the slots, the reflection coefficient (S_{11}) is significantly different from the pair of coil elements orthogonal to the slots (S_{22}); yet all the coil elements are detuned. The results also show that the coupling of the coil elements along the direction of the slots is -4.97 dB while the other two elements coupled by -14.7 dB. The coil cannot be re-tuned with this arrangement.

6.3.5 Dual Optimization Approach

Figure 6.9(d1) and (e1) display the FDTD calculated RF current distribution associated with four different excitation modes. Figure 6.9(e1) displays overlaid RF current vectors for four excitation modes. The results show that with different transmit excitation modes (as used in PTX applications), the current densities and distribution patterns can be substantially different. Especially in the center areas, the current directions are substantially spatially changing with different types of excitations (as shown in the zoomed subfigures.) While the current distributions and current vectors are different for various excitation mechanisms, several

locations on the shielding panels sustain minimal RF current densities (this was observed throughout all the modes and useful RF shimming patterns excited with the 2x2 TTT coil.) Based on these findings, the double 4 μm (2x4 μm) copper shielding were etched into different slotting patterns that are shown in Figure 6.9(a4). The inner side of the top panel is slotted at regions where there is relatively lower RF current density in order to maintain the main RF current pathways. The external copper layers' (facing the magnet) cuts (designed exclusively based on eddy current simulations) are used to reduce the eddy currents.

The low frequency eddy current simulations were then performed and verified that the induced eddy current was significantly reduced with the proposed slots which are shown for X-gradient coil in Figure 6.4(c6) and Z-gradient coil in Figure 6.4(c12). For the RF characteristics, Figure 6.9(c4) demonstrates that the proposed slot patterns maintain the tuning and the matching of the RF coil as when intact shielding is utilized. From the EPI images in Figure 6.9(b4), the proposed slots in the double 4 μm (2x4 μm) copper shielding are highly effective in almost negating all of the eddy current artifacts and maintaining the RF characteristics of the RF coil. The SNR and B_1^+ maps have been measured to compare RF signal intensity/distribution changes with different shielding thickness and patterns applied. When compared to the intact double-layered shielding, over all the slices, the SNR and B_1^+ distribution changes per slice are less than 5% when the proposed slot pattern is applied.

Figure 6.9(d3) and Figure 6.9(e3) show the RF current distribution and current vectors were comparable with that of the intact copper, while Figure 6.9(d2) and Figure 6.9(e2) show the RF currents were significantly distorted by the simple slots.

6.3.6 *In-Vivo* Demonstration

Healthy human subject studies were conducted, with signed consent forms approved by the Institutional Review Board at the University of Pittsburgh. *In-vivo* images acquired using the 4 element Tx/Rx coil with the proposed double 4 μm layer copper shielding and the 18 μm copper shielding are shown in Figure 6.10(a) and (b) respectively. In every image, there are 22 slices covering the whole human head. Because of eddy current artifacts, brain images are overlapped in almost every slice in the 18 μm copper case Figure 6.10(b). In the proposed slotted copper case Figure 6.10(a), images are intact (except near the absolute top of the human head.)

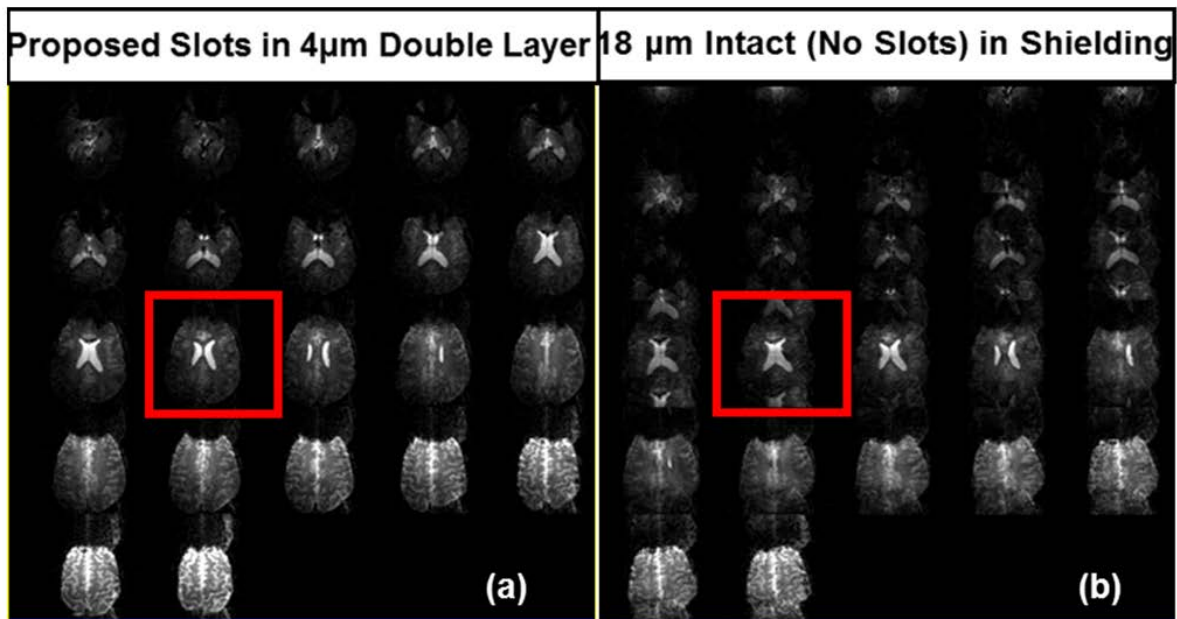


Figure 6.10: *In-vivo* EPI images (22 slices to cover the whole brain) with (a) the proposed slots in double 4 μm (2x4 μm) copper shielding and with (b) 18 μm intact/no-slots copper shielding

6.4 DISCUSSION

Thin copper shielding was shown to improve the transparency to the gradient fields (137). However, the EPI images were distorted by artifacts even when the thin copper is used (4 μm single-layer which is the skin-depth of copper at 297 MHz and double-layered thin copper shielding) as demonstrated by Figure 6.4 and Figure 6.9(b1-b2). Furthermore, simple-structured slots in double layer copper shielding have also been used to reduce gradient field-induced eddy currents (24,29). However as shown from our results, the suppressed eddy current distortion was achieved while significantly altering the coil RF characteristics (tuning, matching, coupling and RF current distribution/intensity on the coil shielding, and consequentially changes in the B_1^+ distribution/intensity and etc.).

When using simple slots in the double layer copper shielding, the shield can be considered as a number of capacitors in parallel. The capacitance is proportional to the overlapping copper area and the thickness of the dielectric substrate in between. With the thin dielectric substrate in this study, the double layer copper with staggered slots should represent a thicker continuous conductor at 297MHz. Therefore the low SNR (Figure 6.9(b3)) was not necessarily caused by RF radiation/leaking. The changes in the coil's S parameters (Figure 6.9(c3)) and RF current distributions/densities on the coil's shielding (Figure 6.9(d2) and Figure 6.9(e2)) show that the simple slots altered the RF coil's characteristics resulting in SNR reduction.

Figure 6.11 shows the ghosting quantitative comparisons between five different copper shielding patterns proposed and tested in this study, using the data measured from the phantom EPI images. The curves are the ratio between the background intensity (including noise and ghosting) and the image signal intensity. It shows less ghosting induced by the 4 μm single and

double-sided copper shielding when compared to the 18 μ m solid copper, through most of the slices. There is minimal eddy current induced ghosting in images associated with the simple-structured slots (Figure 6.9(b3)). However, the RF coil performance was deteriorated and Figure 6.10 shows that the background to signal intensity ratio is almost 50%. As a result and for the presented configuration, the use of thin copper layers and/or simple-structured slots for RF shielding was not effective in reducing the gradient field-induced low frequency eddy currents while maintaining the RF characteristics for this RF coil.

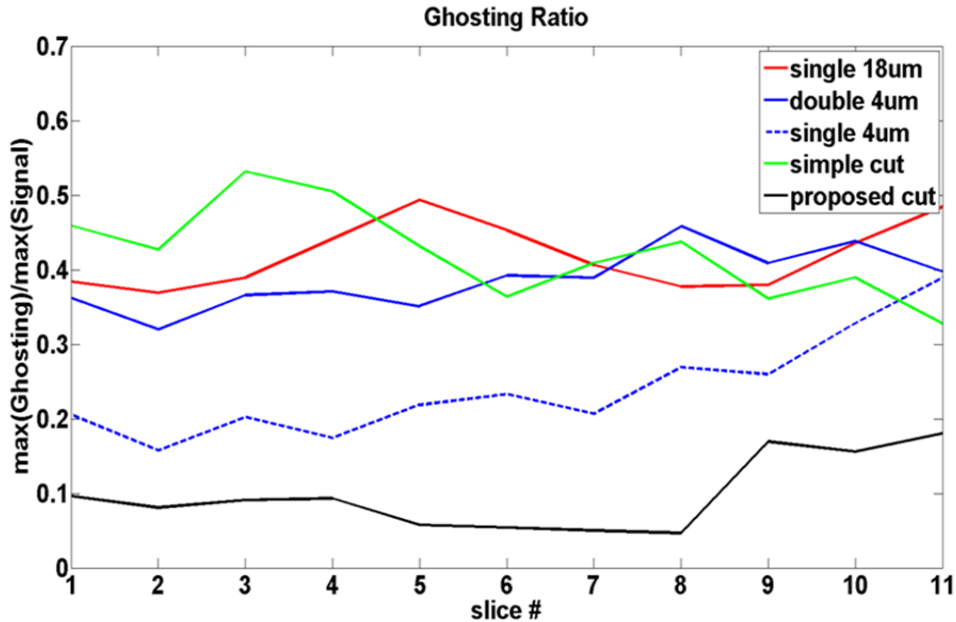


Figure 6.11: Ghosting ratio comparisons (measured with EPI scans) between 5 tested/discussed copper shielding methods.

Some eddy current artifacts are present towards the top of the brain, shown in Figure 6.10(a) and Figure 6.11 curve for the proposed cut case. This can be caused by the copper on the Tx/Rx coil elements (copper struts) and on the small side panels which that are covered by 18 μ m copper sheets in the original coil design. These copper sheets can also generate eddy

currents. Hence, the 18 μm copper sheets on the copper struts have been replaced by the thinner (9 μm) copper layers. And in order to provide a better and more realistic brain imaging illustration, an RF coil system composed of 5 sets of the 2x2 Tic-Tac-Toe transmit coil (total of 20 Tx channels) in conjunction with 32-ch receive coil insert was used. The copper shielding of the large panels of this 20 element transmit coil is similar to the tested 4 element Tx/Rx coil. However this RF coil system contains 1) 16 additional transmit elements with their 4 sets of small side panels in order to provide better transmit fields and 2) receive coil insert in order to provide better SNR. The *in-vivo* EPI images are shown in Figure 6.12(a) (the image resolution= 96 by 96; bandwidth per pixel = 1680 Hz/Px; TE and TR = 24 ms and 2000 ms, respectively.) In order to display the background artifacts clearly, the intensity of 5 EPI image slices (showing the top of the head) was scaled by 10 times in Figure 6.12(b) to show the noise and eddy current ghosting distortion. Figure 6.12 shows that the ratio between the background intensity (including noise and ghosting) and the image signal intensity is less than 10%. Figure 6.4 - Figure 6.12 demonstrate the effectiveness of the proposed slotting method in reducing eddy current artifacts. In our experience, the eddy current artifacts of this modified proposed slotted coil are comparable to other commercial non-shielded 7T RF coils.

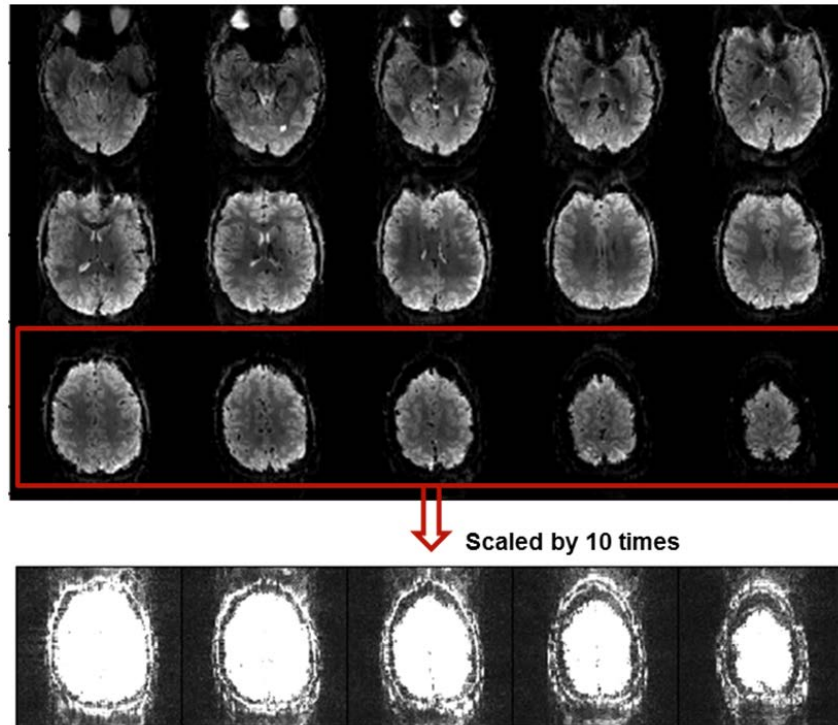


Figure 6.12: *In-vivo* EPI images with the modified slots in the double 4 μm (2x4 μm) copper shielding using the 20-ch Tx coil with 32-ch Rx insert.

In summary, five different types of copper shielding were tested and discussed in this study: single 18 μm (half oz) copper sheet, single 4 μm (0.114 oz) copper sheet, double 4 μm (2x4 μm) copper sheet, double 4 μm (2x4 μm) copper with simple-structured slots and double 4 μm (2x4 μm) copper with a proposed (based on RF and quasi-static field simulations) slot pattern specific to the RF coil (Tic-Tac-Toe transmit array) used. The eddy current simulations were verified by experimental data.

The results demonstrate that eddy currents induced on RF coil copper shielding can significantly distort the linear gradient fields. Although thinner copper shielding generated less (yet still considerable) distortion, the distortions due to the top (cap) copper shielding were significant. Simple slots along the gradient field changing direction are verified to be an

effective way to reduce the eddy current effects. However, simple-structured slots significantly altered the coil's RF characteristics (tuning, matching, coupling and RF current distribution/density on the coil shielding and consequentially transmit field intensity and distribution). This is critical when RF shielding is an essential (not just for the purpose of reduction of radiation) part of the coil performance as in the case of many high field transmit arrays.

The circular RF copper shielding induced more low frequency eddy currents than rectangular shielding. The long term oscillating gradient field in the circular shielding produces larger field distortion than the rectangular shielding. This could be explained by using circuit theory that high impedance occurs at corner circuits. This high impedance blocks low frequency eddy currents for rectangular shielding.

Normally the golden rule used to sustain the RF performance is maintaining the RF current paths. However the RF current distribution as well as current direction could be different for different excitations modes, especially when a PTX system is used. In this work, using the proposed dual optimization method that combines both RF and quasi-static field simulations, the shield areas where there is minimal RF current density were distinctively slotted to maintain the main RF current density pathways. EPI images, GRE images, B_1^+ maps and network analyzer measurements verified that the proposed (based on RF and quasi-static field simulations) slot pattern in the double 4 μm (2x4 μm) copper sheet can sufficiently suppress the eddy current artifacts while maintaining RF characteristics of the utilized RF transmit array. This integrated, RF and quasi-static, field simulation approach can be utilized in designing RF coil shielding.

7.0 CONCLUSIONS AND FUTURE WORK

7.1 SUMMARY AND FINDINGS

In this dissertation, RF methods have been applied to design implanted miniature antennas inside the human brain to transmit power wirelessly for implanted Brain Computer Interfaces. The results show that thin (on the order of 100 micrometers thickness) biocompatible insulating layers can significantly impact the antenna performance. The proper selection of the dielectric properties of the biocompatible insulating layers and the implantation position inside the human brain tissues can facilitate efficient RF power reception by the implanted antenna. While the results show that the effects of the human head shape on implanted antenna performance is somewhat negligible, the constitutive properties of the brain tissues surrounding the implanted antenna can significantly impact the electrical characteristics (input impedance, and operational frequency) of the implanted antenna. Three miniaturized antenna designs are simulated and they demonstrate that maximum RF power of up to 1.8 milli-Watts can be received at 2 GHz when the antenna is implanted around the dura, without violating the Specific Absorption Rate (SAR) limits.

A new 20-channel transmit array has been evaluated and optimized for 7 Tesla MRI neuron imaging applications. Eigenmode arrangement of the 20-ch coil allows controlling RF excitation not only at the XY plane but also along the Z direction; the modes of each group/level

can be excited simultaneously. Optimized results presented show the eigenmode could be optimized and generate a uniform 3D B_1^+ excitation. The fields were also compared with an 8-ch TEM coil. Based on the array structure, new excitation paradigms are presented to generate uniform 3D magnetic excitation fields (B_1^+). The optimization results have been verified by *in-vivo* experiments with different scanning sequences on a Siemens 7T MRI human whole body scanner equipped with 8 parallel transmit channels. High quality whole brain (including cerebellum) MPRAGE and Turbo-Spin-Echo images were acquired successfully.

The eddy current simulation method is verified by the measurement results. Eddy currents induced by solid/intact and simple-structured slotted RF shielding can significantly distort the gradient fields. EPI images, B_1^+ maps and S matrix measurements verified that the proposed slot pattern can suppress the eddy currents while maintaining the RF characteristics of the transmit coil. The presented dual-optimization method could be used to design the RF shielding and reduce the gradient field-induced eddy currents while maintaining the RF characteristics of the transmit coil.

7.2 CONTRIBUTION OF THIS DISSERTATION

7.2.1 Non 50 Ohm Antenna and SAR Regulation Considerations

Recent research reveals that the optimal frequency for the millimeter sized implantable antennas is above 1 GHz; the electromagnetic field penetration depth can be asymptotically independent of frequency at such high frequencies (77,178). Furthermore, an implantable antenna operating above 1 GHz could be designed into a very small profile; these small sizes antennas could be

more bio-tissue compatible. Therefore, an implantable antenna (above 1 GHz) provides a promising approach to accomplish the longevity of implantation of BCI in users as well as transmitting power effectively.

There are some groups studying implantable antennas to transmit data wirelessly into the human body. Most of these implantable antennas have been designed to operate at the medical implant communication service (MICS) band of 402-405 MHz. The implantable small profile (about 30 mm length and 40 mm width) microstrip antennas' resonance characteristics and their radiation were evaluated (36). The transmission and reflection of microstrip antennas affected by different superstrates and substrates were studied (72), through numerical analysis and measurement. The effects of different inner insulating layers and external insulating layers and power loss were discussed (73) analytically, using a spherical model. The radiation efficiency impacts of insulating layers were also presented (74). For GHz and above operating frequencies, the impact of the coating on antenna performance was studied by an implanted antenna radiation measurement setup (75). A pair of microstrip antennas working at microwave frequencies (1.45 and 2.45 GHz) established a data telemetry link for a dual-unit retinal prosthesis (76).

All these referenced papers, whether working in the MICS band or at GHz frequencies, are assuming that the implantable antennas are connected with 50 Ohm transmission lines. It is noted however, 1) the 50 Ohm assumption could limit the antenna geometry and operation frequency; 2) the ratio between received RF power and tissue absorption depends on the input impedance of the receive antenna (77). To realize the optimal antenna performance and conjugate matching (i.e. optimal performance), the antenna loads including connected wires and implanted chips could be designed to other values rather than being restricted to 50 Ohms. Additionally, the available transmitted power into the human brain has not been studied

thoroughly under SAR regulation studies in these referenced papers. In this study, the maximum received power under the SAR regulations will be calculated based on the FDTD simulation results for different antenna structure designs.

7.2.2 A New RF coil Mode Excitation Paradigm

In order to generate a homogenous B_1^+ field, various methods have been explored. The parallel RF excitation approach uses a spatially tailored RF pulse design and has generated satisfactory results (179). However, it requires extra time to measure B_1^+ maps for each transmit channel; it is sensitive to the B_0 field shimming quality and gradient field performance(126). RF shimming is another widely used method. Mao's paper discussed the limits of this method for high field MRI of the human head, while there was no safety consideration (180) and signal efficiency consideration included.

Time-Interleaved Acquisition of Modes (TIAMO) combines only two different excitations, but the contrast in the final image is expected to deviate since the excitation field is nonuniform in each of the individual modes (126). The cylindrical coil produces homogeneity by driving a traveling wave from one end and absorbing at the other, however, the resistive termination makes the coil extremely inefficient (181). In conclusion, none of the presented methods has yet been accepted and used for clinical application and a new coil excitation paradigm design and optimization method needs to be investigated.

The TTT coil (182) is a highly coupled (between struts) and decoupled (between sides) coil. Since the signal from one strut is coupled to another strut, the coil's performance will not be changed significantly by the load (phantom or coil). Since the load sensitivity of the TTT RF coil is robust, the optimization results could be extended for all patient scans without patient-

specific simulations. The modes of the RF coil are the linear independent current distribution solutions of coil's circuit equations (183). Some mode (uniform mode) was used to generate a very uniform transverse magnetic field inside the coil for lower field MRI, for example, mode 1 of the high-pass birdcage coils at 1.5T (183). Some other mode (gradient mode) was used to increase the SNR in the temporal lobes, occipital lobes and cerebellum (127). There are also papers suggesting the use of two modes to increase the homogeneity of the image (126). However, it is not easy to excite several modes of the coil simultaneously (184) and modify modes freely; normally it needs the assistance of extra circuitry (e.g. Butler Matrix). The TTT coil could easily excite different modes with combinations of different coil elements. The 20 channels provide the control ability not only at the XY plane but also in the Z direction. The optimization methods could be used to find a uniform excitation pattern by manipulating the amplitude and phase of each of the excitation modes under certain constraints. There are many different solutions for the RF excitation that achieve a very similar fidelity to the targeted excitation pattern. A solution with the minimized local SAR and best efficiency can be selected and used for a specific clinical application.

7.2.3 New Eddy Currents Calculation and Shielding Slot Methods

RF copper shielding induced eddy currents can be very problematic. There are patents and papers discussing the shielding slot method to reduce eddy currents (153,154). Less reported is the quantitative eddy current study. Analytically, eddy currents are notoriously difficult to calculate. In objective 3, the eddy current field is numerically calculated. Successful MRI field experiment validation is delivered. Eddy current characterization is studied based on eddy current response function. Effective RF coil shielding slot design was reported (185,186) in

order to reduce eddy currents, for example, the multiple thin copper layers were discussed and their performance could ideally be transparent for the MR gradient fields and could efficiently block the high frequency electromagnetic emission (137). These methods only work for coil structures where the RF shielding is not a component of the coil. This work studies a new and an elaborate dual-optimization method that maintains the RF characteristics of the RF-coil and simultaneously reduces low frequency magnetic field distortions created by eddy currents. The optimization is guided by full wave electromagnetic simulation combined with eddy current simulation. The designs are tested on a 7T human scanner using phantoms and *in-vivo* subjects.

7.3 FUTURE WORKS

7.3.1 Implanted Antenna Designed for Wireless Power Transmission

In this work, the input impedance of the antenna has been verified by the measurements of a monopole antenna in the air; the power transmission inside a lossy material has been discussed by analytical methods. In the next step, performance of antennas with bio-compatible materials and inside the human tissue lossy environment should be measured. This can be done with the recently developed eight-component detailed human head phantom in our lab. The designed antenna system (transmit and receive circuitry with implanted chips and electrode array) could be measured inside this human head phantom to study the antenna power transmission efficiency and to calculate the needed number of antenna arrays.

7.3.2 RF Coil Designed for 7 Tesla MRI

The designed innovative RF coil and new eigenmodes excitation method (along the Z direction) could generate high efficient, high uniformity and low power absorption 3D excitation pattern. It will be a powerful tool for brain studies at 7 Tesla; it has been tested and provided high quality 3D MPRAGE, SWI, fMRI and etc. It could benefit many clinical studies. Therefore, in the next steps, new 7 Tesla MRI clinical applications should be investigated. Furthermore, most DTI imaging is done at 3 Tesla, since it requires high B_0 field uniformity (which gets much worse at 7 Tesla MRI). How to generate uniform B_0 or to get rid of the influence could also be a very interesting topic. Last but not least, the coil design and excitation strategy will also be very useful for body coil, breast coil, knee coil and other RF coil designs for ultrahigh MRI applications.

APPENDIX A

MRI GUIDED MAGNETIC NANOPARTICLE BASED DRUG DELIVERY FOR NEURODEGENERATIVE DISEASES- PRELIMINARY *IN-VIVO* AND *IN-VITRO* DATA

This work relates to audiences who are interested in drug delivery research and development for Neurodegenerative Diseases by using MRI technology or ultrahigh field MRI.

Purpose:

To develop a new magnetic nanoparticle (MNP) based drug release system and to study the feasibility of MRI fields triggering MNP drug release *in-vitro* and *in-vivo* in the region of central the nervous system.

Introduction:

Neurodegenerative diseases are generally not well-understood and there are no effective drugs available to treat and prevent these diseases. Oxidative markers and damaged cell components were observed in neurodegenerative patients (187). Magnetic sensitive silica nano-spheres were used to control drug release (188). A potent antioxidant compound could be incorporated in magnetic nanoparticles and delivered into the central nervous systems (CNS) tissue for lowering oxidative stress related to numerous neurodegenerative diseases. In this study, the feasibility of

using MRI fields to trigger the drug loaded MNPs is investigated. *In-vitro* and *in-vivo* results are provided.

Experiments:

Silica magnetic nanoparticles were synthesized. Fluorescent compound was loaded to represent the drug release. All the experiments were done with a 7T MRI (Germany, Siemens). The effects of high intensity static magnetic fields on the stability of the particles were measured. An Echo Planar Imaging (EPI) sequence was used to generate the proper gradient field frequency to stimulate the drug release from designed dialysis sample tubes. The release of fluorescein *in-vitro* was measured using a spectrum meter. For the pilot study, magnetic nanoparticles loaded with fluorescein were also injected into the brain of a rat. The rat was exposed to the gradient field stimulation and then tissue slices were examined for fluorescein released with brightfield and fluorescence microscopy. Magnetic nanoparticles were also injected into the rat brain without MRI stimulation exposure as the control.

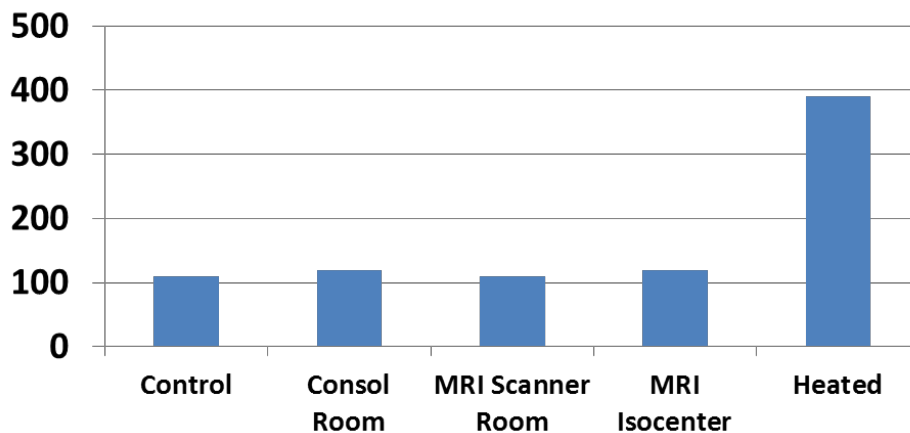


Figure A.1: Stability of MNP in the magnetic field

Results and Discussion:

The synthesized particles were placed inside the 7T MRI for 1 hour to compare with controlled groups. Figure A. 1 shows that the static field did not increase the drug release from magnetic nanoparticles. MRI scanner room data was used to test the fringe fields. The heated sample (80 °C) was used as a positive control for the release. The EPI sequence was applied with RF amplitude of 0 Volt to make sure any release of the drug from the synthesized particles was caused by the gradient field. The readout is Z gradient field. Figure A.2 shows the major frequency of the applied field is ~ 1.7 kHz and the intensity is about 16mT/m. We placed the sample at a location (80 cm away from the imaging iso-center) where 12 mT gradient fields were generated. For the *in-vitro* experiments, two 10 minute gradient field stimulations were applied at time points of 130 and 170 minute. The release of fluorescein was measured. Figure A.3 shows that after samples reached a plateau during the passive release phase with fluorescein diffusion across the dialysis membrane, constituent fluorescein increase was observed, indicating MRI triggered release.

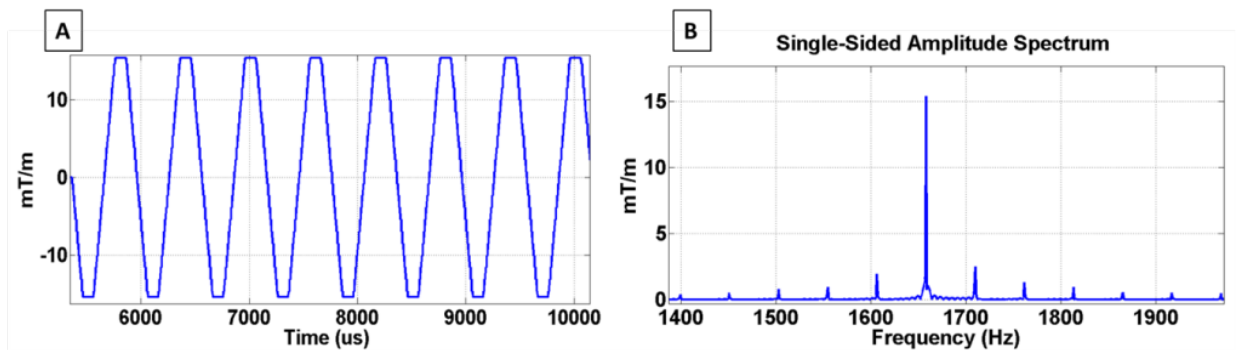


Figure A.2: Gradient fields generated by the applied EPI sequence (a) and Fourier transform of the gradient field (b)

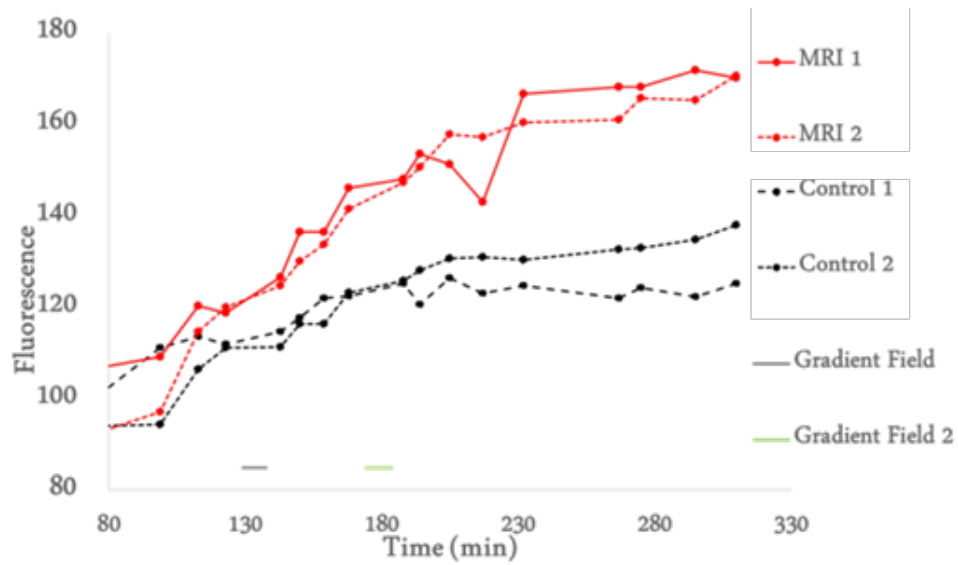


Figure A.3: MRI triggered release from magnetic nanoparticle

In-vivo images are shown in Figure A.4. Magnetic nanoparticles ($10\mu\text{L}, 20\text{mg} / \text{mL}$) were injected 2mm into the rat brain and a 10 minutes stimulation was done with 1.7 kHz and 12 mT gradient fields. The control was just injected but no stimulation was done. The animal was immediately sacrificed. The brain was removed and flash-frozen. Brain slice in Figure A.4 shows a clear increase of fluorescence in tissue surrounding the magnetic nanoparticles.

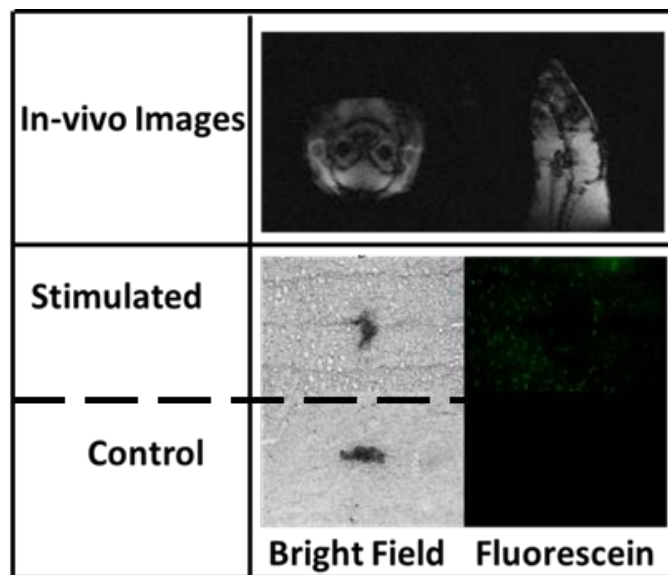


Figure A.4: *In-vivo* MRI triggered fluorescein release

Conclusion:

In-vivo drug release from silica magnetic nanoparticles via MRI stimulation was demonstrated by observing fluorescein release from silica magnetic nanoparticles injected into the brains of rodents.

APPENDIX B

STUDIES IN RF POWER COMMUNICATION, SAR, AND TEMPERATURE ELEVATION IN WIRELESS IMPLANTABLE NEURAL INTERFACES

B.1 INTRODUCTION

Neural interfaces provide a direct functional interface with the brain to monitor or initiate neural activity. The goal for these devices is to provide real-time control signals for prosthetic devices, study brain function, and/or restore sensory information lost as a result of injury or disease (1).

The various classes of neural interfaces can be distinguished by their level of invasiveness (non-invasive and invasive, i.e. intra-cranial) (31). Non-invasive systems primarily record electroencephalograms (EEGs) from the scalp surface to control computer cursors or other devices. The signals provided by EEGs are typically weak, since the signals are transmitted cross different tissue layers and the background noise also reduces the accuracy of the EEG received signals (32). Furthermore, EEG-based techniques provide communication channels of limited capacity (20-30 bits/min) (189), limiting the usefulness for prosthetic devices for real-time control. Two other non-invasive technologies that could be considered as neural interfaces are magnetoencephalography (MEG) and functional magnetic resonance imaging (fMRI) (190). However, both MEG and fMRI technologies require a high field magnetic environment enclosed

in a magnetically shielded room, which greatly increases the cost and severely limits their applications.

The invasive neural interfaces are implanted either on the surface of the brain, or inserted into the cerebral cortex to capture local field potentials and/or action potentials (2-4). The invasive neural interfaces have the potential to provide the spatial and temporal precision required for implementing real-time prosthetic systems. The utility of neural interfaces have been demonstrated by several labs using non-human primates to control robotic arm movements (191-193) and people with tetraplegia to control a robotic arm (5) and a prosthetic limb (6) . The initial results suggest that neural interfaces implanted in the cortex could use spiking activity to restore independence for humans with paralysis (7).

Most invasive neural interfaces use wires for power and data transmission. The wires not only limit the utility of neural interfaces, but also increase the likelihood of device failure and clinical risks (8). Using Radio Frequency (RF) to power and communicate with a neural interface could widely extend the number of applications and increase chronic *in-vivo* viability. There are several advantages to wireless implementation of neural interfaces: 1) the surgical access can be closed, 2) devices could be distributed across the brain, and 3) it minimizes relative motion between the device and tissue by removing tethering forces. However, RF exposure may result in tissue heating, which is regulated by the Food and Drug Administration (FDA), International Electrotechnical Commission (IEC) and Federal Communications Commission (FCC). In order to comply with these standards, accurate heating effects and RF exposure must be estimated. In addition, it is essential to perform an analysis of electromagnetic power deposition throughout the human head to determine the amount of available power to neural interfaces without violating these limits. Hence, this work focuses on the RF power

produced/received by dipole antennas in or on the surface of a human brain and the associated tissue heating. The dipole antenna design was chosen in order to set up a normalized model for future studies.

Power deposition analyses have been performed in the design of transcutaneous transmission coils for powering devices (such as cochlear implants), as well as to simulate the effects of external antennas (e.g. cell phones, magnetic resonance imaging probes, and hyperthermia antennas) placed in close proximity to biological tissue (194,195). Studies have been conducted on the effects of implantable electric devices placed on the retina, cardiac muscle, and other structures within the body (36,196-203). However, none of the above studies examine wireless operation inside the brain.

A miniaturized neuroprosthesis suitable for implantation into the brain was studied by Mojarradi, et al (204), where they measured performance of low power low-noise CMOS preamplifiers. Bashirullah et al (205) provided a brief overview of developments towards the Florida wireless implantable recording electrode micro systems as well. Harrison et al. (68) presents bench and in vivo experimental results from an integrated circuit designed for wireless implantable neural recording applications demonstrating wireless and inductively powered neural recordings from a cat and non-human primate using a single-chip system (INI3 chip) with a minimal number of off-chip components. None of these studies examine tissue heating increases inside the human brain due to the wireless operation.

Kim et al. studied the thermal impact from the operation of the implanted integrated electrode array (UEA) device (206). SAR was measured within a human-head-equivalent phantom during operation of the embedded passive wireless neurorecording microsystem(207) . Nevertheless, SAR and temperature changes due to the RF radiation by the wireless RF

transmitting antenna haven't been investigated. Ibrahim et al. provided an initial estimation of the amount of tissue heating under the SAR limitation with the operation of a wireless neural interface device (208). However, all these calculations were performed in two dimensions (2-D) finite difference time domain (FDTD) method and the peak temperature changes caused by electromagnetic absorption in the head were predicted using the 2-D bio-heat equation. In the 2-D simulation, the simulated head model has to be highly simplified, as well as the structure of the transmit/receive antennas and the integrated implantable chip. Therefore, these models only provide an estimate of heating and SAR. For engineering neural interfaces for human applications, it is critical that we are able to accurately simulate specific 3D antenna structures and chip dimensions. 3-D simulation provides critical data for calculating the transmit power, radiation efficiency and the SAR distributions during device design. The presence of human tissues at high frequencies can affect RF field distribution/intensity/polarization; all of which will impact the allowed power reception under specific SAR guidelines. In conclusion, an elaborate three dimensional (3-D) SAR and temperature study of the implantable neural interface device is needed to accurately model SAR and temperature associated with RF powered neural interface operation.

In this work, we designed a 3-D modeling scheme of the head-neural interface antenna system to study RF power reception and local heating associated with the operation of a wireless implantable neural interface. The dipole antennas were numerically implanted inside of a 19-tissue head model (38,209-212) at different depths. The study was performed with different antenna lengths at different frequencies. Since FDTD method has great advantage when applied to the human body simulation (relative short computational time and small memory requirements), an in-house 3-D FDTD package was used to calculate the SARs, in conjunction

with an accurate excitation/reception algorithm (59). The FDTD model of the implanted antenna was validated by the analytical formulation on a simplified geometry for uniform dielectric and lossy media. The 3-D bio-heat equation was then used to calculate the temperature changes in the head due to the external antenna.

B.2 MATERIALS AND METHODS

B.2.1 The Numerical Electromagnetic Model

The neural interface is implanted intracranially, including the antenna and all the neural signal processor (spike detection, signal conditioning, RF/DC converter, impedance matching, and analog to digital converter, etc). Since our focus is on the RF power reception by the implanted antenna and the associated tissue heating; the chip structure will be simplified and the antenna performance will be emphasized. An external transmitting antenna is used to transmit power to the implanted receiving antenna within the skull. In our analysis, both the transmitting (outside the head) and receiving antennas (inside the head) were designed as dipole antennas. The dipole antenna was chosen to set up a normalized model for future studies.

The transmitting antenna has a length of 63 mm and is located 10 mm away from the back of the head as shown in Figure B.1, and it resonates at a frequency of 2.38GHz in free space (achieved numerically). The receiving antenna, as a part of the neural interface, is implanted inside the skull. To calculate and analyze the efficiency of power transmission, the receiving antennas were designed with three different lengths (5 mm, 9 mm, and 15 mm) and tested at various depths (0 mm, 10 mm, 30 mm, and 60 mm) inside the brain (the brain surface is

normally 20mm from the head surface). The radiation efficiency is in part proportional to the radiation resistance (the real part of the antenna input impedance) (33,74). Ideally the radius of the wire does not affect the input resistance (33). Therefore the thickness and width of the wire of the implanted dipole antennas are negligible in this study. The material of the antenna is simulated as a perfect electrical conductor (PEC) to model very good conducting materials. The positions of the external antenna and 4 implant depths are illustrated in the sagittal plane of the human head in Figure B.1.

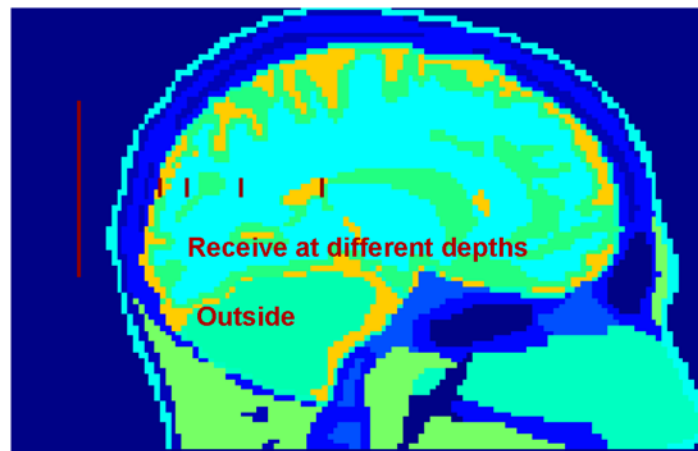


Figure B.1: Sagittal view of the human head model. (Lines represent simulated positions of the transmitting/external antenna outside of the head and the implanted neural interfaces at 4 different depths inside the skull.)

The FDTD grid of the 19-tissue head model developed from 1.5 Tesla MR images (209) has a resolution of $1\text{mm} \times 1\text{mm} \times 1\text{mm}$. The FDTD grid of the head-neural interface system has dimensions of $162 \times 278 \times 200$ cells with the spatial resolution of 1mm. The time step is 1.8873 picoseconds to satisfy the FDTD stability criterion. The perfectly matched layers (PML) (213) are used as the absorbing boundary conditions.

B.2.2 Transmission Line Excitation/Reception and Power Calculations

At the feeding location, the transmitting dipole antenna is excited by a virtual transmission line (85), which is injected with a differentiated Gaussian pulse with sufficient frequency content around the intended operational frequency. The differentiated Gaussian pulse is:

$$G(t) = \frac{1}{T \times 10^{-12}} (t - S \times T \times 10^{-9}) \exp\left(-\left(\frac{t - S \times T \times 10^{-9}}{T \times 10^{-9}}\right)^2\right) \quad (\text{B-1})$$

The parameter T affects the pulse-width and the time delay of the pulse. S is a temporal delay parameter. The widely used Medical Implant Communications Service (MICS) frequency band is 402-405 MHz (214,215). A sub-skin-depth implanted antenna has been studied around 400 MHz (216). Recent research reveals that the optimal frequency for millimeter sized implanted antennas is in the gigahertz range (77,78). A set of suitable parameters for S (5.8) and T (0.1) from equation (B-1) have been chosen for a wideband spectrum of frequencies ranging from 1GHz to 4GHz according to the lengths of the simulated antennas (5 mm, 9 mm and 15 mm). The differentiated Gaussian pulse in the time domain and the frequency response are shown in Figure B.2.

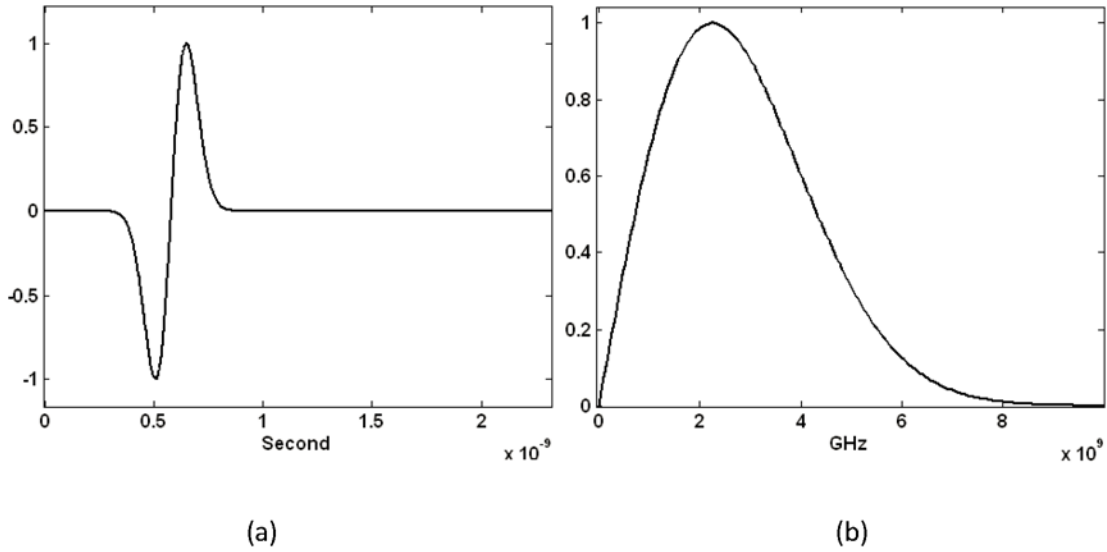


Figure B.2: The differentiated Gaussian pulse in (a) time and (b) frequency domains used to power the implanted antenna.

Using an in-house simulation FDTD software that has been experimentally validated in many MRI applications (217-219), a coaxial probe (one dimensional transmission line) feed model is implemented with the standard 3-D FDTD algorithm. This hybrid algorithm is conditionally stable and is subject to continuous adjustment according to the geometry, structure, and properties of the object being simulated.

A virtual coaxial cable is modeled as a loss-free one-dimensional transmission line (59) connected to the center-fed dipole antennas. The transmission line implementation is used to measure the power radiated by the transmit antenna outside of the head, as well as the power received by the implanted receiving antennas. The power received by each of the implanted antennas is calculated using the following equation:

$$P_{rec} = \frac{1}{2} \text{Re} [V_{rec} I_{rec}^*] \quad (\text{B-2})$$

The load impedance (which will be used to match with the transmission line impedance) Z_L as seen from the transmission line is calculated based on the following equation:

$$\frac{V(z')}{I(z')} = Z_0 \frac{Z_L + jZ_0 \tan(\beta z')}{Z_0 + jZ_L \tan(\beta z')} \quad (\text{B-3})$$

Where $V(z')/I(z')$ is the ratio of the voltage and current (using frequency domain analysis) at this location, Z_0 is the characteristic impedance of the virtual transmission line, z' is the distance between a given point located inside the transmission line and the aperture (interface between the dipole and transmission line) and $\beta = \frac{2\pi}{\lambda}$ is the wave number.

B.2.3 Impedance Matching

From circuit theory, a maximum transfer of power from a given voltage source to a load occurs when the load impedance is the complex conjugate of the source impedance (220). Before calculating the power reception by the implanted antennas, the input impedance and the resonant frequency of a load (composed of antenna, neural interface, human head, and the environment surrounding the head) are computed. After calculating the resonant frequencies and impedances of the load, the characteristic impedance of the transmission line is adjusted to match the load value. The characteristic impedance of the transmission line connected to the external (transmitting) antenna is set to 50 Ohm; while the characteristic impedance of the virtual transmission line connected to the implanted (receiving) antenna is adjusted to the antenna input impedances for the most efficient power reception.

B.2.4 The 3-D Bio-Heat Model

Since the wireless RF power produced/received by external and implanted receiving antennas is the focus of this work, temperature changes in the human tissue caused by the RF power deposition in the head with the implanted neural interface antenna due to the radiation from the external transmitting antenna will be considered. After the electromagnetic fields in the human head model are calculated using the FDTD method, the SAR distribution due to the communication between the antennas within the human head model is then computed. The temperature T changes due to the RF field from the external transmitting antenna are calculated using equation (B-4) (196).

$$\rho C_p \frac{\partial T}{\partial t} = K \nabla^2 T + A_0 - B(T - T_b) + \rho SAR \quad (\text{B-4})$$

where C_p (J/kg °C) denotes the specific heat (the amount of heat per unit mass required to raise the temperature by one degree Celsius), K (J/m s °C) denotes the thermal conductivity (the property of a material that indicates its ability to conduct heat), A_0 (J/m³ s) denotes the basal metabolic rate (the minimum calorific requirement needed to sustain life in a resting individual), and B (J/m³ s °C) denotes the blood perfusion coefficient (196,197). At the boundary between the tissue and air, the following boundary condition is applied (208):

$$K \frac{\partial T}{\partial n}(x, y, z) = -H_a (T_{x,y,z} - T_a) \quad (\text{B-5})$$

where H_a denotes the convective transfer coefficient (a constant with a value of 20 J/m² s °C) (208). The ambient temperature, T_a , is set to 24 °C (196,197).

The head model, initially at a uniform 37 °C, is put into a 24 °C environment without RF power deposition (SAR=0) until the equilibrium condition T_0 is met. A steady state is defined as

$dT/dt = 2 \times 10^{-7} \text{ }^\circ\text{C/s}$ for at least 20 minutes. Then the SAR due to the RF field is inputted in order to calculate the temperature elevations caused by the RF power emitted from the external antenna. The spatial and time steps are 1 mm and 0.0125 second, respectively. The thermal properties of the tissues in the head model can be found in Table B.1(196,208).

Table B.1: Thermal properties for the biological tissues contained in the human head model(196,208).

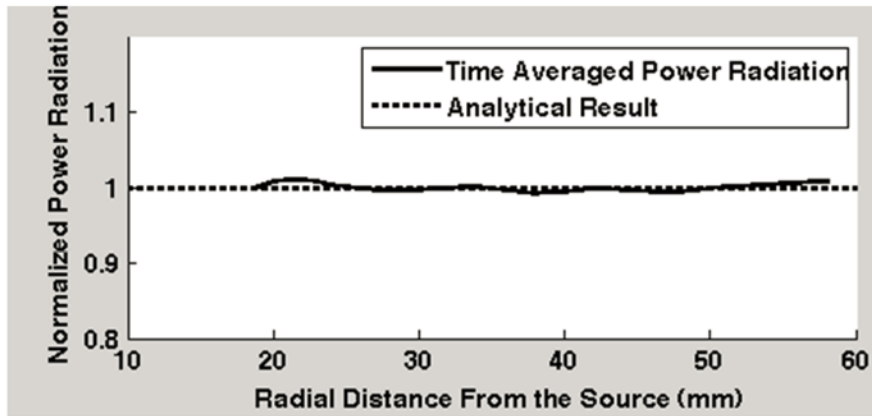
	Basal Metabolic Rate	Specific Heat	Blood Perfusion Coeff.	Thermal Conductivity
	A_o	C_p	B	K
	[J/(m ³ s)]	[J/kg °C]	[J/ (m ³ s °C)]	[J/m s °C]
Air	0	1000	0	0.03
Blood	0	3640	0	0.549
BoneCancellous	590	1300	3300	0.4
BoneCortical	610	1300	3400	0.4
BrainGreyMatter	7100	3700	40000	0.57
BrainWhiteMatter	7100	3600	15925	0.5
Cartilage	1600	3500	9000	0.47
Cerebellum	7100	3700	40000	0.57
CerebroSpinalFluid	0	4200	0	0.62
Cornea	0	4200	0	0.58
Dura	860	2802	4830	0.31
Fat	300	2500	1700	0.25
MucousMembrane	1600	3300	9000	0.43
Muscle	690	3600	2700	0.5
Nerve	7100	3500	40000	0.46
Skin Dry	1620	3500	9100	0.42
Skin Wet	1620	3500	9100	0.42
Tongue*	690	3600	2700	0.5
VitreousHumor	0	4200	0	0.6

B.3 VALIDATION

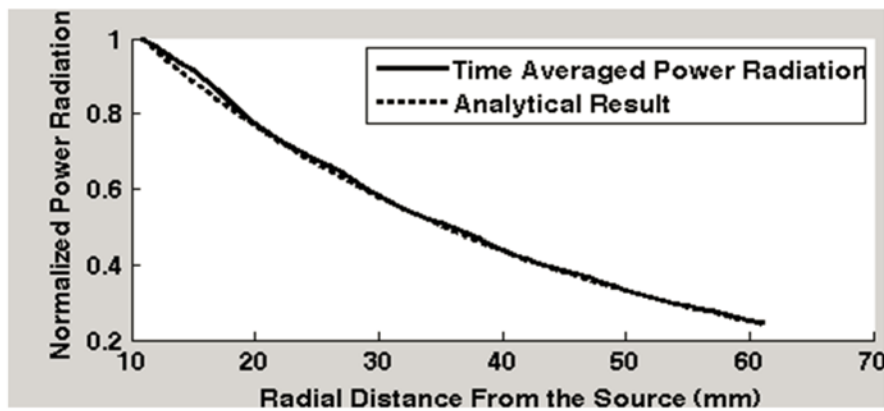
In this section we describe the analytical models of a Hertzian dipole antenna immersed in a dielectric and lossy media used to validate our numerical calculations of the implantable antenna.

Two dielectric (lossless/lossy) blocks with cubic shapes are modeled using our FDTD electromagnetic numerical model. Considering the operational frequency of 2.4 GHz, a relative dielectric constant of 39.0, and a conductivity 0.39 S/m (average dielectric constant and conductivity in the brain at 2.4 GHz) are used (88). The resolution of the domain is set to $1mm \times 1mm \times 1mm$ and the time step is 1.8873 Pico seconds (similar to that used in our calculations). A coaxial probe feed model is implemented at the center of the calculation domain as a feed point to the Hertzian dipole. Bounded with PMLs, the power radiated from the dipole in the FDTD model propagates similarly to the way it does in the lossless/lossy medium of infinite extent. After a prescribed number of time steps, the recorded electromagnetic fields in the time domain are calculated at the operational frequency of 2.4 GHz using Fourier transforms. Figure B.3 demonstrates the results of the power radiation in (a) lossless ($\sigma = 0$, $\epsilon = 39.0$) and (b) lossy ($\sigma = 0.46$, $\epsilon = 39.0$) media. In the simulation of power propagation in a lossless block (Figure B.3 (a)), the power radiated through a set of cubic-shaped surfaces enclosing the dipole is calculated as a function of the distance from the dipole. In the case of the lossy medium (Figure B.3 (b)), instead of the cubical surfaces, the power radiation is computed through a series of spherical enclosures centered on the dipole for comparison with the analytical result (shown later in equation (B-6)). The calculations in the spherical surface slightly vary with the radius of the spheres when rectangular cells in the FDTD model are applied to a polar coordinate. Therefore, the power radiation through a sphere enclosure is averaged over three adjacent

spherical layers (the resolution of the spherical layers is 1 mm which is the same as that used in the FDTD model.)



(a)



(b)

Figure B.3: Electromagnetic power radiation in (a) lossless and (b) lossy media. (The solid line represents the FDTD calculated data and dotted line represents the analytical data. The power radiation is normalized and is shown as a function of radial distance from the dipole.)

The output from the full wave FDTD model in a lossless medium Figure B.3 (a) shows that the total power radiated outwardly measured from a cubic surface is conserved: the simulation result of the time average power radiation over one period ($\lambda = \frac{2\pi}{\beta}$ where $\beta = \omega\sqrt{\mu\epsilon}$

for a lossless medium) minimally changes with propagation (less than 1% difference from the normalized value), which agrees with the energy conservation law (221).

According to the power calculation from equation (B-6) (222), radiated power of a Hertzian dipole immersed inside a lossy medium is a function of the operational frequency, the radial distance from the source, and the properties of the excitation source and the medium.

$$\begin{aligned}
 P &= \text{Re} \left\{ \int_0^{2\pi} \int_0^\pi S R^2 \sin \theta d\theta d\varphi \right\} \\
 &= \frac{\omega^3 p^2 \mu}{12\pi(\alpha^2 + \beta^2)} \left[\frac{2\alpha\beta}{R^3} + \frac{4\alpha^2\beta}{R^2} + \frac{2\alpha\beta(\alpha^2 + \beta^2)}{R} + \beta(\alpha^2 + \beta^2)^2 \right] e^{-2\alpha R}
 \end{aligned} \tag{B-6}$$

where S is the complex Poynting's vector given as $S = \frac{1}{2} E H^*$; R is the radial distance from the source; α and β are the real and imaginary parts of the propagation constant γ given in equation (B-7):

$$\gamma = \alpha + j\beta = j\omega\sqrt{\mu\varepsilon} \left(1 + \frac{\sigma}{j\omega\varepsilon} \right)^{1/2} \tag{B-7}$$

According to equation (B-7), analytical calculation is performed and the normalized power radiation is plotted as a function of radial distance from the excitation source shown with the dotted line in Figure B.3 (b). The simulation results are in excellent agreement with the analytical results. In a lossy medium, the simulation results show that electromagnetic energy decays with its propagation as shown in Figure B.3 (b). Similarly, the time average power radiation over one period ($\lambda = \frac{2\pi}{\beta}$) from the FDTD simulation clearly predicts the analytical results.

B.4 RESULTS AND DISCUSSION

B.4.1 Resonant frequencies and input impedances of the Implanted Antennas

The load as seen from the transmission line (composed of antenna, human head, and the environment surrounding the head) is numerically computed by FDTD method. Table B.2 lists the resonant frequencies (defined as the frequency at which the implanted antenna input impedance is purely real) and the corresponding input impedance for the three specified antennas at the four specified brain depths. The transmission line connected to the receiving dipole should be adjusted to these impedance values individually in order to maximize power reception. Table B.2 demonstrates that implanted dipole antennas with the same length resonate at different frequencies when implanted at various brain depths. Thus the input impedance (at resonance) of the implanted antennas (as defined equation (B-3)) varies with the antenna length as well as the position within the human brain indicating that the received near-field RF power maybe impacted by constitutive parameters of the surrounding tissues (Table B.1)

Table B.2: Resonant frequencies and input impedances for the dipole antennas implanted at various depths

Antennas(length)	0mm brain-depth		10mm brain-depth		30mm brain-depth		60mm brain-depth	
	f (GHz)	Z (Ohm)	f (GHz)	Z (Ohm)	f (GHz)	Z (Ohm)	f (GHz)	Z (Ohm)
5 mm	3.39	16.5	3.56	12.0	3.59	12.1	3.01	14.6
9 mm	2.07	22.7	2.16	16.5	2.18	14.6	1.95	16.5
15 mm	1.27	27.1	1.31	23.1	1.37	18.4	1.27	18.3

B.4.2 Maximum Power Reception without SAR Violations

The SAR safety regulations regarding RF power deposition in the head varies for different applications: the International Electrotechnical Commission (IEC) and the Food and Drug Administration (FDA) limit local SAR to ≤ 10 W/kg over every 10 grams of tissue for heating due to the RF exposure during MRI experiments (normally the frequency is less than 300MHz for human MRI studies). According to FCC safety regulations, the peak local SAR for any 1gm of tissue must be less than or equal to 1.6 W/kg when a human head is exposed to an external radiofrequency field (223). In this work, the power reception of the implanted antennas is analyzed based on the FCC SAR safety limit, which covers the frequencies up to 6 GHz.

Figure B.4 shows the maximum receiving RF power at the FCC SAR limit for the three dipole antennas at their individual resonant frequencies (shown in Table B.2) and at various brain depths. The Friis transmission formula indicates that in the far field regime and in lossless media, the power received is inversely proportional to the square of the electrical distance between the transmitting and receiving antennas. Figure B.4 demonstrates that the relationship between power reception and the implantation depth of the neural interface device does not strictly follow the Friis transmission formula due to 1) the inhomogeneous and lossy environment (human head) and 2) near field effects. Figure B.4 also shows that longer antennas receive more power than shorter ones at their individual resonant frequencies. Therefore, the results clearly show that for the shorter dipoles, the available RF power decays with a more rapid rate than the longer dipoles at greater depths inside the brain.

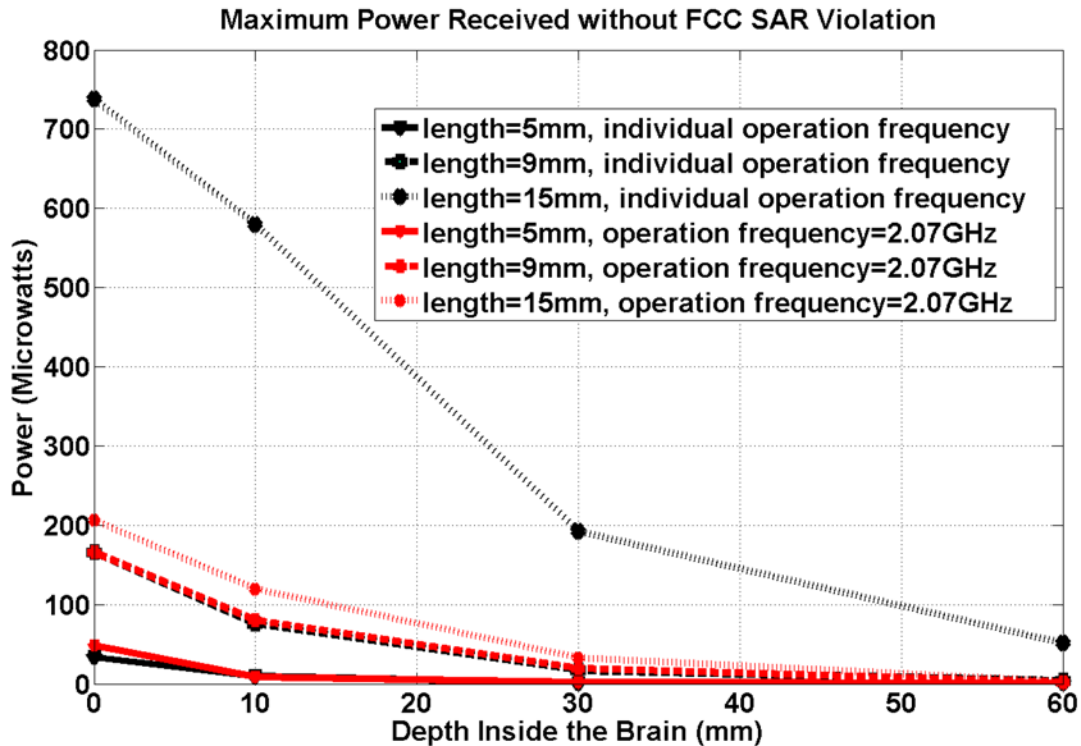


Figure B.4: Maximum power reception for all 3 antenna geometries at 2.07 GHz (red) and different frequencies tuned to their individual geometries (black) (maximum power reception at FCC SAR limit.)

Furthermore, Figure B.4 provides the maximum power reception values at the FCC SAR safety limit at 2.07 GHz (the resonant frequency of the 9-mm antenna on the surface of the brain) for the 5-mm, 9-mm and 15-mm antennas implanted at different brain depths. The results show that longer antennas at shallower brain-depths often receive more RF power at the FCC SAR limits even when operating at the non-matched/non-resonant frequencies. For example at a specified brain depth, the 15 mm dipole is still the most efficient antenna when compared to the 5-mm and 9-mm antennas even though the operational frequency (2.07 GHz) is 800 MHz away from its resonant frequency (1.27 GHz as shown in Table B.2.)

Figure B.4 along with Table B.2 demonstrate that the operating frequency significantly affects the power reception of the implanted antennas: higher frequencies result in less power

availability at the SAR limit. The loss in power at higher frequencies is a result of the reduced skin depth; thus, converting much of the RF energy into heat in the superficial tissues. However, the use of lower frequencies can possibly alter the intrinsic impedance of the antenna which can result in significant mismatch with the circuits' impedances. Therefore, a balanced choice of antenna geometry and operational frequency is crucial.

Last but not least, the development of neural interfaces capable of recording from deeper structures may require ultra-low power circuit designs. The antennas' performance at different operational frequencies in Figure B.4 shows that the maximum power available before violating the FCC SAR limit for the 15-mm implanted antenna at its resonant frequency will be 190uW or less when the neural interface is implanted at brain depths greater than 3cm (or equivalently 5cm inside the head). Assuming a 25% RF/DC conversion efficiency (due to the switching nature of the harvester circuits), the neural interfaces can consume 47.5 uW or less.

B.4.3 Temperature Changes

A maximum temperature elevation of less than 1.0 °C is regulated by the FDA government safety guideline (208,224). In this paper, we evaluated the temperature changes due to the RF radiation by the transmitting antenna.

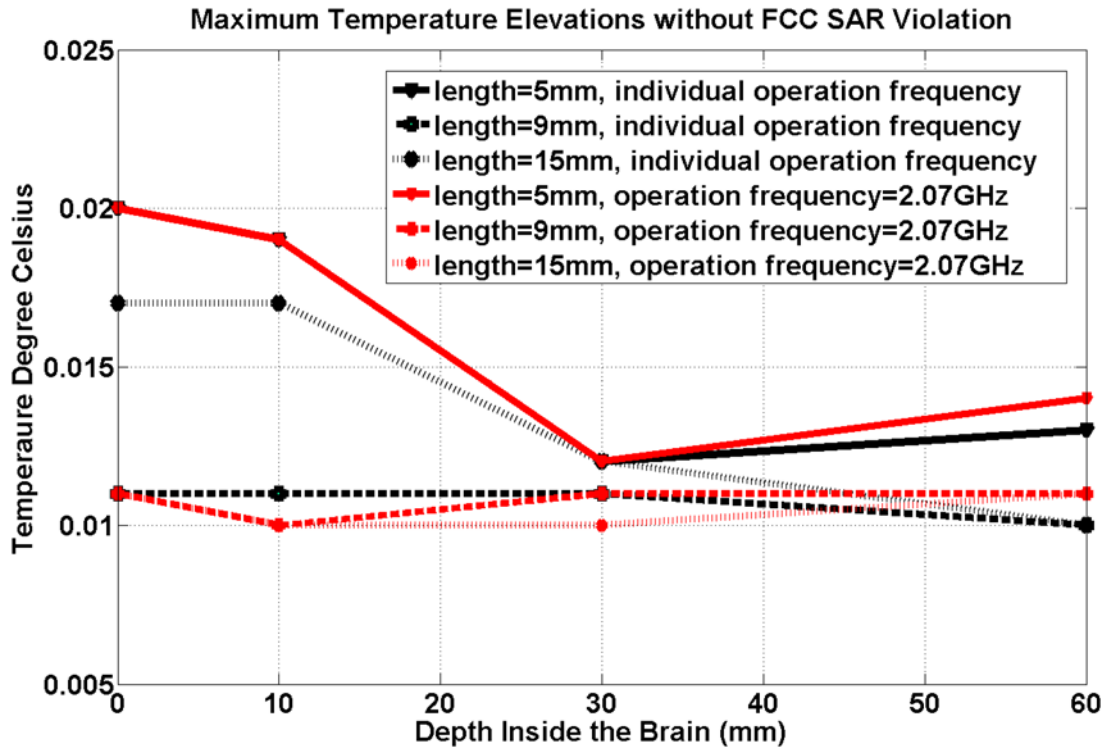


Figure B.5: Maximum temperature elevation for all 3 antenna geometries at 2.07 GHz (red) and frequencies tuned to their individual geometries (black) at FCC SAR safety limit.

Figure B.5 shows the maximum temperature elevations due to the RF radiation by the transmitting antenna when the receiving antenna is implanted at various depths. It shows that a maximum of 1.6 W/kg per 1gm SAR results in a temperature increase that is less than or equal to 0.02 °C for all cases. At the same operational frequency of 2.07GHz, the maximum temperature elevations for an antenna at various brain-depths are similar. This could be explained based on equation (B-4): the temperature changes due to the RF radiation of the external antenna mainly depend on the SAR distribution; since the maximum SAR is limited to the same value (1.6W/kg averaged over every gram of tissue), the increased temperature is expected to be very similar. Furthermore, because of the thermal diffusion was considered in this 3D simulation, small-scale

variations in SAR do not necessarily lead to biologically significant variations in temperature(225).

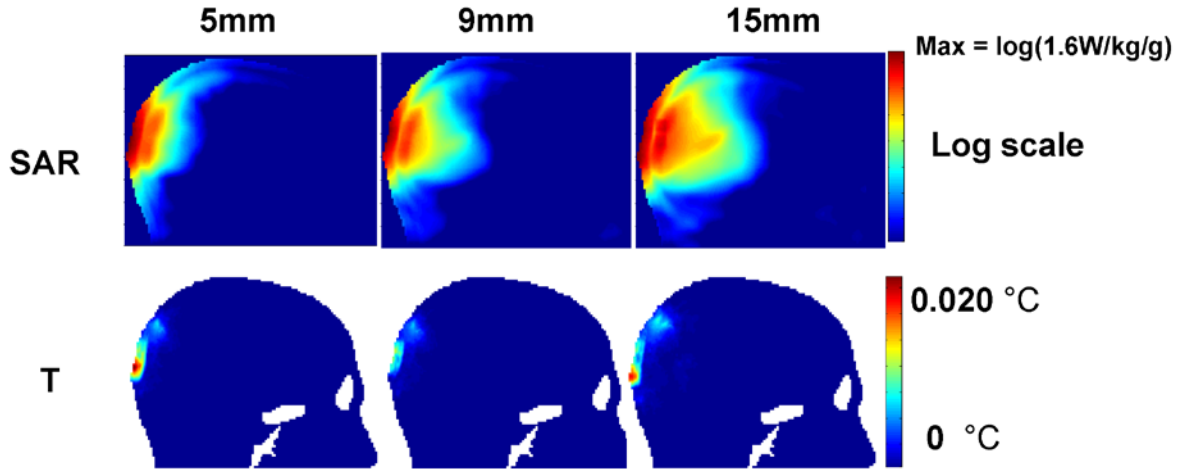


Figure B.6: Logarithmic SAR and temperature (T) distributions for the 3 antennas positioned at 0-mm brain depth.

Figure B.6 provides a set of examples of the logarithmic SAR and temperature distributions for the three antennas at 0 mm brain-depth. The top row shows the logarithmic SAR distributions for the 5-mm, 9-mm and 15-mm antennas (each operating at its resonant frequency). Comparing the results in the top row, the deposited RF power extends deeper into the brain at the lower operating frequencies (longer antenna operating frequency) than higher frequencies (shorter antenna operating frequency) with the same SAR peak (1.6 W/kg averaged over 1gm of the tissue), this is because the power is decaying faster at higher frequency than at the lower frequency). The bottom row of Figure B.6 shows the corresponding temperature elevations caused by SARs shown in the top row. The surface of the head nearest the transmitting antenna experiences the greatest temperature rise. This is expected, since the SAR and temperature peaks calculated in this section are due to the transmitting antenna rather than

the implanted receiving antenna. Comparing the temperature distributions and the SAR distributions, the temperature distributions do not always correlate with the SAR distributions; therefore predicting the locations of the hot spots (where highest temperature rise occurs) based on the SAR distribution alone can be misleading. This issue has been discussed in previous works involving high frequency electromagnetic field biological tissue interactions (226,227).

B.5 CONCLUSION

The maximum power reception (at the FCC SAR limit) by the implanted antennas was calculated for the three different dipole antenna geometries. The results demonstrate that a longer-length implanted antenna (when dipole antennas are utilized) with lower operational frequencies (not necessarily the antennas resonance frequencies) and shallower implantation depth will maximize the RF power reception prior to violating the safety limits. However, the use of lower frequencies can possibly alter the intrinsic impedance of the antenna which can result in significant mismatch with the circuits' impedances. Therefore, a balanced choice of antenna geometry and operational frequency is crucial. The corresponding temperature elevations calculated using 3-D bio-heat simulations show that for the antennas and frequencies evaluated the highest temperature increase was less than 1 °C.

The development of neural interfaces capable of recording from deeper structures may require ultra-low power circuit designs. Neural interfaces must be capable of operating with less than 47.5 uW of power when implanted at depths greater than 3 cm inside the brain (or equivalent 5 cm inside the head) based on the results in this work. Our current designs of implantable neural interface sensors consume about 35 uW (97)

For new applications that do not possess their own specific SAR regulation such as the case of measuring neural activity with wireless (RF powered) microneural interfaces (the topic of this work), new SAR limits may be determined using factors specific to the application of interest including: 1) Findings from experimental studies/numerical methods and/or 2) More complete understanding of long term consequences of exposure to electromagnetic fields.

The maximum allowable received power will then change based on new SAR limits. For instance, we have calculated the maximum power reception when IEC/FDA SAR regulations are applied and the results show that the allowed power reception will be almost ten times of the power received as when the FCC SAR limit is applied: the maximum power reception for receiving antennas operating at their resonant frequencies (shown in Table B.2) and implanted at the surface of the brain using IEC/FDA SAR safety regulations are 393.02 μW , 1996.30 μW and 7667.91 μW for 5 mm, 9 mm and 15 mm antenna respectively. The temperature elevations for these cases are 0.70 $^{\circ}\text{C}$, 0.83 $^{\circ}\text{C}$ and 0.84 $^{\circ}\text{C}$ for the 5 mm, 9 mm and 15 mm antennas respectively. This compares to power reception values of 33.25 μW , 166.03 μW , and 737.69 μW and temperature elevation values of 0.02 $^{\circ}\text{C}$, 0.011 $^{\circ}\text{C}$, and 0.017 $^{\circ}\text{C}$ when the FCC SAR limit is applied.

BIBLIOGRAPHY

1. Nicolelis MAL. Actions from thoughts. *Nature* 2001;409:403-407.
2. Mussa-Ivaldi FA, Miller LE. Brain-machine interfaces: computational demands and clinical needs meet basic neuroscience *Trends in Neurosciences* 2003;26(6):329-334.
3. Donoghue JP. Connecting cortex to machines: recent advances in brain interfaces. *Nature Neuroscience* 2002;5:1085-1088.
4. Chapin JK, Moxon KA, Markowitz RS, Nicolelis MAL. Real-time control of a robot arm using simultaneously recorded neurons in the motor cortex. *Nature Neuroscience* 1999;2:664-670.
5. Hochberg LR, Bacher D, Jarosiewicz B, Masse NY, Simeral JD, Vogel J, Haddadin S, Liu J, Cash SS, van der Smagt P, Donoghue JP. Reach and grasp by people with tetraplegia using a neurally controlled robotic arm. *Nature* 2012;485(7398):372-U121.
6. Collinger JL, Wodlinger B, Downey JE, Wang W, Tyler-Kabara EC, Weber DJ, McMorland J, Velliste M, Boninger ML, Schwartz AB. High-performance neuroprosthetic control by an individual with tetraplegia. *Lancet* 2012.
7. Hochberg LR, Serruya MD, Friehs GM, Mukand JA, Saleh M, Caplan AH, Branner A, Chen D, Penn RD, Donoghue JP. Neuronal ensemble control of prosthetic devices by a human with tetraplegia. *Nature* 2006;442:164-171.
8. Borton DA, Yin M, Aceros J, Nurmikko A. An implantable wireless neural interface for recording cortical circuit dynamics in moving primates. *J Neural Eng* 2013;10(2):026010.
9. Tropp J. Image brightening in samples of high dielectric constant. *J Magn Reson* 2004;167(1):12-24.
10. Ibrahim TS, Mitchell C, Abraham R, Schmalbrock P. In-depth study of the electromagnetics of ultrahigh-field MRI. *Nmr Biomed* 2007;20(1):58-68.
11. Vaughan JT, Garwood M, Collins CM, Liu W, DelaBarre L, Adriany G, Andersen P, Merkle H, Goebel R, Smith MB, Ugurbil K. 7T vs. 4T: RF power, homogeneity, and signal-to-noise comparison in head images. *Magn Reson Med* 2001;46(1):24-30.

12. Ibrahim TS, Tang L. Insight into RF power requirements and B1 field homogeneity for human MRI via rigorous FDTD approach. *J Magn Reson Imaging* 2007;25(6):1235-1247.
13. Roschmann P. Radiofrequency penetration and absorption in the human body: limitations to high-field whole-body nuclear magnetic resonance imaging. *Med Phys* 1987;14(6):922-931.
14. Vaughan JT, Snyder CJ, DelaBarre LJ, Bolan PJ, Tian J, Bolinger L, Adriany G, Andersen P, Strupp J, Ugurbil K. Whole-body imaging at 7T: preliminary results. *Magn Reson Med* 2009;61(1):244-248.
15. Eichfelder G, Gebhardt M. Local specific absorption rate control for parallel transmission by virtual observation points. *Magn Reson Med* 2011;66(5):1468-1476.
16. Kerchner GA. Ultra-High Field 7T MRI: A New Tool for Studying Alzheimer's Disease. *J Alzheimers Dis* 2011;26:91-95.
17. Crozier S, Forbes LK, Roffmann WU, Luescher K, Doddrell DM. Currents and fields in shielded RF resonators for NMR/MRI. *Meas Sci Technol* 1996;7(7):1083-1086.
18. Adriany G, Van de Moortele PF, Wiesinger F, Moeller S, Strupp JP, Andersen P, Snyder C, Zhang X, Chen W, Pruessmann KP, Boesiger P, Vaughan T, Ugurbil K. Transmit and receive transmission line arrays for 7 Tesla parallel imaging. *Magnet Reson Med* 2005;53(2):434-445.
19. Novikov A. Advanced theory of driven birdcage resonator with losses for biomedical magnetic resonance imaging and spectroscopy. *Magn Reson Imaging* 2011;29(2):260-271.
20. Tropp J. Image brightening in samples of high dielectric constant. *J Magn Reson* 2004;167(1):12-24.
21. Wright SM. Full-wave analysis of planar radiofrequency coils and coil arrays with assumed current distribution. *Concept Magnetic Res* 2002;15(1):2-14.
22. Grissom W, Yip CY, Zhang Z, Stenger VA, Fessler JA, Noll DC. Spatial domain method for the design of RF pulses in multicoil parallel excitation. *Magn Reson Med* 2006;56(3):620-629.
23. Zheng H, Zhao TJ, Qian YX, Ibrahim T, Boada F. Parallel transmission RF pulse design for eddy current correction at ultra high field. *J Magn Reson* 2012;221:139-146.
24. Pfabigan DM, Seidel EM, Sladky R, Hahn A, Paul K, Grahl A, Kublbock M, Kraus C, Hummer A, Kranz GS, Windischberger C, Lanzenberger R, Lamm C. P300 amplitude variation is related to ventral striatum BOLD response during gain and loss anticipation: An EEG and fMRI experiment. *Neuroimage* 2014;96:12-21.

25. Rak RJ, Kolodziej M, Majkowski A. Brain-Computer Interface as Measurement and Control System the Review Paper. *Metrol Meas Syst* 2012;19(3):427-444.
26. DiLorenzo DJ, Jankovic J, Simpson RK, Takei H, Powell SZ. Neurohistopathological Findings at the Electrode-Tissue Interface in Long-Term Deep Brain Stimulation: Systematic Literature Review, Case Report, and Assessment of Stimulation Threshold Safety. *Neuromodulation : journal of the International Neuromodulation Society* 2014;17(5):405-418.
27. Lobel DA, Lee KH. Brain Machine Interface and Limb Reanimation Technologies: Restoring Function After Spinal Cord Injury Through Development of a Bypass System. *Mayo Clin Proc* 2014;89(5):708-714.
28. Clark GM. The multiple-channel cochlear implant: the interface between sound and the central nervous system for hearing, speech, and language in deaf people - a personal perspective. *Philos T R Soc B* 2006;361(1469):791-810.
29. Swann NC, De Hemptinne C, Ostrem JL, San Luciano M, Starr PA. Chronic cortical and subcortical recordings in Parkinson's disease using a totally implanted bidirectional neural interface. *Movement Disord* 2014;29:S288-S288.
30. Ahn M, Lee M, Choi J, Jun SC. A Review of Brain-Computer Interface Games and an Opinion Survey from Researchers, Developers and Users. *Sensors-Basel* 2014;14(8):14601-14633.
31. Lebedev MA, Nicolelis MAL. Brain-machine interfaces: past, present and future. *Trends Neurosci* 2006;29(9):536-546.
32. Nicolas-Alonso LF, Gomez-Gil J. Brain Computer Interfaces, a Review. *Sensors-Basel* 2012;12(2):1211-1279.
33. Balanis CA. *Antenna theory : analysis and design*. Hoboken, NJ: John Wiley; 2005. xvii, 1117 p. p.
34. Skrivervik AK, Zurcher JF, Staub O, Mosig JR. PCS antenna design: The challenge of miniaturization. *Ieee Antennas Propag* 2001;43(4):12-26.
35. Chae MS, Yang Z, Yuce MR, Hoang L, Liu WT. A 128-Channel 6 mW Wireless Neural Recording IC With Spike Feature Extraction and UWB Transmitter. *Ieee T Neur Sys Reh* 2009;17(4):312-321.
36. Kim J, Rahmat-Samii Y. Implanted antennas inside a human body: Simulations, designs, and characterizations. *Ieee T Microw Theory* 2004;52(8):1934-1943.
37. Gosselin B, Sawan M. An Ultra Low-Power CMOS Automatic Action Potential Detector. *Ieee T Neur Sys Reh* 2009;17(4):346-353.

38. Ibrahim TS, Abraham D, Rennaker RL. Electromagnetic power absorption and temperature changes due to brain machine interface operation. *Ann Biomed Eng* 2007;35(5):825-834.
39. Hayes CE, Edelstein WA, Schenck JF, Mueller OM, Eash M. An Efficient, Highly Homogeneous Radiofrequency Coil for Whole-Body Nmr Imaging at 1.5-T. *J Magn Reson* 1985;63(3):622-628.
40. Vaughan JT, Adriany G, Garwood M, Yacoub E, Duong T, DelaBarre L, Andersen P, Ugurbil K. Detunable transverse electromagnetic (TEM) volume coil for high-field NMR. *Magn Reson Med* 2002;47(5):990-1000.
41. Wen H, Jaffer FA, Denison TJ, Duewell S, Chesnick AS, Balaban RS. The evaluation of dielectric resonators containing H₂O or D₂O as RF coils for high-field MR imaging and spectroscopy. *J Magn Reson Ser B* 1996;110(2):117-123.
42. Brunner DO, De Zanche N, Frohlich J, Paska J, Pruessmann KP. Travelling-wave nuclear magnetic resonance. *Nature* 2009;457(7232):994-U992.
43. Zhao Y, Zhao T, Raval SB, Krishnamurthy N, Zheng H, Harris CT, Handler WB, Chronik BA, Ibrahim TS. Dual Optimization Method of Radiofrequency and Quasistatic Field Simulations for Reduction of Eddy Currents Generated on 7T Radiofrequency Coil Shielding. *Magnetic Resonance in Medicine* 2014.
44. Zhao Y, Zhao T, Krishnamurthy N, Ibrahim TS. On the E-field construction/deconstruction and B₁₊ Efficiency/Homogeneity with Transmit Array Eigen Modes. 2014; Milan, Italy. *ISMRM*. p 4931.
45. Roemer PB, Edelstein WA, Hayes CE, Souza SP, Mueller OM. The Nmr Phased-Array. *Magnet Reson Med* 1990;16(2):192-225.
46. Hong SM, Park JH, Woo MK, Kim YB, Cho ZH. New design concept of monopole antenna array for UHF 7T MRI. *Magn Reson Med* 2013.
47. Ibrahim TS. Analytical approach to the MR signal. *Magn Reson Med* 2005;54(3):677-682.
48. Zhao Y, Rennaker RL, Hutchens C, Ibrahim TS. Implanted miniaturized antenna for brain computer interface applications: analysis and design. *PloS one* 2014;9(7):e103945.
49. Zhao Y, Tang L, Rennaker R, Hutchens C, Ibrahim TS. Studies in RF Power Communication, SAR, and Temperature Elevation in Wireless Implantable Neural Interfaces. *PloS one* 2013;8(11):e77759.
50. Tang L, Hue YK, Ibrahim TS. Studies of RF Shimming Techniques with Minimization of RF Power Deposition and Their Associated Temperature Changes. *Concept Magn Reson B* 2011;39B(1):11-25.
51. Ibrahim TS, Tang L, Kangarlu A, Abraham R. Electromagnetic and modeling analyses of an implanted device at 3 and 7 Tesla. *J Magn Reson Imaging* 2007;26(5):1362-1367.

52. Hausman S, Januszkiewicz L. Impact of Indoor Environment on Path Loss in Body Area Networks. *Sensors-Basel* 2014;14(10):19551-19560.
53. Tanaka S, Shimizu K, Sakuma S, Tsuchiya T, Endoh N. Experimental and Numerical Analysis of Temperature Rise in Phantom Caused by High-Intensity Focused Ultrasonic Irradiation. *Jpn J Appl Phys* 2013;52(7).
54. Nelson DA, Curran AR, Nyberg HA, Marttila EA, Mason PA, Ziriak JM. High-resolution simulations of the thermophysiological effects of human exposure to 100 MHz RF energy. *Phys Med Biol* 2013;58(6):1947-1968.
55. Yacoob SM, Hassan NS. FDTD analysis of a noninvasive hyperthermia system for brain tumors. *Biomedical engineering online* 2012;11.
56. Fioocchi S, Markakis IA, Ravazzani P, Samaras T. SAR exposure from UHF RFID reader in adult, child, pregnant woman, and fetus anatomical models. *Bioelectromagnetics* 2013;34(6):443-452.
57. Yee KS. Numerical Solution of Initial Boundary Value Problems Involving Maxwells Equations in Isotropic Media. *Ieee T Antenn Propag* 1966;Ap14(3):302-&.
58. Taflove A, Hagness SC. *Computational electrodynamics : the finite-difference time-domain method*. Boston: Artech House; 2005. xxii, 1006 p., [1008] f. de pl. en coul. p.
59. Makinen R, Kangas V, Lahtinen J, Kivikoski M. A coaxial probe feed model for FDTD. *Microw Opt Techn Let* 2002;34(3):193-198.
60. Hertel TW, Smith GS. On the convergence of common FDTD feed models for antennas. *Ieee T Antenn Propag* 2003;51(8):1771-1779.
61. Maloney JG, Shlager KL, Smith GS. A Simple Fdtd Model for Transient Excitation of Antennas by Transmission-Lines. *Ieee T Antenn Propag* 1994;42(2):289-292.
62. Physik RWÜeNMzLgVdM. *J Reine Angew Math* 1909;Vol. 135:1-61.
63. Courant R. *Bulletin of the American Mathematical Society* 1943; 49 1-23.
64. Clough RW. The finite element method in plane stress analysis. *American Society of Civil Engineers 2nd Conference on Electronic Computation*. Pittsburgh, PA1960.
65. Chestek CA, Gilja V, Nuyujukian P, Kier RJ, Solzbacher F, Ryu SI, Harrison RR, Shenoy KV. HermesC: low-power wireless neural recording system for freely moving primates. *IEEE Trans Neural Syst Rehabil Eng* 2009;17(4):330-338.
66. Farshchi S, Pesterev A, Nuyujukian P, Guenterberg E, Mody I, Judy JW. Embedded Neural Recording With TinyOS-Based Wireless-Enabled Processor Modules. *Ieee T Neur Sys Reh* 2010;18(2):134-141.

67. Song YK, Borton DA, Park S, Patterson WR, Bull CW, Laiwalla F, Mislou J, Simeral JD, Donoghue JP, Nurmikko AV. Active Microelectronic Neurosensor Arrays for Implantable Brain Communication Interfaces. *Ieee T Neur Sys Reh* 2009;17(4):339-345.
68. Harrison RR, Kier RJ, Chestek CA, Gilja V, Nuyujukian P, Ryu S, Greger B, Solzbacher F, Shenoy KV. Wireless Neural Recording With Single Low-Power Integrated Circuit. *Ieee T Neur Sys Reh* 2009;17(4):322-329.
69. Irazoqui PP, Mody I, Judy JW. Recording brain activity wirelessly. *Ieee Eng Med Biol* 2005;24(6):48-54.
70. Kim S, Zoschke K, Klein M, Black D, Buschick K, Toepper M, Tathireddy P, Harrison R, Oppermann H, Solzbacher F. Switchable polymer-based thin film coils as a power module for wireless neural interfaces. *Sensor Actuat a-Phys* 2007;136(1):467-474.
71. Kiourti A, Nikita KS. Numerical assessment of the performance of a scalp-implantable antenna: effects of head anatomy and dielectric parameters. *Bioelectromagnetics* 2013;34(3):167-179.
72. Soontornpipit P, Furse CM, Chung YC. Design of implantable microstrip antenna for communication with medical implants. *Ieee T Microw Theory* 2004;52(8):1944-1951.
73. Merli F, Fuchs B, Mosig JR, Skrivervik AK. The Effect of Insulating Layers on the Performance of Implanted Antennas. *Ieee T Antenn Propag* 2011;59(1):21-31.
74. Hall PS, Hao Y. *Antennas and propagation for body-centric wireless communications*. Boston: Artech House; 2006. 1 online resource (xiii, 291 s.) p.
75. Warty R, Tofighi MR, Kawoos U, Rosen A. Characterization of Implantable Antennas for Intracranial Pressure Monitoring: Reflection by and Transmission Through a Scalp Phantom. *Ieee T Microw Theory* 2008;56(10):2366-2376.
76. Gosalia K, Lazzi G, Humayun M. Investigation of a microwave data telemetry link for a retinal prosthesis. *Ieee T Microw Theory* 2004;52(8):1925-1933.
77. Poon ASY, O'Driscoll S, Meng TH. Optimal Frequency for Wireless Power Transmission Into Dispersive Tissue. *Ieee T Antenn Propag* 2010;58(5):1739-1750.
78. Yakovlev A, Kim S, Poon A. Implantable Biomedical Devices: Wireless Powering and Communication. *Ieee Commun Mag* 2012;50(4):152-159.
79. King RWP, Smith GS. *Antennas in Matter: Fundamentals, Theory, and Applications*. Cambridge, MA: The MIT Press; 1981.
80. Fenwick RC, Weeks WI. Summerged antenna characteristics. *Ieee T Antenn Propag* 1963;11(3):296-305.

81. Ibrahim TS, Hue YK, Tang L. Understanding and manipulating the RF fields at high field MRI. *Nmr Biomed* 2009;22(9):927-936.
82. Krishnamurthy N, Zhao T, Ibrahim TS. Effects of receive-only inserts on specific absorption rate, B field, and Tx coil performance. *J Magn Reson Imaging* 2013.
83. Tang L, Hue YK, Ibrahim TS. Studies of RF Shimming Techniques with Minimization of RF Power Deposition and Their Associated Temperature Changes. *Concepts Magn Reson Part B Magn Reson Eng* 2011;39B(1):11-25.
84. Maloney JG, Smith GS. The Efficient Modeling of Thin Material Sheets in the Finite-Difference Time-Domain (FDTD) Method. *Ieee T Antenn Propag* 1992;40(3):323-330.
85. Maloney JG, Shlager KL, Smith GS. A Simple FDTD Model for Transient Excitation of Antennas by Transmission Lines. *IEEE TRANSACTIONS ON ANTENNAS AND PROPAGATION* 1994;42(2):289-292.
86. Endo T, Sunahara Y, Satoh S, Katagi T. Resonant frequency and radiation efficiency of meander line antennas. *Electron Comm Jpn* 2000;83(1):52-58.
87. Ibrahim TS, Lee R, Baertlein BA, Abduljalil AM, Zhu H, Robitaille PML. Effect of RF coil excitation on field inhomogeneity at ultra high fields: A field optimized TEM resonator. *Magn Reson Imaging* 2001;19(10):1339-1347.
88. Andreuccetti D, Fossi R, Petrucci C. An Internet resource for the calculation of the dielectric properties of body tissues in the frequency range 10 Hz - 100 GHz. Website at <http://niremf.ifac.cnr.it/tissprop/>, IFAC-CNR, Florence (Italy). 1997. p Based on data published by C.Gabriel et al. in 1996.
89. Hertel TW, Smith GS. The insulated linear antenna - Revisited. *Ieee T Antenn Propag* 2000;48(6):914-920.
90. Alberti G, Casciola M, Massinelli L, Bauer B. Polymeric proton conducting membranes for medium temperature fuel cells (110–160°C). *Journal of Membrane Science* 2001;185(1):73-81.
91. Kobayashi T, Rikukawa M, Sanui K, Ogata N. Proton-conducting polymers derived from poly(ether-etherketone) and poly(4-phenoxybenzoyl-1,4-phenylene). *Solid State Ionics* 1998;106(3–4):219-225.
92. Chen ZN, Liu GC, See TSP. Transmission of RF Signals Between MICS Loop Antennas in Free Space and Implanted in the Human Head. *Ieee T Antenn Propag* 2009;57(6):1850-1854.
93. Zhao HP, Shen ZX. Weighted Laguerre Polynomials-Finite Difference Method for Time-Domain Modeling of Thin Wire Antennas in a Loaded Cavity. *Ieee Antenn Wirel Pr* 2009;8:1131-1134.

94. Nakano H, Tagami H, Yoshizawa A, Yamauchi J. Shortening Ratios of Modified Dipole Antennas. *Ieee T Antenn Propag* 1984;32(4):385-386.
95. IEEE. IEEE Standard for Safety Levels with Respect to Human Exposure to Radio Frequency Electromagnetic Fields, 3 kHz to 300 GHz. IEEE Standard for Safety Levels with Respect to Human Exposure to Radio Frequency Electromagnetic Fields, 3 kHz to 300 GHz 2005.
96. ICNIRP. Guidelines for limiting exposure to time-varying electric, magnetic, and electromagnetic fields (up to 300 GHz). International Commission on Non-Ionizing Radiation Protection. *Health physics*. Volume 74 1998. p 494-522.
97. Hutchens C, Rennaker RL, 2nd, Venkataraman S, Ahmed R, Liao R, Ibrahim T. Implantable radio frequency identification sensors: wireless power and communication. *Conf Proc IEEE Eng Med Biol Soc* 2011;2011:2886-2892.
98. Nehrke K, Bornert P. Eigenmode analysis of transmit coil array for tailored B1 mapping. *Magn Reson Med* 2010;63(3):754-764.
99. Lattanzi R, Sodickson DK. Ideal current patterns yielding optimal signal-to-noise ratio and specific absorption rate in magnetic resonance imaging: computational methods and physical insights. *Magn Reson Med* 2012;68(1):286-304.
100. Ibrahim TS, Zhao Y, Krishnamurthy N, Raval SB, Zhao T, Wood S, Kim J. 20-To-8 Channel Tx Array with 32-Channel Adjustable Receive-Only Insert for 7T Head Imaging. 2013; Salt Lake City, Utah. International Society of Magnetic Resonance in Medicine p4408.
101. Aussenhofer SA, Webb AG. An eight-channel transmit/receive array of TE₀₁ mode high permittivity ceramic resonators for human imaging at 7 T. *J Magn Reson* 2014;243:122-129.
102. Taracila V, Petropoulos LS, Eagan TP, Brown RW. Image uniformity improvement for birdcage-like volume coils at 400 MHz using multichannel excitations. *Concept Magn Reson B* 2006;29B(3):153-160.
103. King SB, Varosi SM, Duensing GR. Eigenmode analysis for understanding phased array coils and their limits. *Concept Magn Reson B* 2006;29B(1):42-49.
104. King SB, Varosi SM, Duensing GR. Optimum SNR Data Compression in Hardware Using an Eigencoil Array. *Magnet Reson Med* 2010;63(5):1346-1356.
105. Wang C, Qu P, Shen GX. Potential advantage of higher-order modes of birdcage coil for parallel imaging. *J Magn Reson* 2006;182(1):160-167.
106. Ibrahim TS, Hue Y-K, Boada FE, Gilbert R. Tic Tac Toe: Highly-Coupled, Load Insensitive Tx/Rx Array and a Quadrature Coil Without Lumped Capacitors 2008; International Society of Magnetic Resonance in Medicine . Toronto, Canada. p 438.

107. Zhao Y, Wood S, Zhao T, Krishnamurthy N, Ibrahim TS. Simultaneous Excitation of Distinct Electromagnetic Modes Using a Tx Array. 2013; Salt Lake City, US. ISMRM. p 4399.
108. Zhao Y, Zhao T, Raval SB, Krishnamurthy N, Zheng H, Harris CT, Handler WB, Chronik BA, Ibrahim TS. Dual Optimization Method of RF and Quasi-Static Field Simulations for Reduction of Eddy Currents Generated on 7T RF Coil Shielding. *Magnetic Resonance in Medicine* (in press).
109. Bluman GW, Cole JD. The general similarity solution of the heat equation. *Journal of Mathematics and Mechanics* 1969;18(11).
110. Vester M, Nistler J, Oppelt R, Renz W. Using a mode concept to reduce hardware needs for multichannel transmit array. 2006; international Society of Magnetic Resonance in Medicine. p 2024.
111. Cheng DK. *Field and wave electromagnetics*. Reading, Mass.: Addison-Wesley Pub. Co.; 1989. xvi, 703 p. p.
112. Cheng DK. *Field and wave electromagnetics*. Reading, Mass.: Addison-Wesley Pub. Co.; 1989.
113. Pauly J, Nishimura D, Macovski A. A k-space analysis of small-tip-angle excitation. 1989. *J Magn Reson* 2011;213(2):544-557.
114. Setsompop K, Alagappan V, Gagoski B, Witzel T, Polimeni J, Potthast A, Hebrank F, Fontius U, Schmitt F, Wald LL, Adalsteinsson E. Slice-selective RF pulses for in vivo B1+ inhomogeneity mitigation at 7 tesla using parallel RF excitation with a 16-element coil. *Magn Reson Med* 2008;60(6):1422-1432.
115. Katscher U, Bornert P, Leussler C, van den Brink JS. Transmit SENSE. *Magn Reson Med* 2003;49(1):144-150.
116. Gilbert KM, Curtis AT, Gati JS, Klassen LM, Menon RS. A radiofrequency coil to facilitate B-1(+) shimming and parallel imaging acceleration in three dimensions at 7 T. *Nmr Biomed* 2011;24(7):815-823.
117. Shajan G, Kozlov M, Hoffmann J, Turner R, Scheffler K, Pohmann R. A 16-channel dual-row transmit array in combination with a 31-element receive array for human brain imaging at 9.4 T. *Magn Reson Med* 2013.
118. Avdievich NI. Transceiver-Phased Arrays for Human Brain Studies at 7 T. *Appl Magn Reson* 2011;41(2-4):483-506.
119. Trakic A, Li BK, Weber E, Wang H, Wilson S, Crozier S. A Rapidly Rotating RF Coil for MRI. *Concept Magn Reson B* 2009;35B(2):59-66.

120. Trakic A, Weber E, Li BK, Wang H, Liu F, Engstrom C, Crozier S. Electromechanical Design and Construction of a Rotating Radio-Frequency Coil System for Applications in Magnetic Resonance. *Ieee T Bio-Med Eng* 2012;59(4):1068-1075.
121. Alsop DC, Connick TJ, Mizsei G. Spiral volume coil for improved RF field homogeneity at high static magnetic field strength. *Magnet Reson Med* 1998;40(1):49-54.
122. Ibrahim TS, Hue YK, Tang L. Understanding and manipulating the RF fields at high field MRI. *Nmr Biomed* 2009;22(9):927-936.
123. Hue Y-K, Ibrahim TS, Zhao T, Boada FE, Qian Y. A Complete Modeling System with Experimental Validation for Calculating the Transmit and Receive Fields, Total Power Deposition, Input Impedance, and Coupling between Coil Elements ISMRM2008. p 1193.
124. Christ A, Kainz W, Hahn EG, Honegger K, Zefferer M, Neufeld E, Rascher W, Janka R, Bautz W, Chen J, Kiefer B, Schmitt P, Hollenbach HP, Shen J, Oberle M, Szczerba D, Kam A, Guag JW, Kuster N. The Virtual Family--development of surface-based anatomical models of two adults and two children for dosimetric simulations. *Phys Med Biol* 2010;55(2):N23-38.
125. Alagappan V, Nistler J, Adalsteinsson E, Setsompop K, Fontius U, Zelinski A, Vester M, Wiggins GC, Hebrank F, Renz W, Schmitt F, Wald LL. Degenerate mode band-pass birdcage coil for accelerated parallel excitation. *Magn Reson Med* 2007;57(6):1148-1158.
126. Orzada S, Maderwald S, Poser BA, Bitz AK, Quick HH, Ladd ME. RF Excitation Using Time Interleaved Acquisition of Modes (TIAMO) to Address B(1) Inhomogeneity in High-Field MRI. *Magnet Reson Med* 2010;64(2):327-333.
127. G. C. Wiggins OK, E. Zakszewski, V. Alagappan, C. J. Wiggins and L. L. Wald. A 7 Tesla Gradient Mode Birdcage Coil for Improved Temporal and Occipital Lobe SNR. ISMRM. Seattle, Washington, USA2006.
128. Yazdanbakhsh P, Fester M, Oppelt R, Bitz A, Kraff O, Orzada S, Ladd ME, Solbach K. Variable Power Combiner for a 7T Butler Matrix Coil Array. 2009. p 791.
129. Alagappan V, Setsompop K, Nistler J, Potthast A, Schmitt F, Adalsteinsson E, Wald LL. A Simplified 16-channel Butler Matrix for Parallel Excitation with the Birdcage Modes at 7T. 2008. p 144.
130. Hetherington HP, Avdievich NI, Kuznetsov AM, Pan JW. RF shimming for spectroscopic localization in the human brain at 7 T. *Magn Reson Med* 2010;63(1):9-19.
131. van den Bergen B, van den Berg CAT, Bartels LW, Lagendijk JJW. 7 T body MRI: B-1 shimming with simultaneous SAR reduction. *Phys Med Biol* 2007;52(17):5429-5441.

132. Van den Berg CAT, Van den Bergen B, de Kamer JBV, Raaymakers BW, Kroeze H, Bartels LW, Lagendijk JJW. Simultaneous B-1(+) homogenization and specific absorption rate hotspot suppression using a magnetic resonance phased array transmit coil. *Magnet Reson Med* 2007;57(3):577-586.
133. Collins CM, Liu W, Swift BJ, Smith MB. Combination of optimized transmit arrays and some receive array reconstruction methods can yield homogeneous images at very high frequencies. *Magn Reson Med* 2005;54(6):1327-1332.
134. Hue Y, Zhao T, Qian Y, Boada F, Ibrahim T. A Complete Modeling System with Experimental Validation for Calculating the Transmit and Receive Fields, Total Power Deposition, Input Impedance, and Coupling between Coil Elements. 2008 April; Toronto. p 1193.
135. Bitz AK, Gumbrecht R, Orzada S, Fautz H-P, Ladd ME. Evaluation of Virtual Observation Points for Local SAR Monitoring of Multi-Channel Transmit RF Coils at 7 Tesla. 2013.
136. Brink W, Webb A. Apparent B1+Asymmetry in Symmetric Objects at High Fields Milan, Italy: ISMRM; 2014. p 4815.
137. Truhn D, Kiessling F, Schulz V. Optimized RF shielding techniques for simultaneous PET/MR. *Med Phys* 2011;38(7):3995-4000.
138. Jehenson P, Westphal M, Schuff N. Analytical Method for the Compensation of Eddy-Current Effects Induced by Pulsed Magnetic-Field Gradients in Nmr Systems. *J Magn Reson* 1990;90(2):264-278.
139. Trakic A, Wang H, Liu F, Lopez HS, Crozier S. Analysis of transient eddy currents in MRI using a cylindrical FDTD method. *Ieee T Appl Supercon* 2006;16(3):1924-1936.
140. Tang F, Lopez HS, Freschi F, Smith E, Li Y, Fuentes M, Liu F, Repetto M, Crozier S. Skin and proximity effects in the conductors of split gradient coils for a hybrid Linac-MRI scanner. *J Magn Reson* 2014;242C:86-94.
141. Sanchez Lopez H, Freschi F, Trakic A, Smith E, Herbert J, Fuentes M, Wilson S, Liu L, Repetto M, Crozier S. Multilayer integral method for simulation of eddy currents in thin volumes of arbitrary geometry produced by MRI gradient coils. *Magn Reson Med* 2014;71(5):1912-1922.
142. Harris CT, Haw DW, Handler WB, Chronik BA. Application and experimental validation of an integral method for simulation of gradient-induced eddy currents on conducting surfaces during magnetic resonance imaging. *Phys Med Biol* 2013;58(12):4367-4379.
143. Sanchez Lopez H, Poole M, Crozier S. Eddy current simulation in thick cylinders of finite length induced by coils of arbitrary geometry. *J Magn Reson* 2010;207(2):251-261.
144. Kroot JMB, van Eijndhoven SJL, van de Ven AAF. Eddy currents in a transverse MRI gradient coil. *J Eng Math* 2008;62(4):315-331.

145. Boesch C, Gruetter R, Martin E. Temporal and spatial analysis of fields generated by eddy currents in superconducting magnets: optimization of corrections and quantitative characterization of magnet/gradient systems. *Magn Reson Med* 1991;20(2):268-284.
146. Chapman B, Mansfield P. Double Active Magnetic Screening of Coils in Nmr. *J Phys D Appl Phys* 1986;19(7):L129-L131.
147. Wysong RE, Madio DP, Lowe IJ. A Novel Eddy-Current Compensation Scheme for Pulsed Gradient Systems. *Magnet Reson Med* 1994;31(5):572-575.
148. Ganin A, King KF; General Electric Company (Waukesha, WI), assignee. Automatic measurement of gradient field distortion. United States 2001.
149. Duyn JH, Yang YH, Frank JA, van der Veen JW. Simple correction method for k-space trajectory deviations in MRI. *J Magn Reson* 1998;132(1):150-153.
150. Mohammadi S, Moller HE, Kugel H, Muller DK, Deppe M. Correcting eddy current and motion effects by affine whole-brain registrations: evaluation of three-dimensional distortions and comparison with slicewise correction. *Magn Reson Med* 2010;64(4):1047-1056.
151. Xu D, Maier JK, King KF, Collick BD, Wu G, Peters RD, Hinks RS. Prospective and retrospective high order eddy current mitigation for diffusion weighted echo planar imaging. *Magn Reson Med* 2013;70(5):1293-1305.
152. Vaughan JT. An Improved Volume Coil for High Field MRI *ISMRM* 1999:167.
153. Alecci M, Jezzard P. Characterization and reduction of gradient-induced eddy currents in the RF shield of a TEM resonator. *Magnet Reson Med* 2002;48(2):404-407.
154. Daniel J. Weyers QL; Shielding apparatus for magnetic resonance imaging. US 2006.
155. Yao Z, Wu Y, Chmielewski T, Shvartsman S, Eagan T, Martens M, Brown R. Simulation guidelines for incisions patterns on RF shields. *Concept Magn Reson B* 2012;41B(2):37-49.
156. Jaskolski PLW, WI), Eash, Matthew G. (Oconomowoc, WI); General Electric Company (Milwaukee, WI), assignee. Mutual inductance NMR RF coil matching device. United States 1987.
157. Jin J-M. Electromagnetic analysis and design in magnetic resonance imaging. Boca Raton, Fla. etc.: CRC press; 1999. 174 p.
158. Roemer PB, Edelstein WA; RF shield for RF coil contained within gradient coils of NMR imaging device United States 1989.

159. T. S. Ibrahim YZ, T. Zhao, N. Krishnamurthy, S. Wood, S. Raval and H. Kim. 20-to-8 Channel Tx Array with 32-channel Adjustable Receive-Only Insert for 7T Head Imaging. 2013; Salt Lake City, Utah. ISMRM. p 4408.
160. Lattanzi R, Sodickson DK. Ideal current patterns yielding optimal signal-to-noise ratio and specific absorption rate in magnetic resonance imaging: Computational methods and physical insights. *Magnet Reson Med* 2012;68(1):286-304.
161. Freire MJ, Lopez MA, Meise F, Algarin JM, Jakob PM, Bock M, Marques R. A broadside-split-ring resonator-based coil for MRI at 7 T. *IEEE Trans Med Imaging* 2013;32(6):1081-1084.
162. Raghuraman S, Mueller MF, Zbyn S, Baer P, Breuer FA, Friedrich KM, Trattnig S, Lanz T, Jakob PM. 12-channel receive array with a volume transmit coil for hand/wrist imaging at 7 T. *J Magn Reson Imaging* 2013;38(1):238-244.
163. Brown R, Madelin G, Lattanzi R, Chang G, Regatte RR, Sodickson DK, Wiggins GC. Design of a nested eight-channel sodium and four-channel proton coil for 7T knee imaging. *Magn Reson Med* 2013;70(1):259-268.
164. Pang Y, Xie Z, Xu D, Kelley DA, Nelson SJ, Vigneron DB, Zhang X. A dual-tuned quadrature volume coil with mixed $\lambda/2$ and $\lambda/4$ microstrip resonators for multinuclear MRSI at 7 T. *Magn Reson Imaging* 2012;30(2):290-298.
165. Raaijmakers AJ, Ipek O, Klomp DW, Possanzini C, Harvey PR, Lagendijk JJ, van den Berg CA. Design of a radiative surface coil array element at 7 T: the single-side adapted dipole antenna. *Magn Reson Med* 2011;66(5):1488-1497.
166. Metzger GJ, van de Moortele PF, Akgun C, Snyder CJ, Moeller S, Strupp J, Andersen P, Shrivastava D, Vaughan T, Ugurbil K, Adriany G. Performance of external and internal coil configurations for prostate investigations at 7 T. *Magn Reson Med* 2010;64(6):1625-1639.
167. Gilbert KM, Curtis AT, Gati JS, Klassen LM, Villemaire LE, Menon RS. Transmit/receive radiofrequency coil with individually shielded elements. *Magn Reson Med* 2010;64(6):1640-1651.
168. Brown R, Storey P, Geppert C, McGorty K, Leite AP, Babb J, Sodickson DK, Wiggins GC, Moy L. Breast MRI at 7 Tesla with a bilateral coil and T1-weighted acquisition with robust fat suppression: image evaluation and comparison with 3 Tesla. *European radiology* 2013;23(11):2969-2978.
169. Thalhammer C, Renz W, Winter L, Hezel F, Rieger J, Pfeiffer H, Graessl A, Seifert F, Hoffmann W, von Knobelsdorff-Brenkenhoff F, Tkachenko V, Schulz-Menger J, Kellman P, Niendorf T. Two-Dimensional Sixteen Channel Transmit/Receive Coil Array for Cardiac MRI at 7.0 T: Design, Evaluation, and Application. *J Magn Reson Imaging* 2012;36(4):847-857.

170. Wiggins GC, Mareyam A, Setsompop K, Alagappan V, Potthast A, Wald LL. A Close-Fitting 7 Tesla 8 Channel Transmit/Receive Helmet Array with Dodecahedral Symmetry and B1 Variation Along Z. 2008; Toronto Canada. p 148.
171. Aussenhofer SA, Webb AG. Design and evaluation of a detunable water-based quadrature HEM11 mode dielectric resonator as a new type of volume coil for high field MRI. *Magn Reson Med* 2012;68(4):1325-1331.
172. Zhao Y, Stough D, Zheng H, Zhao T, Harris CT, Handler WB, Chronik BA, Boada FE, Ibrahim TS. Maximizing RF efficiency and minimizing eddy current artifacts using RF and eddy current simulations. *International Society of Magnetic Resonance in Medicine*. Melbourne, Australia 2012. p 536.
173. Wiggins GC, Potthast A, Triantafyllou C, Wiggins CJ, Wald LL. Eight-channel phased array coil and detunable TEM volume coil for 7 T brain imaging. *Magn Reson Med* 2005;54(1):235-240.
174. Peeren GN. Stream function approach for determining optimal surface currents. *J Comput Phys* 2003;191(1):305-321.
175. Atkinson IC, Lu A, Thulborn KR. Characterization and correction of system delays and eddy currents for MR imaging with ultrashort echo-time and time-varying gradients. *Magn Reson Med* 2009;62(2):532-537.
176. Ibrahim TS, Hue YK, Tang L. Understanding and manipulating the RF fields at high field MRI. *NMR Biomed* 2009;22(9):927-936.
177. H. Zheng TZ, Y. Qian, T. Ibrahim, and F. Boada. Characterization and correction of eddy currents for ultra high field parallel transmission with RF pulse design. *ISMRM*. Montreal, Canada 2011.
178. Olivo J, Carrara S, De Micheli G. Energy Harvesting and Remote Powering for Implantable Biosensors. *Ieee Sens J* 2011;11(7):1573-1586.
179. Alagappan V, Nistler J, Adalsteinsson E, Setsompop K, Fontius U, Zelinski A, Vester M, Wiggins GC, Hebrank F, Renz W, Schmitt F, Wald LL. Degenerate mode band-pass birdcage coil for accelerated parallel excitation. *Magnet Reson Med* 2007;57(6):1148-1158.
180. Mao WH, Smith MB, Collins CM. Exploring the limits of RF shimming for high-field MRI of the human head. *Magnet Reson Med* 2006;56(4):918-922.
181. Alsop DC, Connick TJ, Mizsei G. A spiral volume coil for improved RF field homogeneity at high static magnetic field strength. *Magn Reson Med* 1998;40(1):49-54.
182. T. S. Ibrahim Y-KH, F. E. Boada, and R. Gilbert. Tic Tac Toe: Highly-Coupled, Load Insensitive Tx/Rx Array and a Quadrature Coil Without Lumped Capacitors. *ISMRM*. Toronto 2008.

183. Jin J-M. Electromagnetic analysis and design in magnetic resonance imaging. Boca Raton: CRC Press; 1998. xiv, 282 p. p.
184. P. Yazdanbakhsh AB, S. Orzada, O. Kraff, M. E. Ladd, and K. Solbach. Planar Butler Matrix Technology for 7 Tesla MRI. ISMRM. Honolulu, Hawaii 2009.
185. Vaughan JT, Adriany G, Garwood M, Yacoub E, Duong T, DelaBarre L, Andersen P, Ugurbil K. Detunable transverse electromagnetic (TEM) volume coil for high-field NMR. *Magnet Reson Med* 2002;47(5):990-1000.
186. Wiggins GC, Potthast A, Triantafyllou C, Wiggins CJ, Wald LL. Eight-channel phased array coil and detunable TEM volume coil for 7 T brain imaging. *Magnet Reson Med* 2005;54(1):235-240.
187. Gan L, Johnson JA. Oxidative damage and the Nrf2-ARE pathway in neurodegenerative diseases. *Biochim Biophys Acta* 2014;1842(8):1208-1218.
188. Hu SH, Liu TY, Huang HY, Liu DM, Chen SY. Magnetic-sensitive silica nanospheres for controlled drug release. *Langmuir : the ACS journal of surfaces and colloids* 2008;24(1):239-244.
189. Bell CJ, Shenoy P, Chalodhorn R, Rao RPN. Control of a humanoid robot by a noninvasive brain-computer interface in humans. *J Neural Eng* 2008;5(2):214-220.
190. Sitaram R, Caria A, Veit R, Gaber T, Rota G, Kuebler A, Birbaumer N. FMRI Brain-Computer Interface: A Tool for Neuroscientific Research and Treatment. *Computational Intelligence and Neuroscience* 2007;2007.
191. Wessberg J, Stambaugh CR, Kralik JD, Beck PD, Laubach M, Chapin JK, Kim J, Biggs SJ, Srinivasan MA, Nicolelis MAL. Real-time prediction of hand trajectory by ensembles of cortical neurons in primates. *Nature* 2000;408:361-365.
192. Chase SM, Kass RE, Schwartz AB. Behavioral and neural correlates of visuomotor adaptation observed through a brain-computer interface in primary motor cortex. *J Neurophysiol* 2012;108(2):624-644.
193. Gilja V, Nuyujukian P, Chestek CA, Cunningham JP, Yu BM, Fan JM, Churchland MM, Kaufman MT, Kao JC, Ryu SI, Shenoy KV. A high-performance neural prosthesis enabled by control algorithm design. *Nat Neurosci* 2012;15(12):1752-1757.
194. Chen JY, Gandhi OP. Numerical simulation of annular-phased arrays of dipoles for hyperthermia of deep-seated tumors. *IEEE Trans Biomed Eng* 1992;39(3):209-216.
195. Kang G, Gandhi OP. SARs for pocket-mounted mobile telephones at 835 and 1900 MHz. *Phys Med Biol* 2002;47:4301-4313.
196. DeMarco SC, Lazzi G, Liu WT, Weiland JD, Humayun MS. Computed SAR and thermal elevation in a 0.25-mm 2-D model of the human eye and head in response to an

- implanted retinal stimulator - Part I: Models and methods. *Ieee Transactions on Antennas and Propagation* 2003;51(9):2274-2285.
197. Lazzi G, DeMarco SC, Liu WT, Weiland JD, Humayun MS. Computed SAR and thermal elevation in a 0.25-mm 2-D model of the human eye and head in response to an implanted retinal stimulator - Part II: Results. *Ieee T Antenn Propag* 2003;51(9):2286-2295.
 198. Bernardi P, Cavagnaro M, Lin JC, Pisa S, PiuZZi E. Distribution of SAR and temperature elevation induced in a phantom by a microwave cardiac ablation catheter. *Microwave Theory and Techniques, IEEE Transactions on* 2004;52(8):1978-1986.
 199. Rappaport C. Cardiac tissue ablation with catheter-based microwave heating. *Int J Hyperthermia* 2004;20(7):769-780.
 200. Gu ZJ, Rappaport CM, Wang PJ, VanderBrink BA. A 2 1/4-turn spiral antenna for catheter cardiac ablation. *Ieee Transactions on Biomedical Engineering* 1999;46(12):1480-1482.
 201. Shock SA, Meredith K, Warner TF, Sampson LA, Wright AS, Winter TC, Mahvi DM, Fine JP, Lee FT. Microwave ablation with loop antenna: in vivo porcine liver model. *Radiology* 2004;231(1):143-149.
 202. Gosalia K, Lazzi G, Humayun M. Investigation of a microwave data telemetry link for a retinal prosthesis. *Microwave Theory and Techniques, IEEE Transactions on* 2004:1925-1933.
 203. Lazzi G. Thermal effects of bioimplants. *IEEE Eng Med Biol Mag* 2005;24(5):75-81.
 204. Mojarradi M, Binkley D, Blalock B, Andersen R, Ulshoefer N, Johnson T, Del Castillo L. A miniaturized neuroprosthesis suitable for implantation into the brain. *IEEE TRANSACTIONS ON NEURAL SYSTEMS AND REHABILITATION ENGINEERING* 2003;11(1):38-42.
 205. Bashirullah R, Harris JG, Sanchez JC, Nishida T, Principe JC. Florida Wireless Implantable Recording Electrodes (FWIRE) for Brain Machine Interfaces. *IEEE International Symposium on Circuits and Systems, 2007 ISCAS 2007* 2007:2084-2087.
 206. Kim S, Tathireddy P, Normann RA, Solzbacher F. Thermal impact of an active 3-D microelectrode array implanted in the brain. *IEEE Trans Neural Syst Rehabil Eng* 2007;15(4):493-501.
 207. Schwerdt HN, Miranda FA, Chae J. Analysis of Electromagnetic Fields Induced in Operation of a Wireless Fully Passive Backscattering Neurorecording Microsystem in Emulated Human Head Tissue. *Ieee T Microw Theory* 2013;61(5):2170-2176.
 208. Ibrahim TS, Abraham D, Rennaker RL. Electromagnetic power absorption and temperature changes due to brain machine interface operation. *Ann Biomed Eng* 2007;35(5):825-834.

209. Ibrahim TS, Abduljalil AM, Baertlein BA, Lee R, Robitaille PM. Analysis of B1 field profiles and SAR values for multi-strut transverse electromagnetic RF coils in high field MRI applications. *Phys Med Biol* 2001;46(10):2545-2555.
210. RF coils for MRI. ; JTV, Griffiths JR, editors: John Wiley & Sons; 2011.
211. Ibrahim TS, Lee R, Baertlein BA, Abduljalil AM, Zhu H, Robitaille PM. Effect of RF coil excitation on field inhomogeneity at ultra high fields: a field optimized TEM resonator. *Magn Reson Imaging* 2001;19(10):1339-1347.
212. Ibrahim TS, Lee R, Abduljalil AM, Baertlein BA, Robitaille PM. Dielectric resonances and B(1) field inhomogeneity in UHFMRI: computational analysis and experimental findings. *Magn Reson Imaging* 2001;19(2):219-226.
213. Berenger JP. A Perfectly Matched Layer for the Absorption of Electromagnetic-Waves. *Journal of Computational Physics* 1994;114(2):185-200.
214. Chow EY, Morris MM, Irazoqui PP. Implantable RF Medical Devices. *Ieee Microw Mag* 2013;14(4):64-73.
215. Kiourti A, Nikita KS. A Review of Implantable Patch Antennas for Biomedical Telemetry: Challenges and Solutions. *Ieee Antennas Propag* 2012;54(3):210-228.
216. Bjorninen T, Muller R, Ledochowitsch P, Sydanheimo L, Ukkonen L, Maharbiz MM, Rabaey JM. Design of Wireless Links to Implanted Brain-Machine Interface Microelectronic Systems. *Ieee Antenn Wirel Pr* 2012;11:1663-1666.
217. Ibrahim TS, Tang L, Kangarlu A, Abraham R. Electromagnetic and modeling analyses of an implanted device at 3 and 7 Tesla. *J Magn Reson Imaging* 2007;26(5):1362-1367.
218. Ibrahim TS, Hue YK, Tang L. Understanding and manipulating the RF fields at high field MRI. *NMR Biomed* 2009;22(9):927-936.
219. Ibrahim TS, Kangarlu A, Chakeress DW. Design and performance issues of RF coils utilized in ultra high field MRI: experimental and numerical evaluations. *IEEE Trans Biomed Eng* 2005;52(7):1278-1284.
220. Cheng DK. *Field and Wave Electromagnetics*: Pearson Education Inc.; 2001.
221. Balanis CA. *Advanced Engineering Electromagnetics*: Wiley; Solution Manual edition (May 9, 1989); 1989.
222. Tai CT, Collin RE. Radiation of a Hertzian dipole immersed in a dissipative medium. *IEEE Transactions on Antennas and Propagation* 2000;48(10):1501-1506.
223. FCC. FCC Policy on Human Exposure to Radiofrequency Electromagnetic Fields. In: *Comission FC*, editor 1996.

224. Nominations from FDA's Center for Device and Radiological Health. <http://www.ntp.niehs.nih.gov/index.cfm?objectid=03DB98A9-E505-AA26-833749D41A8F0B671999>.
225. Petersen R, Bodemann R. Comment on "A new IEEE standard for safety levels with respect to human exposure to radio-frequency radiation". *Ieee Antennas Propag* 2006;48(4):129-130.
226. Oh S, Webb AG, Neuberger T, Park B, Collins CM. Experimental and Numerical Assessment of MRI-Induced Temperature Change and SAR Distributions in Phantoms and In Vivo. *Magnet Reson Med* 2010;63(1):218-223.
227. Wang ZW, Lin JC, Mao WH, Liu WZ, Smith MB, Collins CM. SAR and temperature: Simulations and comparison to regulatory limits for MRI. *J Magn Reson Imaging* 2007;26(2):437-441.
228. Fujimoto K, Polimeni JR, van der Kouwe AJ, Reuter M, Kober T, Benner T, Fischl B, Wald LL. Quantitative comparison of cortical surface reconstructions from MP2RAGE and multi-echo MPRAGE data at 3 and 7 T. *Neuroimage* 2014;90:60-73.
229. Schreiner SJ, Liu X, Gietl AF, Wyss M, Steininger SC, Gruber E, Treyer V, Meier IB, Kalin AM, Leh SE, Buck A, Nitsch RM, Pruessmann KP, Hock C, Unschuld PG. Regional Fluid-Attenuated Inversion Recovery (FLAIR) at 7 Tesla correlates with amyloid beta in hippocampus and brainstem of cognitively normal elderly subjects. *Frontiers in aging neuroscience* 2014;6:240.
230. Wu X, Schmitter S, Auerbach EJ, Moeller S, Ugurbil K, Van de Moortele PF. Simultaneous multislice multiband parallel radiofrequency excitation with independent slice-specific transmit B1 homogenization. *Magn Reson Med* 2013.